SOME ASPECTS OF CORNER VORTICES IN SEPARATED FLOWS: A THEORETICAL AND NUMERICAL INVESTIGATION

by

Sougata Biswas
(Roll Number: 126123012)

Department of Mathematics
Indian Institute of Technology Guwahati, India
August, 2018

SOME ASPECTS OF CORNER VORTICES IN SEPARATED FLOWS: A THEORETICAL AND NUMERICAL INVESTIGATION

A Thesis Submitted

for the Award of the Degree of

Doctor of Philosophy

by

Sougata Biswas
(Roll Number: 126123012)

to the

DEPARTMENT OF MATHEMATICS

INDIAN INSTITUTE OF TECHNOLOGY GUWAHATI

August, 2018

TH-1927_126123012


भारतीय प्रौद्योगिकी संस्थान गुवाहाटी
Indian Institute of Technology Guwahati

DECLARATION

It is certified that the work contained in this thesis entitled **“Some Aspects of Corner Vortices in Separated Flows: A Theoretical and Numerical Investigation”** has done by me, under the supervision of **Dr. Jiten C. Kalita**, Professor, Department of Mathematics, Indian Institute of Technology Guwahati for the award of the degree of Doctor of Philosophy and this work has not been submitted elsewhere for a degree.

August, 2018

Sougata Biswas
Roll No. 126123012
Department of Mathematics
Indian Institute of Technology Guwahati

CERTIFICATE

It is certified that the work contained in this thesis entitled **"Some Aspects of Corner Vortices in Separated Flows: A Theoretical and Numerical Investigation"** by **Sougata Biswas,** a student of Department of Mathematics, Indian Institute of Technology Guwahati, for the award of the degree of Doctor of Philosophy has been carried out under my supervision and this work has not been submitted elsewhere for a degree.

August, 2018

Dr. Jiten Chandra Kalita
Professor
Department of Mathematics
Indian Institute of Technology Guwahati

भारतीय प्रौद्योगिकी संस्थान गुवाहाटी • Indian Institute of Technology Guwahati •

To My Parents

***Mangali Biswas and Shyamal Biswas*, for**
their infinite love, sacrifice and devotion
and to my *Supervisor* for his inspiration,
motivation and discipline.

Indian Institute of Technology Guwahati

TH-1927_126123012

भारतीय प्रौद्योगिकी संस्थान गुवाहाटी • Indian Institute of Technology Guwahati •

Acknowledgements

Though this thesis has my name on its cover page, it would not have been possible without contributions of several individuals who in different ways gave the inspiration, motivation and energy to carry out this study. I would like to take this opportunity to thank them all.

I am grateful to God for giving me all the good health, wisdom and patience to make this thesis possible.

First and foremost, I would like to express my deep and sincere gratitude to my thesis supervisor, **Prof. Jiten C. Kalita** for guiding me through my research; his careful guidance, constructive criticisms and valuable suggestions proved very stimulating and helpful. I am deeply indebted to him for his utmost care and making me feel free to express my views. Without his help and frequent advice, the work could not have been accomplished. I would never forget about his constant inspiration and love throughout my research days. It would be really unfair enough not to state that he is truly a good friend, philosopher and a great guide for someone like me. I consider myself lucky and most honoured to be his research student. I will be forever indebted to him for his encouragement in every aspect of my life. Thank you very much Sir!

I owe a huge debt of gratitude to Mrs. Deepshikha Choudhury who showered me with her motherly love and affection. In reality, it is very difficult to acknowledge her with only a few words.

With great appreciation, I would like to thank Prof. Kalpesh Kapoor, chairman of my doctoral committee and other members of the committee, Dr. Siddhartha Pratim Chakrabarty (Department of Mathematics) and Prof. Anoop Kumar Dass (Department of Mechanical Engineering) for their valuable suggestions, helpful criticism and in overseeing the advancement of my work. I would like to thank Prof. Rajen Kumar Sinha, Dr. P. A. S. Sree Krishna, Dr. K. V. Srikanth (Department of Mathematics) and Dr. Arnab Kumar De (Department of Mechanical Engineering) for learning the basics during my course work which proved very handy in my research. I am also extremely thankful to Dr. Pankaj Kumar Mishra (Department of Physics) for his crucial suggestions in my research work.

My gratitude towards Prof. Karl Gustafson (University of Colorado Boulder), Prof. Aynur Ünal (Standford University) and Dr. Manoranjan Mishra (IIT Ropar) for their constant encouragement, support and valuable suggestions in my research work.

I must convey my sincere gratitude to Prof. Swaroop Nandan Bora who always look after me like his child. His utmost care, affection and love really means a lot to me. Special thanks to Dr. Jitendriya Swain for his constant support during my M.Sc and encouraging me for pursuing Ph.D. In the same vein, I express my gratitude to Dr. Anjan Kumar Chakrabarty, one of the dedicated and fantastic faculties of IIT Guwahati. I enjoyed his lectures during my course work and enrich some of his teaching skills.

I take this opportunity to express my gratitude to all the faculty members of the Department of Mathematics who have offered help directly or indirectly at different stages during my research work. My sincere thanks are due to Mr. Santanu Majumdar, Mr. Pranpratim Borgohain and Mr. Pranab Jyoti Boro for their technical support, Mr. Sridhar Samal, Mr. Phatik Kumar and Mr. Saurav Choudhury of the Department of Mathematics for their assistance in all official matters.

I gladly acknowledge the Indian Institute of Technology Guwahati for providing me various facilities to carry out my research work. I am grateful to the Ministry of Human Resource Development, Government of India for providing me financial assistance during the period of my Ph.D programme.

I am fortunate to have Ravi Da, Manideepa Di, Santu Da, Sunanda Di, Dinesh Da, Barun Da, Punit Da, Sibu Da, Debopam Da, Swarup Da, Himadri Da, Gayatri Di, Saloni Di as my seniors. I am thankful to them for all their help during my stay at IIT Guwahati. I take this opportunity to convey my gratefulness to my friends and co-researchers. I would like to thank Anirudha, Anirban, Hiru Da, Abhishek Da, Naba Da, Jayanta Da, Swarup, N. Balasubramani, Madhu, Debu, Tanushree, Koyel, Rakesh (Department of Mathematics) and Simon Peter, Subrat, Pabitra, Subhra, Soni, Shatrughan (Department of Mechanical Engineering) for all their timely help, encouragement and support.

Special thanks to Swapnendu, Ankur, Devanand, Ankita and Rahul Deka for their wonderful company for making my life at IIT Guwahati an extremely comfortable one. I have always had a great time with them. Apart from fun,

TH-1927_126123012

they have also been great sources of learning and have gifted me memories that I will cherish for ever. My heartfelt thanks to my senior Dr. Bidyut Bikash Gogoi, Scientist, Space Navigation Group, ISRO Satellite Centre (ISAC), Bangalore for his friendship, brotherly love, care, valuable suggestions and help throughout this work.

My revered regards goes to Dr. Animesh Kumar Golder, Department of Chemical Engineering for his utmost care and love during my stay at IIT Guwahati.

I express my deep sense of appreciation for Dr. Atashi Karpha, Principal and Dr. Jayjayanti Ray of Gokhale Memorial Girls' College, Kolkata. I will never be able to repay their help during my last phase of Ph.D days.

This work would have not been possible without the strong moral support and the unfailing faith of my parents, my mother Mrs. Mangali Biswas (Maa) and my father Mr. Shyamal Biswas (Baba), which have sustained me throughout this endeavour. I would like to thank my younger sister Shila (Bunu), and my cousins Newtan (Dada), Soma (Didi), Souraj, Bijoy, Mampi, Shilpi, Palas, Sudipta and Sukhen for their pampering love and care. They have been a source of inspiration throughout my life and I dedicate this thesis to them. I am also thankful to my grandmother Mrs. Hemlata Biswas (Thakuma) and my uncle Mr. Swapan Kumar Biswas (Chotka) for always playing a supportive role in my life.

Special thanks to my school teachers Mrs. Asalata Biswas, Mr. Kanchan Mandal and my college teachers Dr. Krishnendu Dutta, Dr. Sanjib Kumar Chakrabarti, who have been always inspired and encouraged me for pursuing higher studies and taught me the lesson to become a good human being.

Lastly, I would like to convey my deepest love to my school friend Sukdeb Chandra Mallik for his encouragement and support during my Ph.D teniure. Thanks to him for being always with me in every step of this journey and beyond.

August, 2018 **Sougata Biswas**

Abstract

This dissertation is mainly concerned with the theoretical and numerical investigation of corner vortices in two- and three-dimensional (2D and 3D) incompressible internal viscous separated flows; it is an endeavour to delve into certain unexplored facets of vortex dynamics. The work is broadly divided into two parts. In the first part, we establish Moffatt-likeness of the corner vortices in the lid-driven square cavity for Stokes flow and flow for moderate Reynolds numbers in the pre-asymptotic regime. The corner vortices have been resolved and documented with extreme details up to the post-quaternary level, both qualitatively and quantitatively. In the process, we also observe the self-similarity of these vortices from fractal point of view. Next, we utilize the critical point theory from the recent advances in topological fluid dynamics to gain more physical insights into the corner vortices from the perspective of the flow topology in the 2D vis a vis 3D cavity. The Poincaré-Bendixson formula is used to validate the computed results for the possible number of critical points in the cavity. We further present a detailed discussion of the vortical structures in 3D rectangular cavities including the dynamics of Taylor-Görtler-Like vortices by a rigorous topological theory. We also report the presence of "U-shaped and mushroom-shaped vortex" structures in the flow field through the visualization of λ_2 isosurfaces.

The second part of the work consists of the development of some novel theories on Moffatt vortices in incompressible viscous flows in bounded domains. We propose two topological equivalence classes of Moffatt vortices: one in terms of orientation preserving homeomorphism; and the other by half-saddle point structures. We further quantify the centers of vortices as fixed points through Brouwer fixed-point theorem and define boundary of a vortex as circle cell. The salient feature of this dissertation is however the development of a series of proofs establishing the finiteness of Moffatt vortices which was thought to be infinite from the time of its inception. Besides, we have listed the concerns and pertinent questions on the notion of infiniteness of such sequences and pinpointed where the assumptions of the existing hypothesis might have gone wrong. Making use of some elementary concepts of mathematical analysis and our own construction of diametric disks, we proved that the number of vortices in solid corners in a bounded domain must be finite. We further extend the above mentioned work on the finiteness of vortices to the more general situation in steady incompressible viscous flows on bounded domains.


भारतीय प्रौद्योगिकी संस्थान गुवाहाटी
Indian Institute of Technology Guwahati

Contents

Indian Institute of Technology Guwahati

List of Figures

TH-1927_126123012

Indian Institute of Technology Guwahati

List of Tables

Chapter 1

INTRODUCTION

1.1 General background

In the last few decades, the physical problem of the formation and evolution of vortices in fluids has generated a tremendous interest among applied mathematicians, fluid dynamicists and physicists alike. Vortices are considered to be the most important structure in a flow as it essentially controls the dynamics of the flow [10]. Although a precise definition of a vortex is difficult to obtain, according to physicists and fluid dynamicists, a vortex describes a circulating region of a flow, and for most of us the term indicates the occurrence of certain rotation in some way. Physical phenomena like flow down a bath plug hole, tornados, smoke rings, the flow behind the tips of an aircraft wing in flight describe a vortex. Though vortices, whenever formed, occupy a very small portion of the flow domain, they play a key role in the organization of the flow as "*the sinews and muscles of the fluid motion*" [89] and "*the sinews of turbulence*" [110]. In incompressible viscous flows, vortices are known to form and occur in corners and in the vicinity of separation points.

The existence of an infinite sequence of vortices (known as Moffatt vortices) [106, 107] at the corner of solid structure for internal flows with decreasing size and rapidly decreasing intensity has been indicated by physical experiments [140] and mathematical asymptotics [106, 107, 108]. Fluid dynamics and its mathematical description in terms of the Navier–Stokes (N–S) equations are fundamental in theoretical and applied sciences including physics, aerodynamics and other basic sciences. In particular, the physical problem of the formation and evolution of vortices in fluids, the N–S equations provide a framework for exploring different facets of the flow. The geometric theories of incompressible viscous flows are also founded on a divergence-free vector field which is very much a part of the N–S equations for incompressible viscous flows.

Topological fluid dynamics is a very young mathematical discipline that studies geometric features of flows with complicated trajectories and their applications to fluid motions. There are various approaches to study topological aspects of fluid flow problems such as critical point theory, differential topology, Lie group, differential geometry, knot theory etc.

The current work is an endeavour of exploring some new aspects of vortical structures in two-dimensional (2D) and three-dimensional (3D) separated flows by making use of the concepts mentioned above. Most of our observations are based on the numerical solution of the N–S equations either in its two or three-dimensional form and application of the recent developments of topological fluid dynamics.

In the following, we list the motivation, objectives and a brief summary of the present work.

1.2 Motivation

Existing literature reveals that the numerical investigation of Moffatt vortices at the corner has been confined to the mere mention of finding multiple vortices mainly for Reynolds number, $Re \to 0$ only in flows such as the backward-facing step and the triangular cavity [15, 30, 40, 70]. To the best of our knowledge, no detailed study on their quantification in internal flows for higher Reynolds numbers is available in the literature. Again, all the previous studies on the lid-driven cavity flow are confined to either the study of its 2D or 3D configuration in isolation. No study of the cavity flow in the context of 2D vis a vis 3D has been carried out so far. Moreover, describing vortical structures in such flows in the light of topological fluid dynamics seems to be restricted and there are many aspects which still remain unexplored. One such aspect is the exploration of the typical sequence of dynamical structures via topological evolution during the formation of a new vortex.

A careful look at the literature on the 3D lid-driven cavity reveals that the topological description of the flow was mainly confined to listing the critical points without much clarity in their classification. Although most of the studies were unanimous in the existence of Taylor-Görtler-Like (TGL) vortices at moderate Reynolds numbers, the investigation into their topological aspects seemed far from complete. As mentioned earlier, the term "infinite sequence of corner vortices" is synonymous with the existence of Moffatt vortices. However, the notion of infiniteness of Moffatt vortices is claimed without any rigorous mathematical proof and this issue still remained unaccomplished and unanswered. The present study endeavours to address all the issues mentioned above.

1.3 Objectives

The present work envisages to study some aspects of corner vortices in 2D and 3D separated flows through numerical and theoretical approaches. The main objectives of the current work are as follows:

(i) To quantify the corner vortices as Moffatt both for Stokes flow and moderately higher Reynolds numbers in the 2D driven cavity with an existing efficient N–S solver on non-uniform space grids.

(ii) To explore some physical insight into the corner vortices in the 2D vis a vis 3D driven cavity by utilizing critical point theory, one of the fundamental concept of topological fluid dynamics.

(iii) To explore flow topology in 3D rectangular driven cavities with extreme details and the existence of "U-shaped and mushroom-shaped vortex structures" in the flow field which are closely associated with transition to turbulence and further probe into their possible connection with TGL vortices.

(iv) To develop some novel theories of Moffatt vortices; topological equivalence, quantification of their centers as fixed points and boundary as

TH-1927_126123012

circle cells.

(v) To establish the finiteness of Moffatt vortices by utilizing some recent advances on geometric theories on incompressible viscous flows. Further, to extend the hypothesis on finiteness of corner vortices to more general situation in steady incompressible viscous flows in bounded domains.

In the process, we endeavour to bridge the gap between two factions of contradicting thoughts by pinpointing what could have possibly gone wrong with the assumptions of the existing theories upon which the conclusion of infiniteness is built.

1.4 The work

The present work is concerned with the theoretical and numerical investigation of corner vortices in 2D and 3D separated flows. The work in this dissertation is broadly divided into two parts. The first part deals with some numerical aspects of corner vortices and the next one deals with the development of some new theories on Moffatt vortices and some other issues related to them which hitherto remained unanswered and unexplored.

In the first part, we investigate the existence of Moffatt vortices in the lid-driven square cavity for a wide range of Reynolds numbers: starting from Stokes flow to a moderately high $Re = 3200$ by utilizing an existing Higher Order Compact (HOC) scheme [78] for the ψ-ω formulation of the N–S equations on non-uniform space grids. The quantification of the corner vortices in succession as Moffatt vortices follows from them adhering to a fixed geometric ratio in sizes and intensities. To the best of our knowledge, this is probably for the first time the vortices in the 2D lid-driven cavity has been resolved and documented with extreme details up to the post-quaternary level, both qualitatively and quantitatively. The accuracy of the scale resolution, particularly close to the corners has been verified by a novel approach to grid independence analysis. The self-similarity of these vortices from fractal point of view has also been observed.

All the previous studies on the cavity flow are confined to either the study of its 2D or 3D configuration in isolation. In the present study, we utilize the critical point concepts from the recent advances in the topological fluid dynamics [36, 62, 97, 136, 148] to gain more physical insights into the corner vortices from the perspective of the flow topology in the 2D vis a vis 3D cavity. The computed flow is post processed to identify critical points in the flow field leading to the prediction of separation, reattachment and vortical structures in the flow field. The limit cycles in the plane of symmetry of the 3D flow representing the vortices are found to be stable ones. The Poincaré-Bendixson formula is used to validate the computed results for the possible number of critical points in the 2D cavity. Further, the birth of a corner vortex preceded by a typical sequence of critical point structures in the light of the work of Perry and Chong [119] is detailed. The topological features of the corner vortices in actual 3D flow and its 2D idealization in the cavity has also been compared. Next, we present a detailed discussion of 3D flow topology in a rectangular cavity with values of Spanwise Aspect Ratio (SAR) ($\equiv$ L : B = 2, 3), subject to a constant velocity on the lid. A careful undermining into the existing literature reveals that most of the studies in the 3D cavity is confined to identifying TGL vortices at moderate Reynolds numbers. The topological construction of the vortical structures were not probed thoroughly. In the current study, we attempt to explore the dynamics of TGL vortices by a rigorous topological theory [36, 62, 97, 136, 148] in the 3D lid-driven cavity flow. The "U-shaped and mushroom-shaped vortex" structures also have been observed in the flow field through the visualization of λ_2 isosurfaces. These structures are closely related to transition to turbulence and henceforth with TGL vortices.

The second part of the work consists of the development of some theories on Moffatt vortices in incompressible viscous flows in bounded domains. Firstly, we propose two topological equivalence classes of Moffatt vortices: one through the notion of orientation-preserving homeomorphism and other by the concept of critical point theory [8, 9, 43, 52, 101, 122]. We further quantify the centers of vortices as fixed points through Brouwer fixed-point theorem [52] and define boundary of a vortex as circle cell.

The highlight of this dissertation is however the development of a series of proofs establishing the finiteness of Moffatt vortices. Till date, the sequence of vortices present in the solid corners of steady internal viscous incompressible flows, widely known as Moffatt vortices was thought to be infinite. However, the already existing and most recent geometric theories on incompressible viscous flows [97] that express vortical structures in terms of critical points in bounded domains, indicate a strong opposition to this notion of infiniteness. In this study, we endeavor to bridge the gap between the two opposing stream of thoughts by addressing what might have gone wrong and pinpoint the shortcomings on the assumptions of the existing theorems on Moffatt vortices. We provide our own set of proofs for establishing the finiteness of the sequence of Moffatt vortices by making use of the continuum hypothesis [12, 146] and Kolmogorov length scale [6, 46, 68], which guarantee a non-zero scale for the smallest vortex structure possible in incompressible viscous flows. We point out that the notion of infiniteness resulting from discrete self-similarity of the vortex structures is not physically feasible. With the aid of our new developments and making use of some existing theorems in topology [8, 52, 101] along with some elementary concept of mathematical analysis [123], we provide several approaches to delve into this issue. All these approaches converge to the same conclusion that the sequence of Moffatt vortices cannot be infinite; in fact it is at most finite. We further extend the above mentioned work on the finiteness of vortices to the more general situation in steady incompressible viscous flows in bounded domains.

1.5 Organization of the thesis

The present dissertation has been organized in eight chapters. In chapter 2, we quantify the existence of corner vortices as Moffatt in the lid-driven square cavity for Stokes flow and moderate Reynolds numbers by using an efficient transient N–S solver on compact non-uniform space grids. In chapter 3, we endeavour to gain some physical insight into the corner vortices from the perspective of the flow topology in the 2D vis a vis 3D driven cavity by employing some recent development in the field of topological fluid dynamics. Chapter 4 presents a detailed discussion on flow topology in the 3D lid-driven cavity; in particular the dynamical structures of TGL vortices. In chapter 5, we developed some novel theories on Moffatt vortices which have been used in the subsequent chapters. In chapter 6, we establish the finiteness of Moffatt vortices which in the existing literature has always been synonymous with the existence of an infinite sequence of corner vortices. In chapter 7, we extend the work presented in chapter 6 on the finiteness of vortices in corners to the more general situation in steady incompressible viscous internal flows. Chapter 8 summarizes and comments on the whole work and outlines the future directions of the thesis.

TH-1927_126123012

Chapter 2

QUANTIFICATION OF CORNER EDDIES AS MOFFATT IN THE 2D LID-DRIVEN CAVITY FLOW BY AN HOC APPROACH

2.1 Introduction

The lid-driven cavity flow is probably the most celebrated problem [22, 41, 48, 130] in the field of computational fluid dynamics (CFD). The popularity of this problem stems from the fact that it displays almost all fluid mechanical phenomena for incompressible viscous flows in the simplest of geometric settings. It has been primarily used as a benchmark problem for validating simulations resulting from the numerical solutions of the Navier–Stokes (N–S) equations that govern the physics in incompressible viscous flows. Because of the frequency of use and enormous number of papers being published on this topic, it has almost reached the status of an *overstudied* problem. However, many facets of this problem still remain to be addressed by the scientific community, particularly the characterization of the corner vortices. In the current study, we explore the possibility of categorizing the corner vortices for this

प्रौद्योगिकी संस्थान गुवाहाटी
Indian Institute of Technology Guwahati

flow as the so-called Moffatt vortices within numerical framework [1].

The existence of a sequence of vortices at the corner of solid structure for internal flows with decreasing size and rapidly decreasing intensity towards the corner has been indicated by physical experiments and mathematical asymptotics [108, 140]. Such vortices, for Stokes flow between two solid boundaries was first established theoretically by H. K. Moffatt [106, 107] and are fittingly referred to as "Moffatt vortices" in the existing literature. Following this, the existence of Moffatt vortices in slow viscous incompressible flows on different geometries [5, 15, 30, 54, 82, 86, 87, 99, 100, 106, 107, 128, 129] has so far been established mostly through theoretical studies. There have been very few experimental and numerical studies [15, 30, 39, 57, 140] on this topic. Most theoretical studies on Moffatt vortices seek the solution of the biharmonic form of the N–S equations for Stokes flow [115]

$$\nabla^4\psi = 0, \tag{2.1}$$

which is a linear one. The solution is assumed to be of the form $\psi = \tilde{r}^{\Lambda} f(\phi)$ leading to an equation in f [115]

$$f'''' + \left\{(\Lambda+1)^2 + (\Lambda-1)^2\right\} f'' + (\Lambda+1)^2(\Lambda-1)^2 f = 0, \tag{2.2}$$

resulting in a solution of the form [106, 107, 115, 132]

$$f(\phi) = C_1 \sin(\Lambda-1)\phi + C_2\cos(\Lambda-1)\phi + C_3\sin(\Lambda+1)\phi + C_4\cos(\Lambda+1)\phi, \tag{2.3}$$

where $C_1,\ C_2,\ C_3$ and C_4 are arbitrary constants and Λ is some exponential power of the distance $\tilde{r}$ from the corner. This Λ was found to be a complex number when the angle between the two planes does not cross a certain limit, implying infinite oscillations, i.e. an infinite sequence of counter-rotating eddies as the corner is approached. The sizes and intensities of two successive vortices in this sequence asymptotically approach a fixed ratio.

The numerical computation of incompressible viscous flows essentially con-

---

[1] Parts of this work have been published in (i) *Journal of Physics: Conference Series* [16] and (ii) *Computers and Mathematics with Applications* [17].

sists of solving the N–S equations which provide a framework for exploring different facets of the vortex dynamics. As mentioned earlier, the study of Moffatt vortices has been confined mainly to Stokes flow. The mention of Moffatt vortices in the numerical computation of incompressible fluid flow for moderate Reynolds numbers dates back to the work of Burgraff [24] in 1966, who besides computing the lid-driven square cavity flow, provided a linearized analysis of circular eddies. In 1967, Pan and Acrivos [114] computed flow in rectangular cavities and made use of interpolation techniques to locate the strength and location of tertiary vortices and eventually calculate the common ratio of the vortex sizes.

In their work, Collins and Dennis [30] used a second-order central difference formula in finite difference set up for numerically computing the corner vortices in the flow through a curved tube of triangular cross-section. They endeavoured to achieve the theoretical limits of the intensity and size ratio of the vortices through their numerical studies. Nonetheless, instead of computing the entire flow in the physical domain, they were extrapolating data from the bigger vortices to compute the smaller ones in succession as done by Pan and Acrivos [114]. In 2004, Biswas *et al.* [15] employed the SIMPLE algorithm [117] on a finite volume set up for computing flow in the backward-facing step problem. However, their quantification of Moffatt vortices at the corner was confined to the mention of finding multiple vortices at the backward step corner and the possibility of its existence as $Re \to 0$ only. Recently, Magalhães *et al.* [98] compared the Stokes flow parameters found by Moffatt [106, 107] with the data available from last possible corner vortices for a single Reynolds number value 1000 through an adaptive mesh finite volume computation. Likewise, Biswas and Kalita [16] initiated a study to quantify the corner vortices for the same flow as Moffatt; however it was confined to $Re = 100$ only.

The objective of the current study is to rigorously explore the prospect of quantifying the corner vortices in the famous lid-driven square cavity problem as Moffatt: whether it exists only for Stokes flow or flows at moderate and high Reynolds numbers also. The essential problem with the characterization of vortices as Moffatt eddies lies in finding the asymptotic relation between successive vortices. However, in the numerical framework, no matter how strong the computational resources are, it is impossible to obtain data for the extreme end of the sequence of vortices. As the vortices of greatest interest are the weakest ones belonging to this extreme end, it is highly unlikely that numerical studies alone will be sufficient to answer these questions. As such, the current study is more an endeavour towards establishing Moffatt-likeness of the sequence of vortices in the pre-asymptotic regime. Within the limitations of the computational resources available at our disposal, we would explore the possibility of characterizing these vortices as Moffatt based on the first few corner vortices that has been possible to capture through the current computation.

It is well known that in order to capture the vortices in the extreme corners belonging to the sequence of Moffatt vortices, one not only needs a strong numerical scheme, but also the finest grids possible in the neighbourhood of the corners. In order to accomplish this, we utilize the recently developed Higher Order Compact (HOC) scheme by Kalita *et al.* [78] on non-uniform grids with extreme clustering. Computation of incompressible viscous flows by HOC scheme [72, 75, 76, 77, 78] has gained momentum over the past few years owing to their computational efficiency. Though these schemes have been widely used for the numerical simulation of a host of fluid flow problems, to the best of our knowledge, no HOC scheme has yet been utilized for analyzing the existence of Moffatt vortices, more so for the lid-driven cavity flow. The simulation prompted us to explore a broad categorization of the corner vortices, whose dimensions and intensities in succession should ideally fall off in geometric progression with fixed geometric ratios for them to qualify as Moffatt. The self-similarity property from fractal geometry [2, 11, 14] also has been observed among them. We further introduce a novel approach to grid independence studies in order to confirm that the smallest scales captured by us are not numerical artefacts.

2.2 Problem description

The N–S equations are the governing equations for an incompressible viscous flow situation which in non-dimensional primitive-variable form under suitable boundary conditions are given by

$$\frac{\partial u}{\partial x}+\frac{\partial v}{\partial y}=0, \tag{2.4}$$

$$\frac{\partial u}{\partial t}+u\frac{\partial u}{\partial x}+v\frac{\partial u}{\partial y}=-\frac{\partial p}{\partial x}+\frac{1}{Re}\nabla^2 u, \tag{2.5}$$

$$\frac{\partial v}{\partial t}+u\frac{\partial v}{\partial x}+v\frac{\partial v}{\partial y}=-\frac{\partial p}{\partial y}+\frac{1}{Re}\nabla^2 v, \tag{2.6}$$

Here, u and v are the velocities along the x- and y- directions respectively, t is the time and p is the pressure. In the above equations, Re is the Reynolds number defined by UL/ν, where ν is the kinematic viscosity of the fluid, U is the velocity of the lid, L is the characteristic length and $\nabla^2 \equiv \frac{\partial^2}{\partial x^2}+\frac{\partial^2}{\partial y^2}$. Introducing streamfunction ψ and vorticity ω, the above equations transform to [146]

$$\omega_t-\frac{1}{Re}(\omega_{xx}+\omega_{yy})+(u\omega_x+v\omega_y)=0, \tag{2.7}$$

$$\psi_{xx}+\psi_{yy}=-\omega(x,y), \tag{2.8}$$

with

$$u=\psi_y,\ v=-\psi_x \quad \text{and} \quad \omega=v_x-u_y. \tag{2.9}$$

The classical lid-driven square cavity problem is one of the most extensively solved problems in CFD which essentially deals with numerically solving the two-dimensional (2D) N–S equations in a square cavity. Figure 2.1(a) shows a simple 2D lid-driven cavity defined on $0 \leq x, y \leq 1$. This 2D configuration may be considered as the idealization of the flow in the plane of symmetry in a three-dimensional (3D) lid-driven rectangular cavity with infinite span-wise length. Such a flow can be visualized in figure 2.1(b), where one can see the flow in the plane of symmetry of a 3D rectangular cavity with span-wise aspect ratio two. All the walls of the cavity are stationary except the top

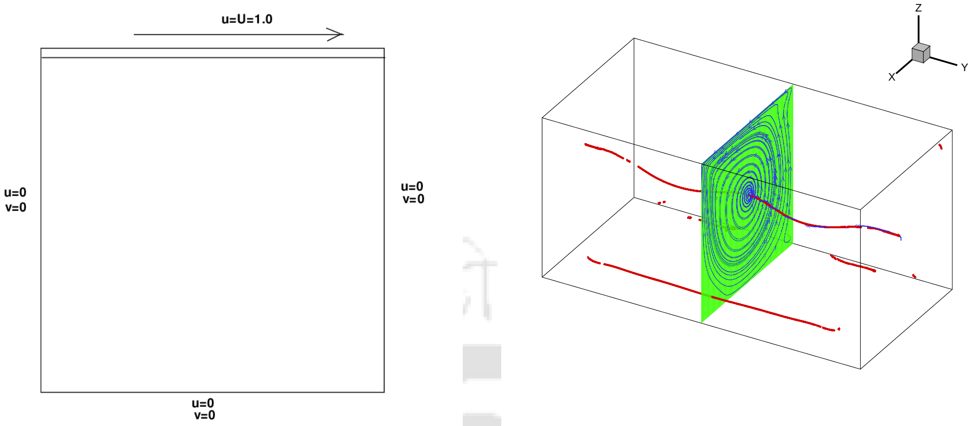

(a) (b)

Figure 2.1: *Lid-driven square cavity (a) 2D and (b) 3D.*

wall at $y = 1$ which moves from left to right setting the fluid into motion. The no-slip condition at the boundary walls requires the velocities to be zero except on the top wall where the non-dimensional x-velocity equals the wall velocity $u = U = 1.0$. The momentum in the x-direction diffuses in the transverse direction towards the interior of the cavity owing to viscosity. After a while, this sets the fluid in the whole cavity into motion. As the Reynolds number increases, highly complex flow patterns arise. A large primary vortex (or eddy) occurs at relatively low Reynolds number; smaller vortices, known as secondary, tertiary, quaternary etc. occur at bottom left and bottom right corners of the cavity as the Reynolds number increases. Thus, a sequence of vortices, ranging from the primary eddy having the dimension of the cavity to the smaller ones starts developing at high Reynolds numbers. The current study endeavours to delve into certain aspects of these vortices – in particular, carefully quantifying the size and intensity ratios of the first few vortices.

2.3 Basic formulations and numerical procedures

2.3.1 The Numerical scheme

The unsteady two-dimensional convection-diffusion equation for a flow variable ϕ in some continuous domain can be written as

$$b\frac{\partial \phi}{\partial t} - \nabla^2\phi + c(x,y,t)\frac{\partial \phi}{\partial x} + d(x,y,t)\frac{\partial \phi}{\partial y} = f(x,y,t), \tag{2.10}$$

where $b > 0$ is a constant, c and d are the convection coefficients in the x- and y-directions, respectively, and f is a forcing function. The $(9,9)$ HOC scheme by Kalita *et al.* [78] for this equation on non-uniform space grid is given by:

$$\begin{aligned}
&b[1 + (H_1 + H_2c)\delta_x + (K_1 + K_2d)\delta_y + \{H_2 - 0.5(x_f - x_b)(H_1 + H_2c)\}\delta_x^2 \\
&+\{K_2 - 0.5(y_f - y_b)(K_1 + K_2d)\}\delta_y^2]\delta_t^+\phi_{ij}^n \\
&+[-A_{ij}\delta_x^2 - B_{ij}\delta_y^2 + C_{ij}\delta_x + D_{ij}\delta_y + G_{ij}\delta_x\delta_y - H_{ij}\delta_x\delta_y^2 - K_{ij}\delta_x^2\delta_y - L_{ij}\delta_x^2\delta_y^2]\phi_{ij}^n \\
&= F_{ij},
\end{aligned} \tag{2.11}$$

with

$$H_1 = \frac{1}{6}\{2(x_f - x_b) - cx_fx_b\}, \quad H_2 = \frac{1}{24}\{2(x_f^2 + x_b^2 - x_fx_b) - cx_fx_b(x_f - x_b)\}$$

and

$$K_1 = \frac{1}{6}\{2(y_f - y_b) - dy_fy_b\}, \quad K_2 = \frac{1}{24}\{2(y_f^2 + y_b^2 - y_fy_b) - dy_fy_b(y_f - y_b)\},$$

where $x_f,\ x_b$ are the forward and the backward step lengths in the x-direction given by $x_f = x_{i+1,j} - x_{i,j}$ and $x_b = x_{i,j} - x_{i-1,j}$, and $y_f,\ y_b$ represent the same in the y-direction; $\delta_x,\ \delta_y$ are the first-order and $\delta_x^2,\ \delta_y^2$ are the second-order central difference operators in the x- and y-directions with step lengths $h = (x_f + x_b)/2$ and $k = (y_f + y_b)/2$ respectively; δ_t^+ denotes the forward difference operator for time with uniform time step Δt and n represents the time level; expressions for the coefficients A_{ij}, B_{ij}, C_{ij}, D_{ij}, G_{ij}, H_{ij}, K_{ij}, L_{ij} and F_{ij}, and other details can be found in the work of Kalita *et al.* [78].

2.3.2 Solution of algebraic systems

The system of equations (2.11) associated with the HOC finite difference on non-uniform grid can be written in matrix form as

$$A\mathbf{\Phi^{n+1}} = \mathbf{f}(\mathbf{\Phi^{n}}), \tag{2.12}$$

where the coefficient matrix A is an asymmetric sparse matrix. For a grid of size $m \times n$, A has a dimension mn, and $\mathbf{\Phi^{n+1}}$ and $\mathbf{f}(\mathbf{\Phi^{n}})$ are mn-component vectors.

The next step involves solving equation (2.12) with iterative methods. Note that the coefficient matrix A is not generally diagonally dominant, which prevents the use of conventional iterative methods such as Gauss-Seidel. While use of uniform grids results in some of the associated matrices to be symmetric and positive definite, and allows implementation of algorithms like conjugate-gradient (CG) [81], a non-uniform grid invariably leads to non-symmetric matrices. As such, in order to solve these systems, the hybrid biconjugate gradient stabilized method (BiCGStab) [81] is used here both with and without preconditioning. Preconditioning was particularly useful for high Reynolds numbers using finer grids with extreme clustering where we have used the Lis library [1].

The streamfunction-vorticity (ψ-ω) formulation (equations 2.7-2.9) of the N–S equations is numerically solved by employing an outer-inner iteration procedure. While an outer iteration consists of solving the discretized versions of equations (2.7)-(2.9) at each time step, the inner iterations within an outer iteration step involves solving the matrix equations resulting from the discretization of (2.7) and (2.8) by BiCGStab [81]. Note that equation (2.10) represents (2.7) and (2.8) with adjustment of the coefficients. As such, in a typical outer temporal cycle, equation (2.7) is discretized using (2.11) with $b = Re$, $c = Re\ u$, $d = Re\ v$ and $f = 0$ in (2.10). Then we discretize (2.8) using the steady-state form of (2.10) with $c = d = 0$ and $f = -\omega$ (see ref. [77]). Once (2.7)-(2.8) are solved, u and v are computed using a fourth-order compact formula (see ref. [75]) for (2.9). This constitutes one outer iteration cycle. For the outer iterations, we used time steps varying from $\Delta t = 10^{-2}$ to 10^{-6} with higher Reynolds numbers at finer grid requiring much smaller time steps.

All of our computations were carried out on a Intel Core i5 based PC with 3GB RAM. For the inner iterations, the computations were stopped when the Euclidean norm of the residual vector $\boldsymbol{r} = \boldsymbol{B} - A\boldsymbol{\phi}$ ($\boldsymbol{B} = \boldsymbol{f}(\Phi^n)$) arising out of equation (2.12) fell below 10^{-13}. The time-marching steady-state solution was assumed to reach when the maximum ω-error between two successive outer temporal iteration steps was smaller than 0.5×10^{-13}.

2.3.3 Clustered grid generation

The theory of Moffatt vortices states that the vortices at the corners reduce in size and intensity by adhering to a geometric ratio. Keeping this in mind, it is essential that the regions in the neighbourhood of the solid boundaries have enough points for resolving the small scales accurately. Therefore, we have used a clustered grid in the vicinity of the corners. Care has been taken to meet the Kolmogorov length scale criteria $\delta \sim Re^{-0.5}$ and $h^* \sim Re^{-0.75}$ where δ and h^* are the boundary layer thickness (non-dimensional) and distance between a wall and the point closest to it respectively [37, 130]. To generate a centro-symmetric grid with clustering near the walls, we use the stretching function [78]

$$x_i = \frac{i}{i_{max}} - \frac{\lambda}{2\pi} \sin\left(\frac{2\pi i}{i_{max}}\right), \ 0 \le \lambda < 1 \tag{2.13}$$

in both x- and y-directions. Here λ is the clustering parameter which determines the intensity of clustering along the walls: the higher the value of λ, the greater the intensity of clustering.

In figures 2.2(a)-(c), we exhibit several clustered grids on the bottom right corner of the cavity generated by the above formula (equation (2.13)) on two different grid sizes in order to demonstrate the effect of λ. The significance of the parameter λ can be gauged from figure 2.2(d) where one can see the

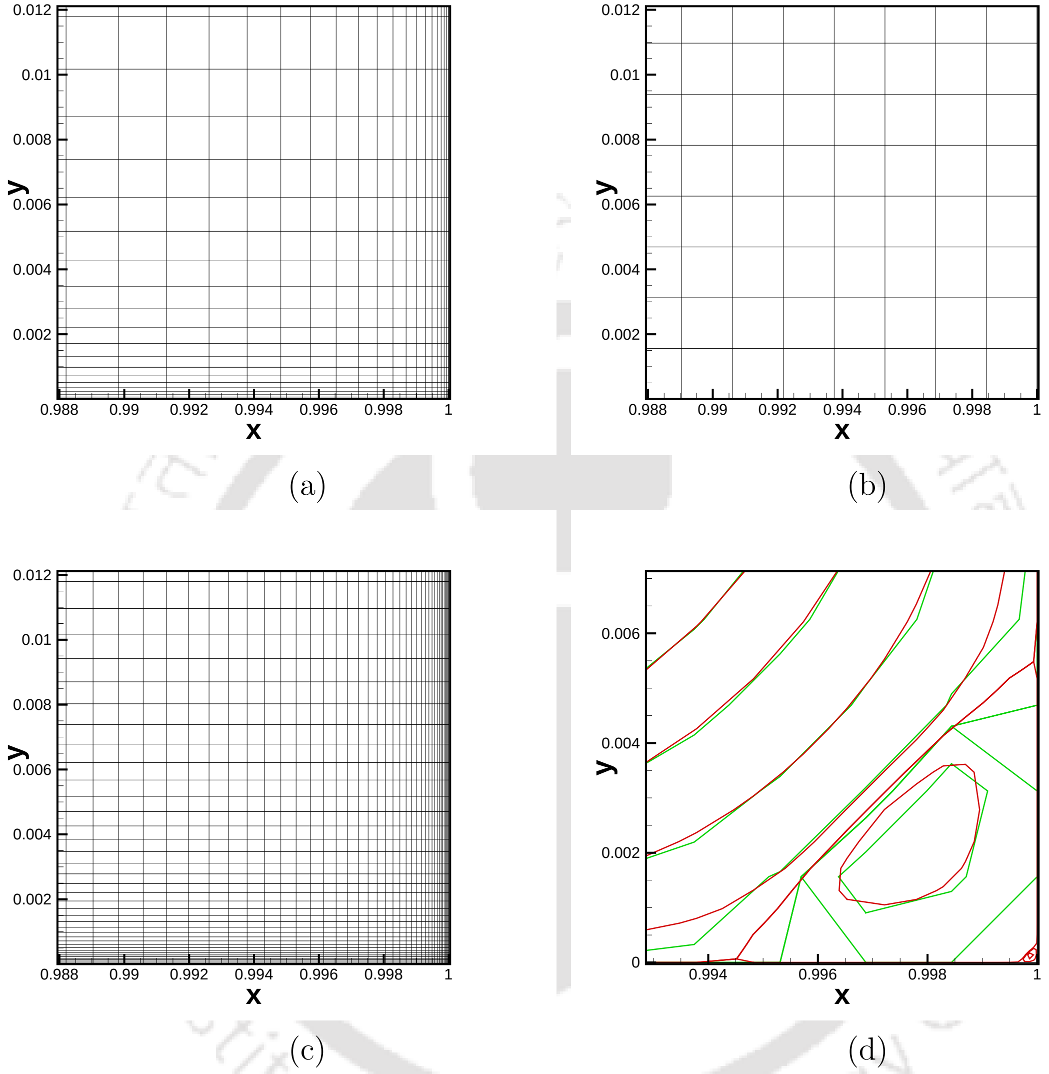

(a) (b)

(c) (d)

Figure 2.2: *Typical clustered grids at the bottom right corner: (a)* $161 \times 161,\ \lambda = 0.99$, *(b)* $321 \times 321,\ \lambda = 0.5$, *(c)* $321 \times 321,\ \lambda = 0.99$ *and (d) tertiary and quaternary vortices for Stokes flow on grids with* $\lambda = 0.5,\ 321 \times 321$ *(green lines) and* $\lambda = 0.99,\ 161 \times 161$ *(red lines).*

streamlines at the bottom right corner of the cavity for Stokes flow computed on two grids, viz., 161×161 with $\lambda = 0.99$ and 321×321 with $\lambda = 0.5$ corresponding to figures 2.2(a)-(b) respectively. While a higher value of $\lambda = 0.99$ on a relatively coarser grid renders severe clustering at the corner (figure 2.2(a)), a moderate value of $\lambda = 0.5$, even on a finer grid, makes it resemble a uniform grid (figure 2.2(b)). It is clear from the figure 2.2(d) that the finer grid despite having double the number of points than the coarser one in each x- and y-directions, was not able to capture the quaternary vortex, which the coarser one could accomplish with ease. The reason for this is obvious from figures 2.2(a)-(b); one can clearly see that the 321 × 321 grid in figure 2.2(b) does not have enough points to resolve the quaternary vortex at the extreme right corner. Therefore throughout all the computations, we have used $\lambda = 0.99$ for all the Reynolds numbers considered here. Note that for the largest Reynolds number Re considered for the current study is 3200 for which $h^* = 3.14 \times 10^{-5}$ which corresponds to figure 2.2(c) and it is well within the range of the Kolmogorov length scale.

2.3.4 Approximation of the vorticity boundary conditions

The boundary conditions for velocity on the top wall of the cavity are given by $u = 1$, $v = 0$. On the other walls the velocities are zero i.e, $u = 0$, $v = 0$. For ψ-ω formulation, along all the four walls streamfunction values are set as zero i.e, $\psi = 0$. For vorticity the following fourth-order accurate approximation [78] has been used on the left wall:

$$\delta_t^+ \omega_{0j} = \frac{1}{Re}\left[\frac{24}{x_f^3}\delta_x^+\psi + \frac{12}{x_f^2}\omega + \frac{4}{x_f}\delta_x^+\omega + \delta_y^2\omega - \delta_x^+\delta_y^2 v\right]_{0j}$$

where δ_x^+ is the forward space-difference operator; the suffixes 0 and j (varying from 0 to y_{max}) stand for x-direction index and the y-direction index respectively. Boundary conditions for vorticity on the other walls have been used in a similar fashion.

2.4 Grid independence and benchmarking

One noticeable fact from the current study is that the sizes and the intensities of the vortices under observation are extremely small. As such, one needs to establish that the computed solution is not a spurious one or not numerical artefact. In order to accomplish that, firstly we carry out a grid independence study for the Reynolds numbers at the high end and further compute the pressure gradients along the left and right wall of the cavity to verify that the number of vortices exactly matches the number of its change of sign.

2.4.1 Grid independence analysis

In figures 2.3 and 2.4, we present the horizontal velocities along the vertical centerline and vertical velocities along the horizontal centerline for $Re = 1000$ and $Re = 3200$ respectively. We have also plotted the famous results of Ghia *et al.* [48] along with our results, where one can see an excellent match. Besides, the overlapping of the graphs for grids of sizes 161×161 and 321×321 clearly indicates the grid independence of our results.

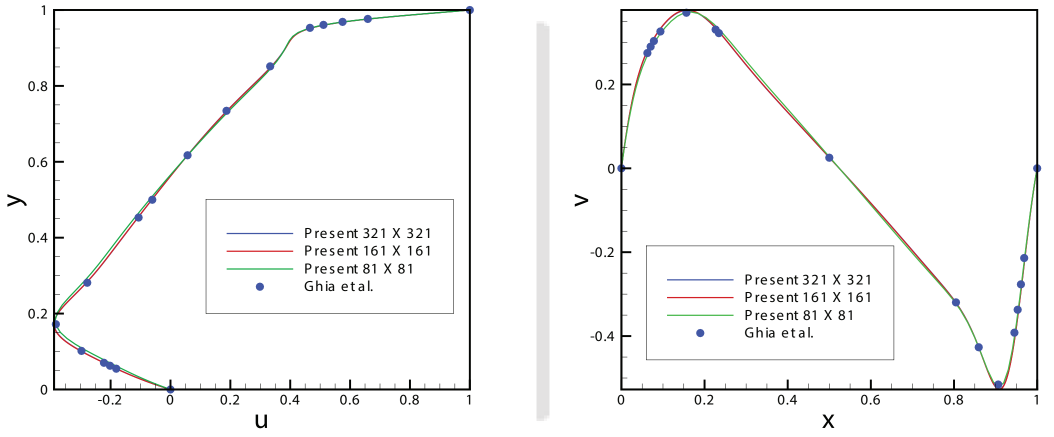

(a) (b)

Figure 2.3: *Grid independence study for* $Re = 1000$*: (a) Horizontal velocity along the vertical centerline and (b) vertical velocity along the horizontal centerline.*

However, as observed by Kalita [71], grid independence studies solely based on the computed values of the flow variables at certain portions of the physical domain sometimes may not reflect the true accuracy of the solution. Since the quantification of Moffatt vortices entirely depends upon the corner vortices, it is imperative that grid independence be specifically sought in the neighbourhood of those regions. In order to show that grid independence has also been achieved at these corners, the vortices are plotted in figure 2.5 on two grids,

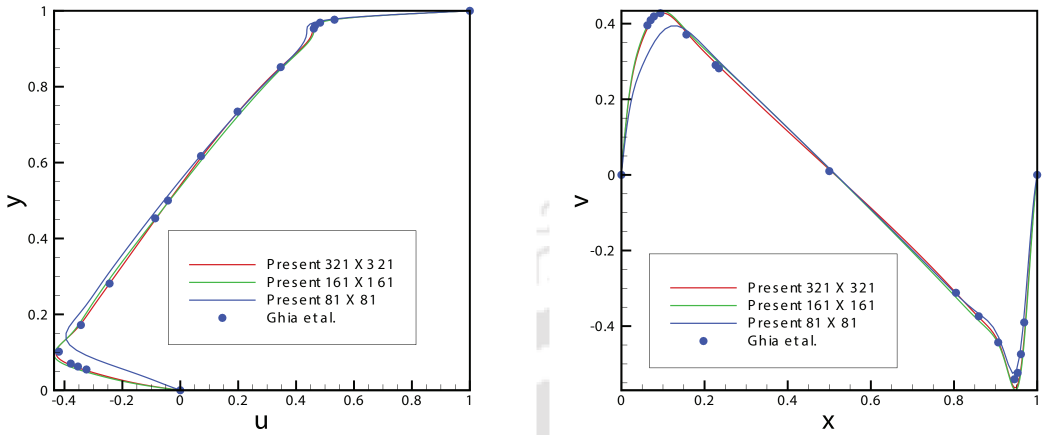

(a) (b)

Figure 2.4: *Grid independence study for* $Re = 3200$*: (a) Horizontal velocity along the vertical centerline and (b) vertical velocity along the horizontal centerline.*

viz., 161×161 and 321×321 using the same streamfunction values at each of the frames (more details in figure 2.16). Here the solid and dotted lines represent positive and negative ψ-values respectively. Figure 2.5(a) shows the streamlines in the bottom left corner: the tertiary and quaternary vortices on the left and secondary and tertiary vortices on the right panel. Likewise 2.5(b) shows the streamlines in the bottom right corner: the secondary and tertiary vortices on the left, tertiary and quaternary vortices in the middle and quaternary and post quaternary vortices in the right panel. It is heartening to see that even in the smallest of scales, some of which are of the order 10^{-13}, extreme closeness of the streamfunction values is achieved. A similar conclusion can be drawn for the computed solution for the other Reynolds numbers as well.

Moreover, we compare the data for the corner vortices (see the schematic in figure 2.6) for $Re = 1000$ on the finest grid with the recent study of Magalhães *et al.* [98] in table 2.1[2]. Despite being computed on a finite difference set up, our results are extremely close to the ones computed on a finite volume set up

---

[2] Note that there was a typographical error in [98] for BL3 center location data which has been confirmed by the corresponding author of [98]. The one presented here is the correct one.

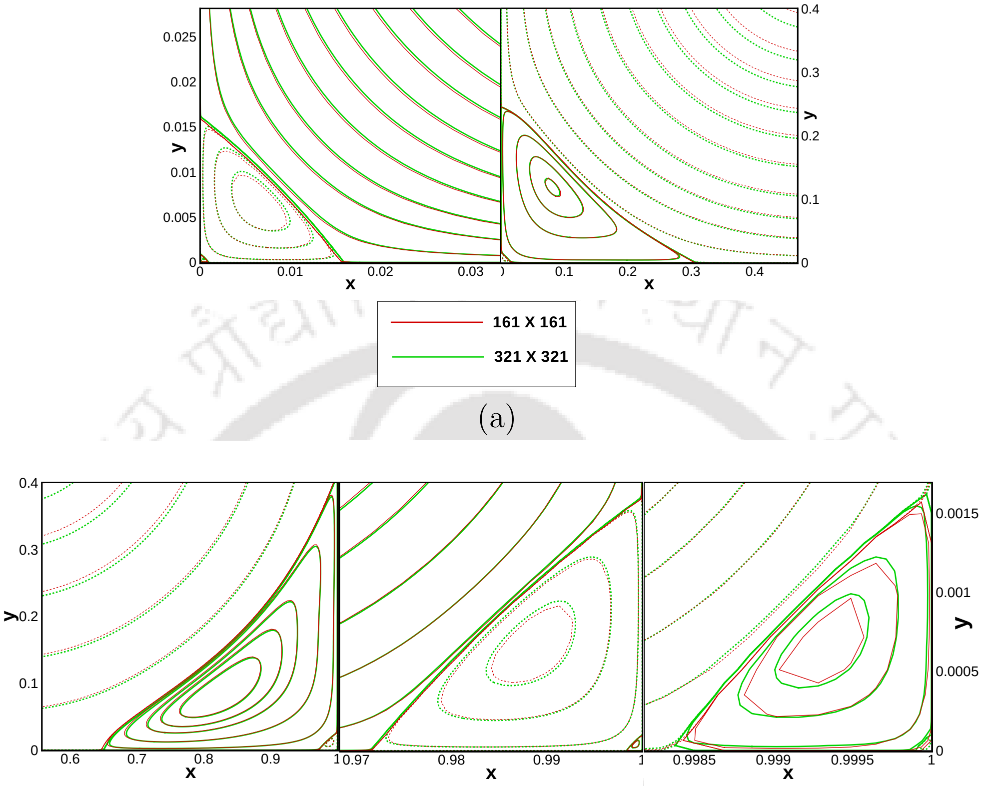

(a)

(b)

Figure 2.5: *Grid independence analysis at the corners: (a) Streamlines at bottom left corner and (b) streamlines at bottom right corner for* $Re = 3200$ *on grids of sizes* 161×161 *and* 321×321*.*

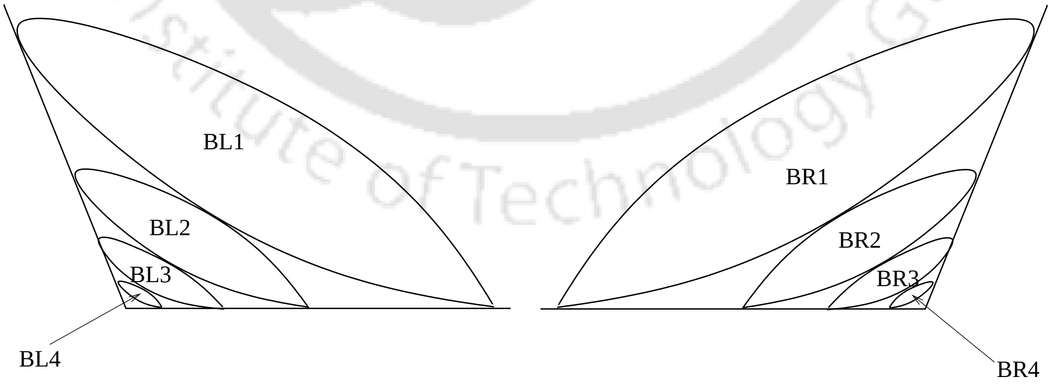

Figure 2.6: *Schematic of the corner vortices at the bottom left and bottom right of the cavity.*

using an adaptive mesh.

Table 2.1: *Comparison of corner vortex data for Re* = 1000 *with Magalhães et al. [98].*

Vortex	**Ref.**	**Center location**	**X, Y separation**
BL1	Present	(0.08333, 0.07757)	0.22714, 0.17090
	Magalhães *et al.*[98]	(0.08317, 0.07708)	0.22335, 0.16800
BL2	Present	(0.00470, 0.00470)	0.01179, 0.01179
	Magalhães *et al.*[98]	(0.00441, 0.00424)	0.01068, 0.01038
BL3	Present	(0.00028, 0.00028)	0.00072, 0.00071
	Magalhães *et al.*[98]	(0.00025, 0.00025)	0.00065, 0.00064
BR1	Present	(0.86570, 0.11281)	0.69652, 0.36597
	Magalhães *et al.*[98]	(0.86576, 0.11364)	0.69495, 0.36817
BR2	Present	(0.99261, 0.00739)	0.98144, 0.01853
	Magalhães *et al.*[98]	(0.99323, 0.00727)	0.98339, 0.01759
BR3	Present	(0.99957, 0.00042)	0.99886, 0.00114
	Magalhães *et al.*[98]	(0.99958, 0.00042)	0.99895, 0.00107
BR4 (Trace Fig.2.11 (b))	Present	(0.99996, 3.143e-5)	0.99993, 6.428e-5
	Magalhães *et al.*[98]	(0.99997, 2.68e-5)	0.99991, 8.25e-5

2.4.2 Pressure gradient observation

Next, we move to the computation of pressure gradients along the left and right walls for which we have utilized the y- momentum equation of the N–S equation. By use of no-slip condition [146] along the walls, the y-momentum equation (2.6) reduces to

$$\frac{\partial p}{\partial y} = \frac{1}{Re}\frac{\partial^2 v}{\partial x^2} \tag{2.14}$$

We use a one-sided first-order finite difference formula to discretize equation (2.14). For the left and right wall, we have used forward and backward difference formula respectively.

$$\text{For the left wall : } \left.\frac{\partial p}{\partial y}\right|_{0,j} = \frac{2}{Re}\left(\frac{x_2 v_{1,j} - x_1 v_{2,j} + (x_2 - x_1)v_{0,j}}{x_1 x_2 (x_1 - x_2)}\right) \tag{2.15}$$

$$\text{For the right wall : } \left.\frac{\partial p}{\partial y}\right|_{i_{max},j} = \frac{2}{Re}\left(\frac{x_2 v_{i_{max}-1,j} - x_1 v_{i_{max}-2,j} + (x_2 - x_1)v_{i_{max},j}}{x_1 x_2 (x_1 - x_2)}\right) \tag{2.16}$$

where, $x_1 = \Delta x_1$ and $x_2 = \Delta x_1 + \Delta x_2$ ($\Delta x_i = x_{i+1} - x_i$, x_i being the i-th point along x-direction).

It is well known that whenever the pressure gradient changes its sign, separation in the flow takes place paving the way for the creation of a vortex [49, 146]. As such, the number of eddies will depend on the total number of changes of sign in pressure gradient. Figures 2.7-2.10 depict the pressure gradient along the left and right walls of the cavity for $Re = 0.001,\ 100,\ 400,\ 1000$ and 3200 on grid of size 321×321. In these figures PL and PR denote the pressure gradient along the left and right wall of the cavity respectively; PL1, PL3, PR2, PR4 denote the points where pressure gradient changes its sign from negative to positive whereas PL2, PL4, PR1, PR3 denote the points having undergone a change of sign from positive to negative. Some of these points in the vicinity of the corner are extremely close to each other and as such it is almost impossible to have a global view of all of them together. Therefore, such regions have been magnified in order to have a clear view of them (see the encircled portions in Figures 2.7-2.10). Note that the same trend is observed on all three grids used in the computation.

As mentioned earlier, the total number of eddies is equal to the total number of changes of sign in pressure gradient; for a particular Reynolds number, in all three grids used, the number of changes in sign along a particular wall is always equal to the number of eddies captured in that corner corresponding to that wall. This fact assures us that small scales have been resolved very accurately and our computed solution is not spurious.

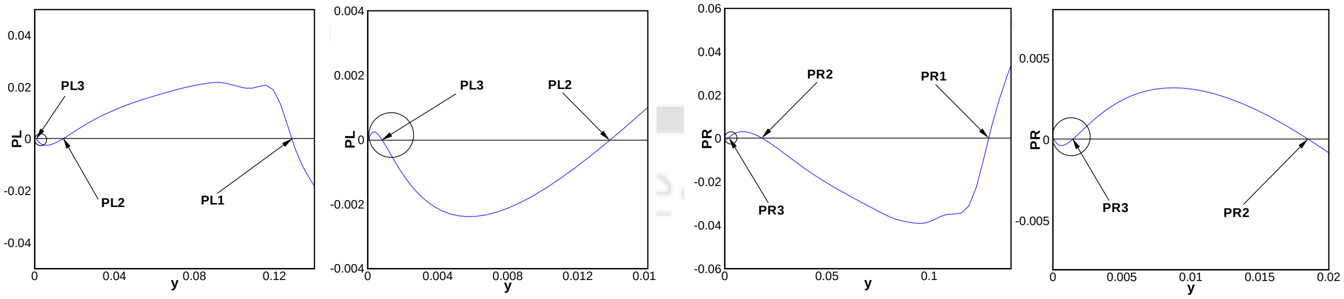

(a) (b)

Figure 2.7: *Pressure gradient along the (a) left wall and (b) right wall for* $Re = 100$ *on grid of size* 321×321.

Although generation of more vortices are expected through grid refinement, we observe that mere refinement of the grid will not help as the appearance of

TH-1927_126123012

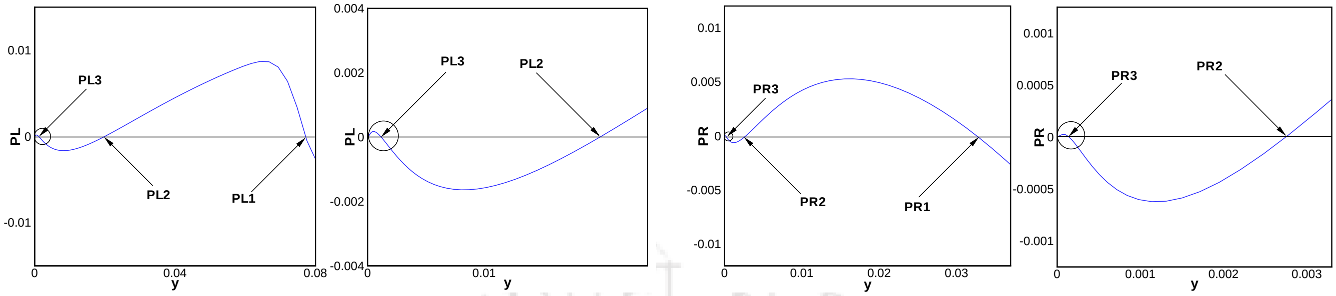

(a) (b)

Figure 2.8: *Pressure gradient along the (a) left wall and (b) right wall for* $Re = 400$ *on grid of size* 321×321.

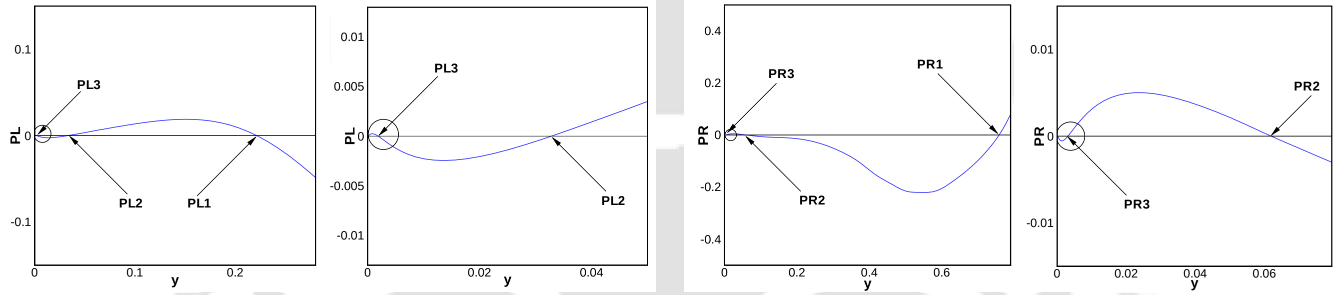

(a) (b)

Figure 2.9: *Pressure gradient along the (a) left wall and (b) right wall for* $Re = 1000$ *on grid of size* 321×321.

the vortices under consideration at the corner depends on fixed geometric ratio of sizes. The grid refinement must be able to generate sufficient points inside the smaller scales for their accurate resolution. For example, for $Re = 100$, the point of separation of the quaternary vortex on the right wall is at a distance 0.00051 from the corner. Assuming a fixed geometric ratio between two consecutive Moffatt vortices in the sequence, which turns out to be 0.058, the next vortex will have its separation point on the wall lying at a distance 3.39×10^{-5} from the corner. Note that on the 321×321 grid used in our computation, the first point nearest to the corner on the right wall lies at a distance 3.14×10^{-5} from the corner. As such there will be only one point inside the estimated separation length (length of the separation point from the corner) in the computational domain which is not good enough for capturing the next vortex (see figure 2.11(a)). Likewise for $Re = 1000$, the point of

TH-1927_126123012

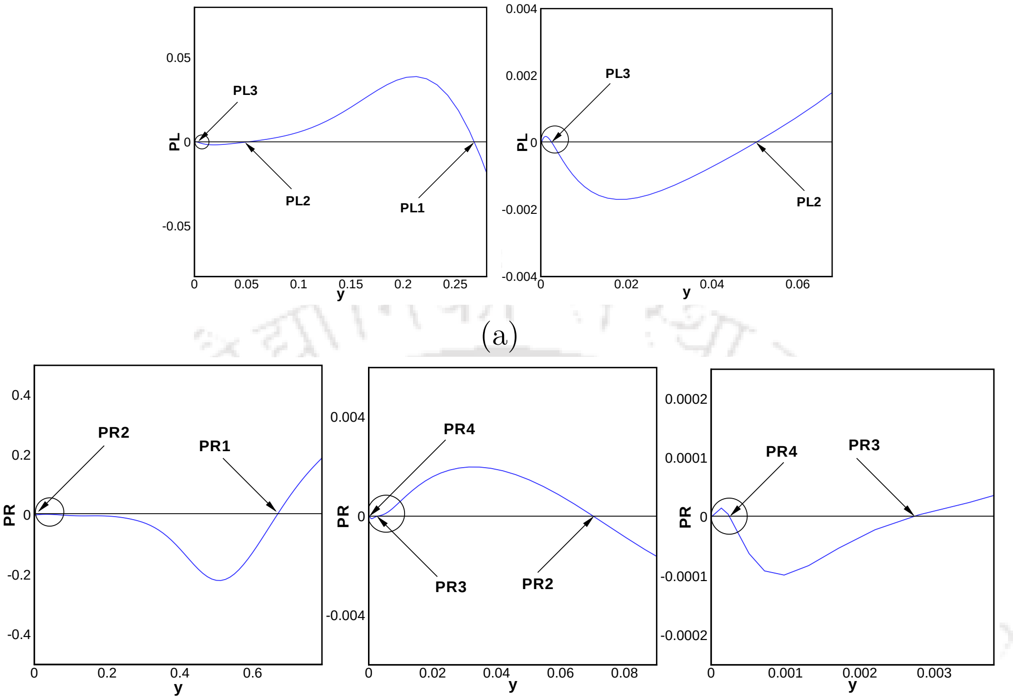

(a)

(b)

Figure 2.10: *Pressure gradient along the (a) left wall and (b) right wall for* $Re = 3200$ *on grid of size* 321×321.

separation of the quaternary vortex is at a distance 0.00136 from the corner and as such the next vortex following the geometric ratio of 0.061 should be at a distance 6.45×10^{-5} from the corner leaving only two points on a 321×321 grid. As such our computation could not capture all the details of this vortex; instead it showed only a trace of it as shown in figure 2.11(b).

2.5 Size and intensity ratios of corner vortices

2.5.1 Corner vortices in the cavity

In order to qualify as Moffatt, the sequence of vortices at specific corners must bear some special characteristics in terms of the size and strength (intensity) which will be described at appropriate junctures. We have computed the flow for a wide range of Reynolds numbers beginning with Stokes flow for $Re < 1$

Indian Institute of Technology Guwahati

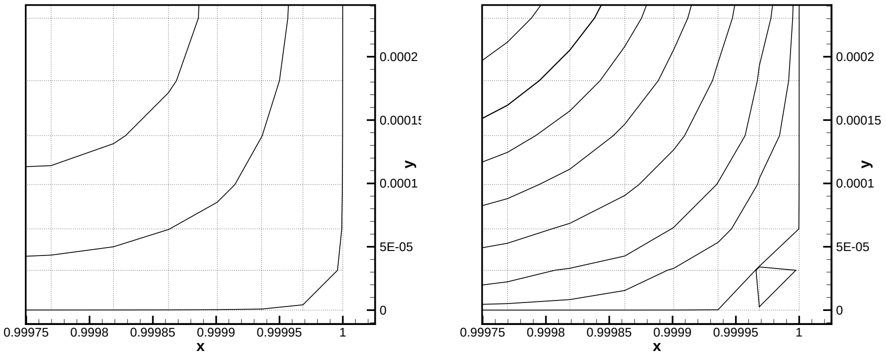

(a) (b)

Figure 2.11: *Streamlines at the extreme bottom right corner of the 2D lid-driven cavity flow (a)* $Re = 100$ *and (b)* $Re = 1000$.

to a high of 3200. As mentioned earlier, it is natural that even the best available computational resources are incapable of capturing many members of the sequence of corner vortices. With the computational resources available to us, we have been able to capture the first few members in that sequence. Those members are presented in terms of streamfunction contours by adopting the following nomenclature (for schematic refer to figure 2.6). For the vortices at the left corner, $BL1$ denotes the secondary vortex which is the first one to appear in the sequence. Likewise, $BL2$, $BL3$, $BL4$, $\cdots$ denote the tertiary, quaternary and post-quaternary vortices respectively in that sequence in the same corner. In a similar way, for the vortices in the right corner, the vortices in the same sequence are denoted by $BR1$, $BR2$, $BR3$, $BR4$, $\cdots$ etc.

In figures 2.12-2.16, we show streamlines on the left and right bottom corners of the cavity resulting from our finest grid computations on a grid of size 321×321 although computations were carried out for Stokes flow ($Re << 1$) and for $Re = 100,\ 400,\ 1000$ and 3200 on grids of sizes 81×81 and 161×161 as well. Multiple frames are used to depict the vortices appearing in the same sequence. In each frame, a pair of vortices gradually decreasing in size is plotted with the next pair appearing side by side in the adjacent frame. The smaller vortex in the previous frame is magnified for clarity in the next frame, which is now the bigger of the two vortices and is marked with arrowheads. For

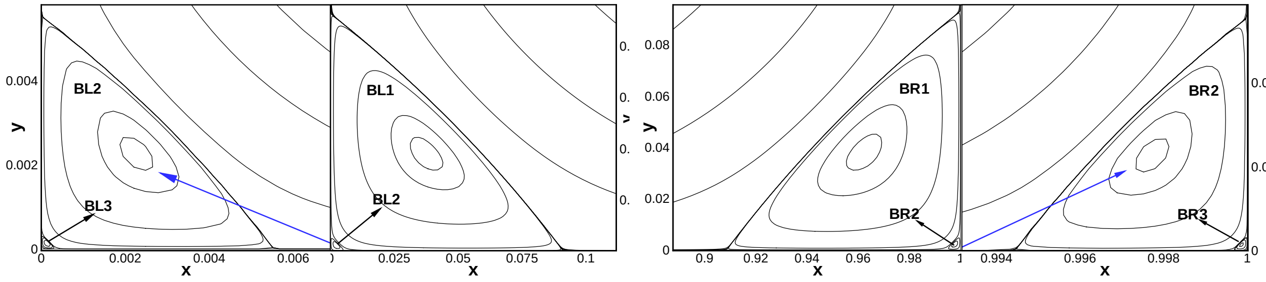

(a) (b)

Figure 2.12: *Corner vortices for Stokes flow on grid of size* 321 × 321*: (a) BL1, BL2, BL3 at the bottom left corner and (b) BR1, BR2, BR3 at the bottom right corner.*

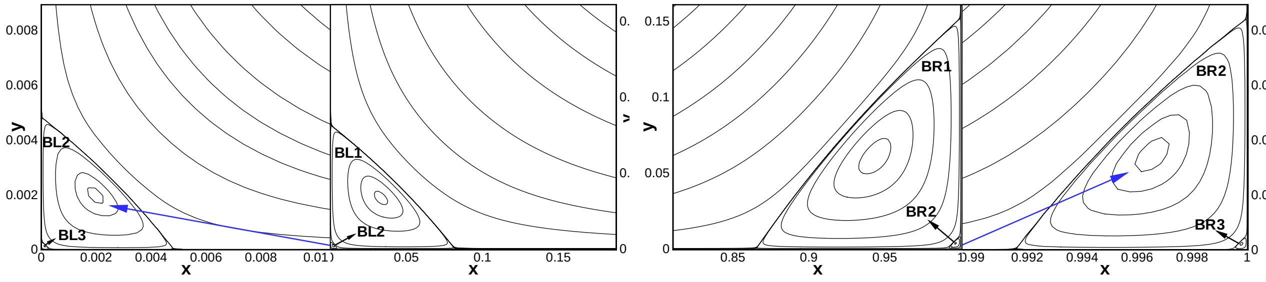

(a) (b)

Figure 2.13: *Corner vortices for* $Re = 100$ *on grid of size* 321 × 321*: (a) BL1, BL2, BL3 at bottom left corner and (b) BR1, BR2, BR3 at bottom right corner.*

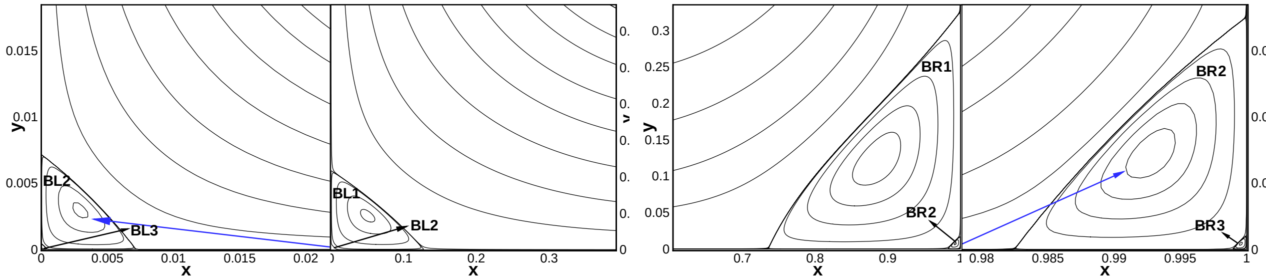

(a) (b)

Figure 2.14: *Corner vortices for* $Re = 400$ *on grid of size* 321 × 321*: (a) BL1, BL2, BL3 at bottom left corner and (b) BR1, BR2, BR3 at bottom right corner.*

TH-1927_126123012

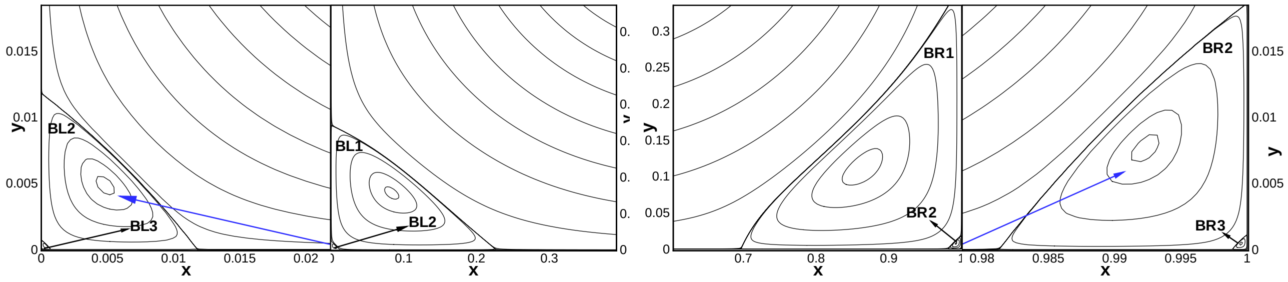

(a) (b)

Figure 2.15: *Corner vortices for Re = 1000 on grid of size 321 × 321: (a) BL1, BL2, BL3 at bottom left corner and (b) BR1, BR2, BR3 at bottom right corner.*

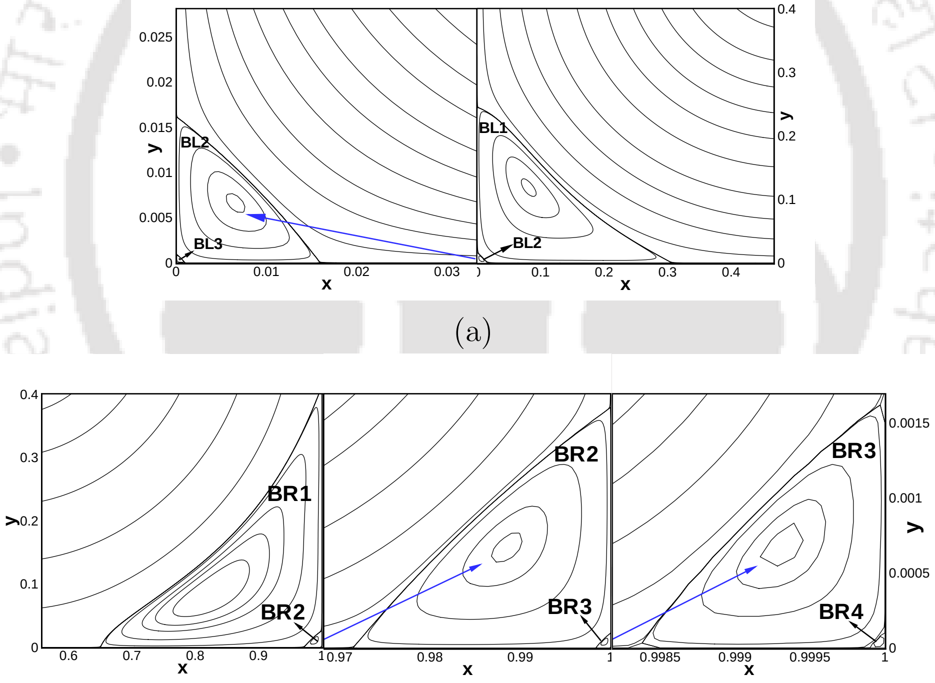

(a)

(b)

Figure 2.16: *Corner vortices for Re = 3200 on grid of size 321 × 321: (a) BL1, BL2, BL3 at bottom left corner and (b) BR1, BR2, BR3, BR4 at bottom right corner.*

example, in figure 2.12(a), the frame on the right depicts the vortices $BL1$ and $BL2$ for the Stokes flow; the smaller vortex $BL2$ in the right frame is magnified in left panel for better visualization of it along with the next vortex, viz., $BL3$

in the sequence. Note that while presenting the vortices, the same length scale has been maintained in all the figures showing two successive vortices both at the left and right corner bearing the same vortex index.

In figure 2.12, we present the three corner vortices captured through our computation for Stokes flow in which one can clearly see the symmetry of the respective vortices at the left and right corner about the vertical centerline. On the other hand no trace of symmetry could be found in the computation for the Reynolds numbers $Re = 100,\ 400,\ 1000$ and 3200 (figures 2.13-2.16). With the exception of $Re = 3200$, it seems that two consecutive vortices in the sequence grows approximately with the same proportion in a particular corner.

A close look at figures 2.13-2.15 will reveal that the ratio of the sizes of $BL1$ to $BL2$ and $BL2$ to $BL3$ are almost the same; the same occurrence is observed for the vortices at the right corners as well. These issues will be addressed more elaborately in the next section (section 2.5.2) wherein we will quantify the ratios of the size and intensity of the first few of these vortices.

2.5.2 Quantification of Moffatt vortices

For our problem, computations were carried out for $Re = 0.001,\ 100,\ 400,\ 1000$ and 3200 on grids of sizes 81×81, 161×161 and 321×321.

The intensity of a vortex is defined by the streamfunction (ψ) value at the center of the vortex as the value of ψ signifies the volume flow [12, 146]. Following the work of H. K. Moffatt [106], we measure the size of a vortex in terms of the distance of the center of the vortex from the corner of the cavity.

In table 2.2, we present the properties such as intensities, location of centers and sizes of Moffatt vortices at the left and right corner of the cavity for Reynolds number $Re = 0.001,\ 100,\ 400,\ 1000$ and 3200 on grids of sizes 81×81, 161×161, 321×321. Ours is one of the very few attempts that could be found in the existing literature providing comprehensive details of the corner eddies with such extreme clustering and as such table 2.2 could prove to be a useful tool for the future researchers for benchmarking their results in lid-driven cavity flow.

Table 2.2: *Properties of secondary (BL1, BR1), tertiary (BL2, BR2), quaternary (BL3, BR3) and post-quaternary (BR4) vortices for the lid-driven square cavity for Re* = 0.001, 100, 400, 1000 *and* 3200 *on grids of sizes 81×81, 161×161, 321×321.*

			Re				
Vortex	**Property**	**Grid**	0.001	100	400	1000	3200
BL1	ψ_{max}	81^2	2.10845e-6	1.50108e-6	1.07568e-5	2.01454e-4	6.21171e-4
		161^2	2.17616e-6	1.79512e-6	1.42228e-5	2.31489e-4	1.04856e-3
		321^2	2.19727e-6	1.55439e-6	1.31597e-5	2.33145e-4	1.05161e-3
	Center (x, y)	81^2	(0.03812, 0.03826)	(0.03465, 0.03464)	(0.05017, 0.04194)	(0.08047, 0.08048)	(0.08053, 0.11954)
		161^2	(0.03819, 0.03819)	(0.03462, 0.03462)	(0.05018, 0.04593)	(0.08042, 0.08042)	(0.08055, 0.11948)
		321^2	(0.03816,0.03816)	(0.03292, 0.03292)	(0.05017, 0.04594)	(0.08333, 0.07757)	(0.08040, 0.11941)
	Size	81^2	0.05401	0.04899	0.06539	0.11381	0.14413
		161^2	0.05401	0.04896	0.06803	0.11373	0.14410
		321^2	0.05397	0.04656	0.06802	0.11385	0.14396
BL2	ψ_{min}	81^2	-4.86629e-11	-3.87426e-11	-2.31442e-10	-5.07863e-9	-1.12757e-8
		161^2	-5.53968e-11	-4.77309e-11	-3.71492e-10	-6.06667e-9	-3.34648e-8
		321^2	-5.98816e-11	-4.07759e-11	-3.57897e-10	-6.13548e-9	-3.81386e-8
	Center (x, y)	81^2	(0.00221, 0.00221)	(0.00220, 0.00220)	(0.00283, 0.00281)	(0.00517, 0.00517)	(0.00518, 0.00518)
		161^2	(0.00221, 0.00221)	(0.00220, 0.00220)	(0.00279, 0.00279)	(0.00517, 0.00517)	(0.00622, 0.00621)
		321^2	(0.00220,0.00220)	(0.00195, 0.00195)	(0.00279, 0.00279)	(0.00470, 0.00470)	(0.00677, 0.00678)
	Size	81^2	0.00312	0.00311	0.00399	0.00731	0.00733
		161^2	0.00312	0.00311	0.00395	0.00731	0.00879
		321^2	0.00311	0.00276	0.00395	0.00665	0.00958
BL3	ψ_{max}	81^2	1.15963e-15	7.68436e-16	4.91105e-15	7.96503e-14	3.03096e-13
		161^2	1.31497e-15	1.26467e-15	9.05603e-15	1.39809e-13	8.58466e-13
		321^2	1.69091e-15	9.62348e-16	1.00124e-14	1.57768e-13	9.38673e-13
	Center (x, y)	81^2	(0.00014, 0.00014)	(0.00013, 0.00013)	(0.00014, 0.00014)	(0.00023, 0.00023)	(0.00035, 0.00035)
		161^2	(0.00014, 0.00014)	(0.00013, 0.00013)	(0.00014, 0.00014)	(0.00023, 0.00023)	(0.00035, 0.00035)
		321^2	(0.00014,0.00014)	(0.00012, 0.00012)	(0.00018, 0.00018)	(0.00028, 0.00028)	(0.00038,0.00039)
	Size	81^2	0.00019	0.00018	0.00019	0.00032	0.00049
		161^2	0.00019	0.00018	0.00019	0.00032	0.00049
		321^2	0.00019	0.00017	0.00025	0.00039	0.00054
BR1	ψ_{max}	81^2	2.10845e-6	1.05658e-5	6.23926e-4	1.69673e-3	2.89686e-3
		161^2	2.22507e-6	1.26505e-5	6.41613e-4	1.72786e-3	2.83868e-3
		321^2	2.22889e-6	1.14526e-5	6.40871e-4	1.73109e-3	2.84563e-3
	Center (x, y)	81^2	(0.96188,0.03826)	(0.94074, 0.05932)	(0.88757, 0.12649)	(0.86586, 0.11941)	(0.81549, 0.09249)
		161^2	(0.96186, 0.03819)	(0.94309, 0.06174)	(0.88777, 0.11936)	(0.86571, 0.11229)	(0.82453, 0.08637)
		321^2	(0.96183,0.03817)	(0.94309, 0.06173)	(0.88422, 0.12302)	(0.86570,0.11281)	(0.82432, 0.08334)
	Size	81^2	0.05401	0.08385	0.16923	0.17959	0.20639
		161^2	0.05397	0.08397	0.16384	0.17505	0.19558
		321^2	0.05398	0.08396	0.16894	0.16896	0.19445
BR2	ψ_{min}	81^2	-4.86629e-11	-2.93590e-10	-1.72460e-8	-4.53019e-8	-2.90829e-7
		161^2	-5.89713e-11	-3.50669e-10	-1.72122e-8	-4.72641e-8	-1.96029e-7
		321^2	-6.08892e-11	-2.93130e-10	-1.81285e-8	-4.87726e-8	-2.12191e-7
	Center (x, y)	81^2	(0.99780, 0.00221)	(0.99653, 0.00346)	(0.99261, 0.00738)	(0.99263, 0.00742)	(0.98642, 0.01359)
		161^2	(0.99779, 0.00221)	(0.99653, 0.00346)	(0.99261, 0.00739)	(0.99263, 0.00741)	(0.98823, 0.01018)
		321^2	(0.99779,0.00221)	(0.99653, 0.00346)	(0.99262, 0.00739)	(0.99261,0.00739)	(0.98819, 0.01097)
	Size	81^2	0.00312	0.00490	0.01044	0.01046	0.01921
		161^2	0.00312	0.00490	0.01045	0.01045	0.01556
		321^2	0.00312	0.00490	0.01044	0.01045	0.01612
BR3	ψ_{max}	81^2	1.15963e-15	3.77053e-15	3.66382e-13	7.92947e-13	7.61207e-12
		161^2	1.31497e-15	9.62741e-15	3.85288e-13	1.09364e-12	4.84358e-12
		321^2	1.69091e-15	7.37723e-15	5.05647e-13	1.33303e-12	4.70625e-12
	Center (x, y)	81^2	(0.99986, 0.00013)	(0.99986, 0.00013)	(0.99965, 0.00035)	(0.99965, 0.00035)	(0.99928, 0.00071)
		161^2	(0.99986, 0.00013)	(0.99976, 0.00023)	(0.99965, 0.00035)	(0.99965, 0.00035)	(0.99928, 0.00072)
		321^2	(0.99986,0.00014)	(0.99979, 0.00020)	(0.99957, 0.00042)	(0.99957, 0.00042)	(0.99939, 0.00061)
	Size	81^2	0.00019	0.00019	0.00049	0.00049	0.00101
		161^2	0.00019	0.00033	0.00049	0.00049	0.00102
		321^2	0.00019	0.00029	0.00060	0.00060	0.00086
BR4	ψ_{min}	81^2	—	—	—	—	—
		161^2	—	—	—	—	—
		321^2	—	—	—	—	-1.74421e-16
	Center (x, y)	81^2	—	—	—	—	—
		161^2	—	—	—	—	—
		321^2	—	—	—	—	(0.99996, 0.00003)
	Size	81^2	—	—	—	—	—
		161^2	—	—	—	—	—
		321^2	—	—	—	—	0.00005

TH-1927_126123012

Table 2.3: *Intensity ratio* (IR) *and size ratio* (SR) *between two consecutive vortices.*

Corner	Re	**Step Size (h)**	IR			SR		
			$BL2 : BL1$	$BL3 : BL2$	$BL4 : BL3$	$BL2 : BL1$	$BL3 : BL2$	$BL4 : BL3$
Bottom Left	0.001	1/80	2.3079e-5	2.3829e-5	–	5.7861e-2	6.3360e-2	–
		1/160	2.5456e-5	2.3737e-5	–	5.7861e-2	6.3360e-2	–
		1/320	2.7252e-5	2.8237e-5	–	5.7647e-2	6.3645e-2	–
		1/640	2.7372e-5	2.8537e-5	–	5.7632e-2	6.3664e-2	–
		$h \to 0$	2.6973e-5	2.7537e-5	–	5.7678e-2	6.3600e-2	–
	100	1/80	2.5809e-5	1.9834e-5	–	6.3496e-2	5.9145e-2	–
		1/160	2.6589e-5	2.6496e-5	–	6.3542e-2	5.9145e-2	–
		1/320	2.6233e-5	2.3601e-5	–	5.9240e-2	6.1639e-2	–
		1/640	2.6209e-5	2.3408e-5	–	5.8953e-2	6.1805e-2	–
		$h \to 0$	2.6288e-5	2.4051e-5	–	5.9908e-2	6.1250e-2	–
	400	1/80	2.1516e-5	2.1219e-5	–	6.0987e-2	4.9649e-2	–
		1/160	2.6119e-5	2.4377e-5	–	5.8007e-2	5.0177e-2	–
		1/320	2.7196e-5	2.7975e-5	–	5.8007e-2	6.4622e-2	–
		1/640	2.7268e-5	2.8215e-5	–	5.8007e-2	6.5585e-2	–
		$h \to 0$	2.7029e-5	2.7416e-5	–	5.8007e-2	6.2375e-2	–
	1000	1/80	2.6699e-5	1.5683e-5	–	6.4239e-2	4.4454e-2	–
		1/160	2.7354e-5	2.3045e-5	–	6.4283e-2	4.4454e-2	–
		1/320	2.8174e-5	2.5714e-5	–	5.8377e-2	5.9434e-2	–
		1/640	2.8229e-5	2.5892e-5	–	5.7983e-2	6.0432e-2	–
		$h \to 0$	2.8047e-5	2.5299e-5	–	5.9295e-2	5.7102e-2	–
	3200	1/80	1.8152e-5	2.6880e-5	–	5.0827e-2	6.7568e-2	–
		1/160	3.1915e-5	2.5653e-5	–	6.0994e-2	5.6320e-2	–
		1/320	3.6266e-5	2.4612e-5	–	6.6556e-2	5.6883e-2	–
		1/640	3.6556e-5	2.4543e-5	–	6.6927e-2	5.6921e-2	–
		$h \to 0$	3.5589e-5	2.4775e-5	–	6.5691e-2	5.6797e-2	–
			IR			SR		
			$BR2 : BR1$	$BR3 : BR2$	$BR4 : BR3$	$BR2 : BR1$	$BR3 : BR2$	$BR4 : BR3$
Bottom Right	0.001	1/80	2.3079e-5	2.3829e-5	–	5.7732e-2	6.1257e-2	–
		1/160	2.6503e-5	2.2298e-5	–	5.7899e-2	6.1120e-2	–
		1/320	2.7318e-5	2.7770e-5	–	5.7981e-2	6.3360e-2	–
		1/640	2.7372e-5	2.8135e-5	–	5.7986e-2	6.3509e-2	–
		$h \to 0$	2.7190e-5	2.6919e-5	–	5.7967e-2	6.3010e-2	–
	100	1/80	2.7787e-5	1.2843e-5	–	5.8438e-2	3.8980e-2	–
		1/160	2.7720e-5	2.7454e-5	–	5.8356e-2	6.7755e-2	–
		1/320	2.5595e-5	2.5167e-5	–	5.8361e-2	5.9184e-2	–
		1/640	2.5453e-5	2.5015e-5	–	5.8361e-2	5.8612e-2	–
		$h \to 0$	2.5925e-5	2.5524e-5	–	5.8359e-2	6.0515e-2	–
	400	1/80	2.7641e-5	2.1244e-5	–	6.1713e-2	4.7396e-2	–
		1/160	2.6826e-5	2.2384e-5	–	6.3789e-2	4.7364e-2	–
		1/320	2.8287e-5	2.7892e-5	–	6.1823e-2	5.7545e-2	–
		1/640	2.8384e-5	2.8259e-5	–	6.1691e-2	5.8224e-2	–
		$h \to 0$	2.8059e-5	2.7035e-5	–	6.2126e-2	5.5850e-2	–
	1000	1/80	2.6699e-5	1.7504e-5	–	5.8233e-2	4.7332e-2	–
		1/160	2.7354e-5	2.3138e-5	–	5.9703e-2	4.7364e-2	–
		1/320	2.8174e-5	2.7331e-5	–	6.1856e-2	5.7506e-2	–
		1/640	2.8229e-5	2.7611e-5	–	6.1999e-2	5.8182e-2	–
		$h \to 0$	2.8047e-5	2.6680e-5	–	6.1519e-2	5.5928e-2	–
	3200	1/80	10.0394e-5	2.6173e-5	–	9.3084e-2	5.2623e-2	–
		1/160	6.9056e-5	2.4708e-5	–	7.9570e-2	6.5416e-2	–
		1/320	7.4567e-5	2.2179e-5	3.7062e-5	8.2897e-2	5.3539e-2	5.7937e-2
		1/640	7.4934e-5	2.2010e-5	–	8.3119e-2	5.2747e-2	–
		$h \to 0$	7.3709e-5	2.2571e-5	–	8.2380e-2	5.5386e-2	–

In table 2.3, we provide the intensity and size ratio between two consecutive eddies for Reynolds number $Re = 0.001,\ 100,\ 400,\ 1000$ and 3200 on step sizes 1/80, 1/160, 1/320, 1/640 and for smaller step size ($h \to 0$) termed as zero-grid-step size. Computations for intensity ratio (IR) and size ratio (SR) were carried out for step sizes 1/80, 1/160 and 1/320. In order to compute the intensity and size ratio for step size 1/640, we extrapolate the size ratio values as well as intensity ratio values on the finest two grids, namely 161×161 and 321×321. We have used Richardson's extrapolation formula [63] for intensity ratio (IR) as well as size ratio (SR) which are given by

$$\text{Improved value of } \ IR = IR(h_f) + \frac{1}{R^m - 1}(IR(h_f) - IR(h_c)) \tag{2.17}$$

$$\text{Improved value of } \ SR = SR(h_f) + \frac{1}{R^m - 1}(SR(h_f) - SR(h_c)) \tag{2.18}$$

where $R = h_c/h_f$, the ratio of the step sizes h_c, h_f on coarser and finer grids respectively and m is the order of accuracy of the numerical method used ($m = 4$ here).

As step size $h \to 0$, the intensity and size ratio is obtained by using Lagrange interpolating polynomial [23]. The interpolation was carried out using three different step sizes namely, $h_1 = 1/160$, $h_2 = 1/320$ and $h_3 = 1/640$ and their corresponding intensity ratio as well as size ratio. The interpolation formulas are given by

$$\begin{aligned} IR(h) \quad &= \frac{(h-h_2)(h-h_3)}{(h_1-h_2)(h_1-h_3)}IR(h_1) + \frac{(h-h_1)(h-h_3)}{(h_2-h_1)(h_2-h_3)}IR(h_2) \\ &+ \frac{(h-h_1)(h-h_2)}{(h_3-h_1)(h_3-h_2)}IR(h_3) \end{aligned} \tag{2.19}$$

$$\begin{aligned} SR(h) \quad &= \frac{(h-h_2)(h-h_3)}{(h_1-h_2)(h_1-h_3)}SR(h_1) + \frac{(h-h_1)(h-h_3)}{(h_2-h_1)(h_2-h_3)}SR(h_2) \\ &+ \frac{(h-h_1)(h-h_2)}{(h_3-h_1)(h_3-h_2)}SR(h_3) \end{aligned} \tag{2.20}$$

2.5.2.1 Stokes flow

This regime is represented by a value $Re = 0.001$. From table 2.3, one can clearly see that successive ratios of size and intensities are very close to each other. The centers of the secondary vortices at the left and right corners are located at $(0.03816, 0.03816)$ and $(0.96183, 0.03817)$ respectively; thus the points are reflection of each other about the vertical centerline; likewise for the centers of the tertiary and quaternary vortices. Moreover, the streamfunction values at the centers of the secondary, tertiary and quaternary vortices in the left corner on the finest grids are 2.20×10^{-6}, -5.99×10^{-11}, and 1.69×10^{-15} respectively, while at the right their values are 2.23×10^{-6}, -6.09×10^{-11}, and 1.69×10^{-15} respectively. These values from table 2.2 reconfirm that the sequence of vortices at the left and right bottom corners are symmetric about the vertical center line through the cavity as can also seen in figure 2.12. All these facts also exemplify the accuracy of our computation.

Note that in Moffatt's original paper [106], an asymptotic limit of the ratio of the size and intensity of the corner vortices was established for Stokes flow only. It was accomplished through the analytical streamfunction solution of the linearized N–S equations in biharmonic form. Accomplishing this for the lid-driven cavity flow in the numerical framework in the asymptotic regime is an impossible task as we were able to generate only three vortices in the sequence for Stokes flow at each corner. However the size ratio between the second and third vortices in the sequence is very close to the value of 0.0614 found for a sharp corner with 90° angle, computed using Moffatt's analytical expression [98, 106].

2.5.2.2 Flow in the moderate Re regime

The range $100 \leq Re \leq 1000$ represents this regime. While the theory [106, 107] predicted rapid decrease in the intensity and size of the vortices for Stokes flow, one can observe from table 2.2 that it holds true for this regime as well. Moreover, for a particular Re, as the grid size increases, both the intensity and the size of any vortex are extremely close even in smaller scales, manifesting accurate resolution of the smaller scales. However, while the intensity ratios for a particular Re at a certain corner are extremely close to each other, the same cannot be said about the ratios of their sizes.

Another interesting observation from table 2.3 is that while the parameters have settled down for the right corner, there still are some fluctuations on the left corner, considering two pairs of vortices in succession on gradually increasing grid size. The reason for this may be because of the unsteady nature of the smallest scales captured through the computation. Note that Chiang and Sheu [28] also observed the same phenomenon in their computation of 3D shear-driven cavity flow.

2.5.2.3 Flow for $Re = 3200$

A close look at tables 2.2 and 2.3 reveals that for $Re = 3200$, neither the intensity nor the size of the vortices maintains a fixed ratio. Thus it appears that if there is a limiting value to these ratios, the first few members of this sequence are not too close to it for this Re and beyond. One can also observe that all vortex details presented for the three grids lean towards a grid independent result. However, on the 321×321 grid, for the quaternary vortices and the vortices after them in the sequence to settle down, a much smaller time step $\Delta t = 10^{-6}$ had to be used. It is worth mentioning that with the increase in the Reynolds numbers, the size of such vortices also increases. Therefore for the reasons mentioned at the end of section 2.4.2, only for $Re = 3200$, the fourth vortex at both the corners could be accurately resolved on the finest grid used in the current study.

2.6 Self-similarity of Moffatt vortices

An important property of fractals [2, 11, 14] is their self-similarity or their symmetry by dilation. *The father of fractal geometry* Benoit Mandelbrot who coined the term *fractal*, perceived that it is extremely difficult to describe nature from the point of view of Euclidean geometry, that is with reference to straight lines, circles, cubes alike. He is the first to contemplate that real objects, such as trees, coastlines, lighting etc. can be explained through fractals and fractal geometry. There are many ways to define a fractal. The simplest way to define a fractal is as an object which appears self-similar under varying finite degrees of magnification . The best way of illustrating the meaning of a fractal object is probably by viewing two ‘natural objects’: an island coastline and a person (see figure 2.17). The zoom into the coastline reveals that its ruggedness is repeated on finer and finer scales, an under re-scaling looks essentially the same: the coastline is a fractal object, however the person is not. As we zoom into various part of the body, we see quite different forms. The hand does not resemble the whole body, the finger nails does not look like the hand and so on.

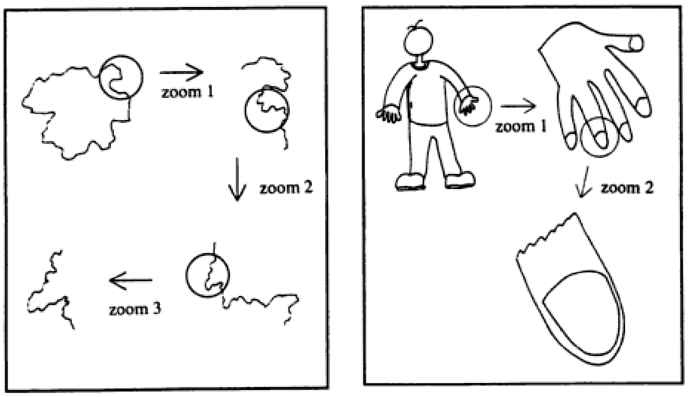

(a) (b)

Figure 2.17: *(a) Coastline: fractal object and (b) person: non-fractal object [2].*

In our work, we present the self-similarity of Moffatt vortices at moderate Reynolds numbers in connection with self-similarity in fractals. Figures 2.18-2.21 describe the self-similarity of those vortices for $100, 400, 1000$ and 3200 on grid of size 321×321.

In these figures, we depict the distribution of vorticities along the left and right wall in the region of existence of Moffatt vortices. Note that a change in sign in vorticity value represents flow separation and hence a new vortex in the sequence. The positive and negative signs of the vorticity correspond to the presence of a counter-rotating and a rotating vortex respectively over the extent of the wall throughout which the vorticity keeps the same sign. The self-similarity in rotation of these vortices can be gauged from the fact that the vorticity curves show the same pattern over the range where it maintains the same sign, albeit as a mirror image of the previous curve in the

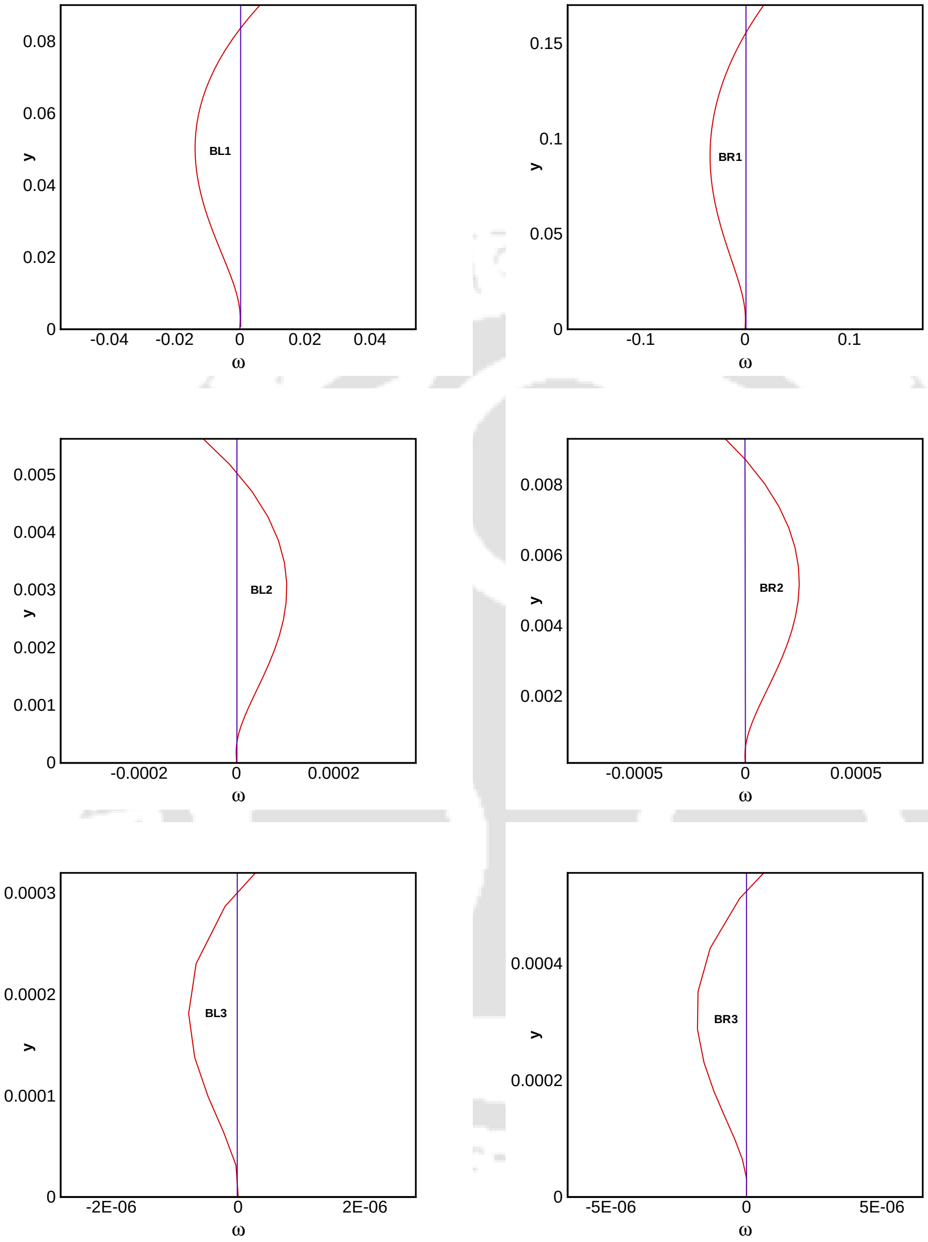

(a) (b)

Figure 2.18: *Self-similarity of Moffatt vortices for* $Re = 100$ *on grid of size* 321×321*: at (a) bottom left and (b) bottom right corner of the cavity.*

sequence about y-axis. For example one can see the curves corresponding to the regions of BL1, BL2 and BL3 for the left corner for $Re = 100$ in figure 2.18(a) and figure 2.18(b) for the right corner. Similar observation follows for

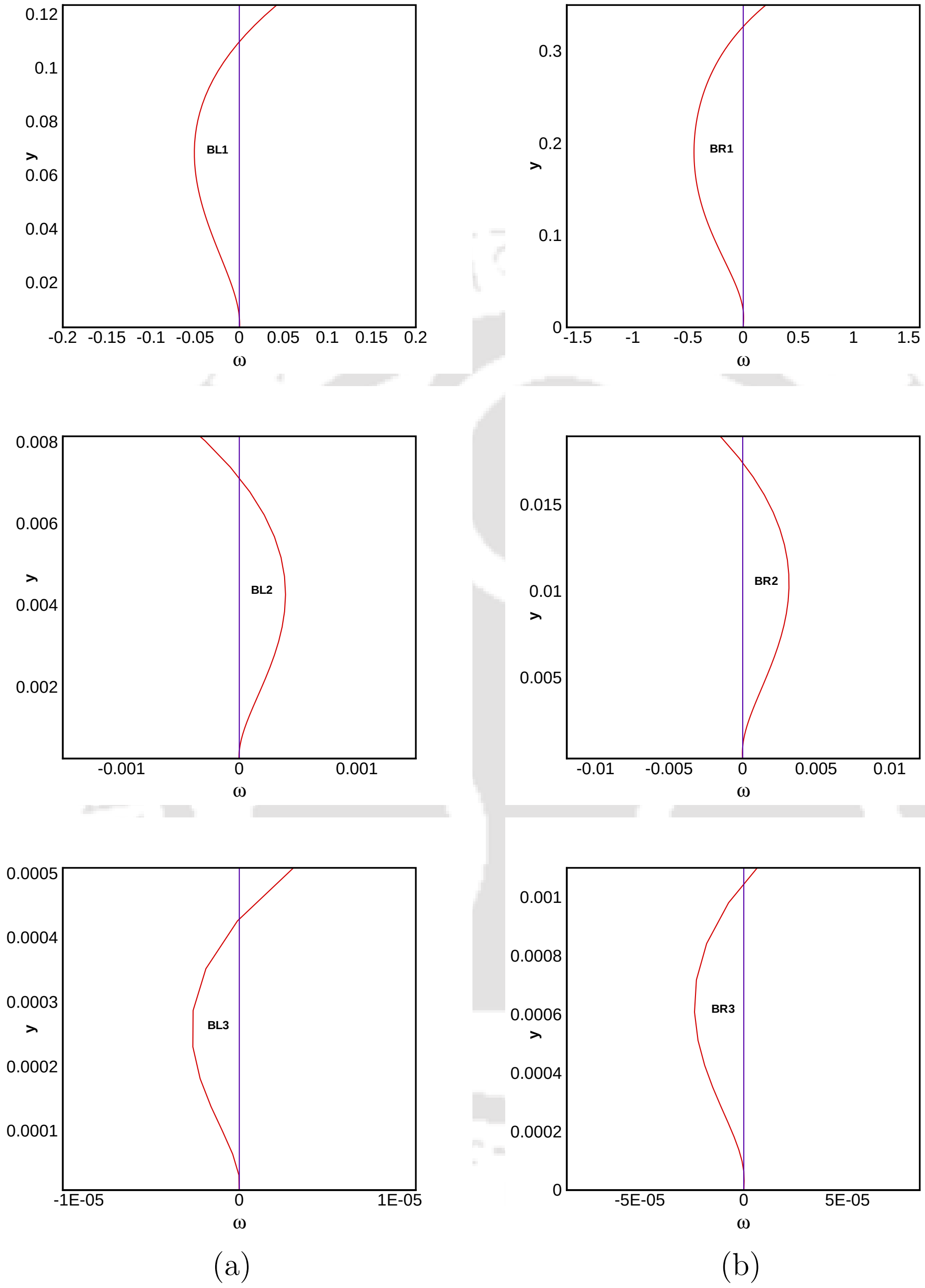

Figure 2.19: *Self-similarity of Moffatt vortices for* $Re = 400$ *on grid of size* 321×321*: at (a) bottom left and (b) bottom right corner of the cavity.*

$Re = 400, 1000, 3200$ in figures 2.19-2.21.

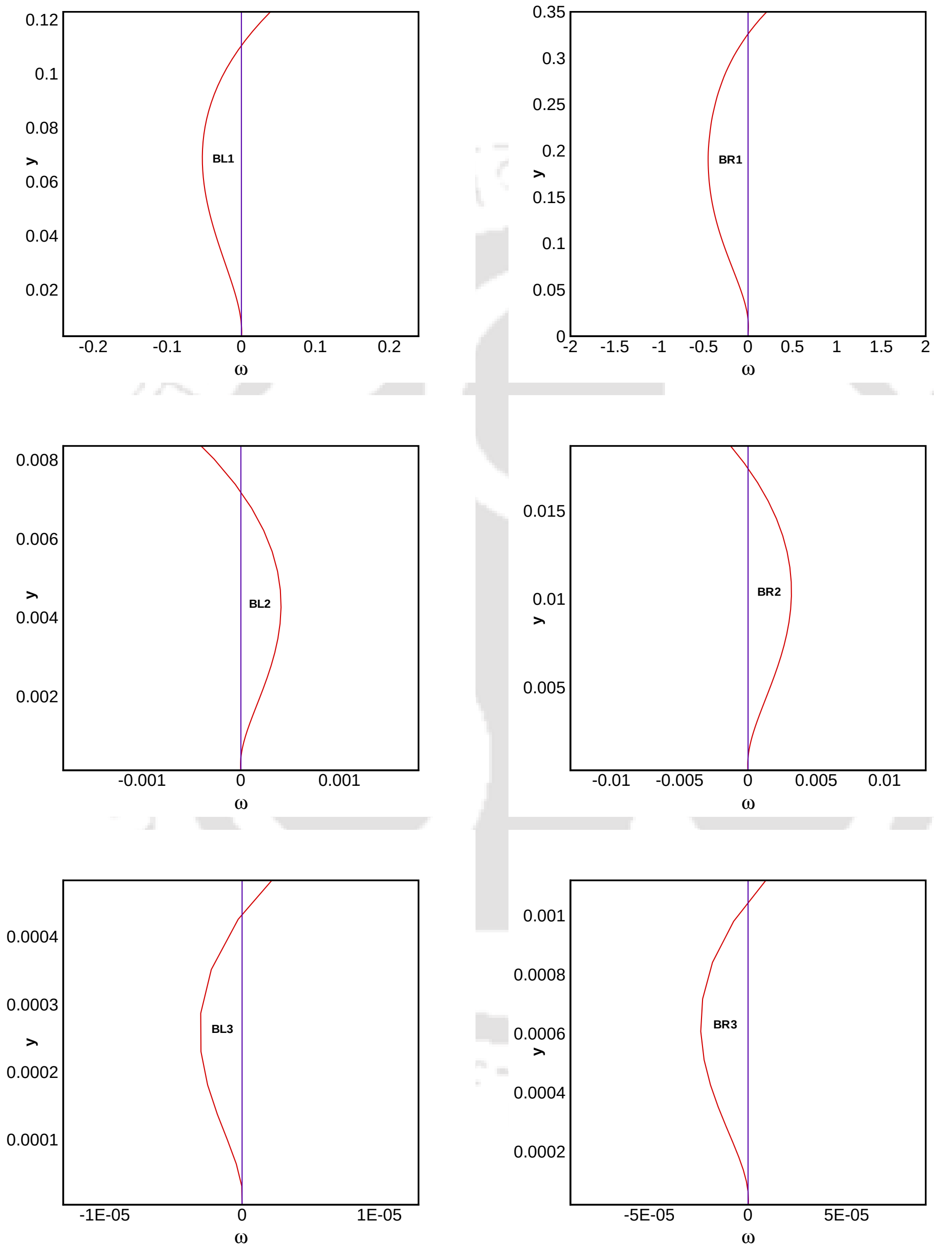

(a) (b)

Figure 2.20: *Self-similarity of Moffatt vortices for* $Re = 1000$ *on grid of size* 321×321*: at (a) bottom left and (b) bottom right corner of the cavity.*

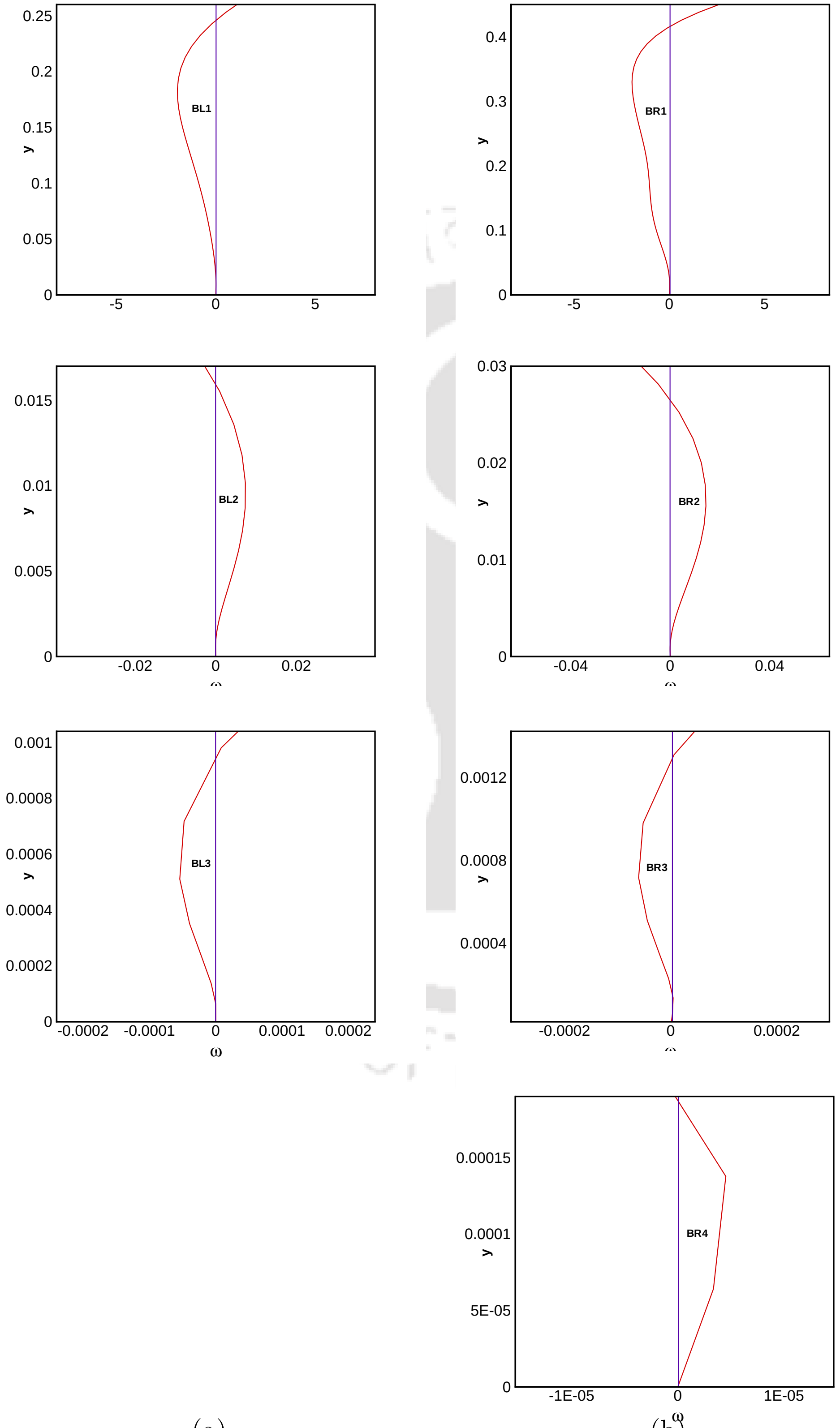

(a) (b)

Figure 2.21: *Self-similarity of Moffatt vortices for Re* = 3200 *on grid of size* 321 × 321*: at (a) bottom left and (b) bottom right corner of the cavity.*

2.7 Conclusion

The current study computes with care and precision, features of corner vortices in lid-driven square cavity flow, examining along the way the intensity and size ratios of successive vortices. In order to compute the flow, a recently developed efficient transient N–S solver is used on compact non-uniform space grids with extreme clustering at the corners. We have explored the possibility of them qualifying as Moffatt vortices for a wide range of Reynolds numbers: starting from the Stokes flow to a moderately high $Re = 3200$. The size and intensities of the corner vortices are measured and their accuracy is further strengthened by extrapolating the computed data on finer grids through Richardson's extrapolation and Lagrange interpolation. This is probably for the first time that the vortices in the 2D lid-driven cavity have been resolved and documented with extreme details up to the post-quaternary level, both qualitatively and quantitatively. As such this study is also an effort towards benchmarking the corner vortex data for the flow under consideration. We further observe that these vortices exhibit self-similarity like a fractal object does. Besides, we have introduced a novel approach to the grid independence analysis where the concept of adverse pressure gradients is used as a tool to validate that the separation zones in the neighbourhood of the corners are consistent with the vortices obtained from the computed solution. This strengthens our case that the smallest scales resulting from the computation are actual physical phenomena, not numerical artefacts.

In the next chapter, these corner vortices in the 2D cavity are analyzed by utilizing critical point theory in the field of topological fluid dynamics. Further, the topology of the same vortices in the 3D cavity across the plane of symmetry are compared with their 2D counterpart.

भारतीय प्रौद्योगिकी संस्थान गुवाहाटी • Indian Institute of Technology Guwahati •

Chapter 3

TOPOLOGY OF CORNER VORTICES IN THE LID-DRIVEN CAVITY FLOW: 2D VIS A VIS 3D

3.1 Introduction

The importance of the lid-driven cavity [22, 41, 48, 130] in the computational fluid dynamics folklore has already been discussed in the previous chapter. The flow in the driven cavity exhibits a plethora of fluid flow characteristics such as vortex dynamics, hydrodynamics instability, bifurcations etc. in the simplest of geometric settings. All these flow characteristics are mainly manifested through the presence of multiple counter-rotating corner eddies at the corners of the cavity depending on the Reynolds number (Re).

It is worth mentioning that in almost all the studies available in literature on this topic, two-dimensional (2D) flows as an idealization of a three-dimensional (3D) ones or 3D flows having symmetry in one direction have been considered. The present study is no different from them where one expects the flow to be exactly the same found in the plane of symmetry of a 3D lid-driven flow in a rectangular cavity with infinite span-wise length. Figure 3.1(a) shows a simple 2D lid-driven square cavity defined on $0 \leq x, y \leq 1$, the configuration of which may be considered as the idealization of the flow in the plane of symmetry in a 3D lid-driven rectangular cavity with infinite span-wise length. Such a flow can be visualized in figure 3.1(b), where one can see the flow in the plane of symmetry of a 3D rectangular cavity with span-wise aspect ratio two.

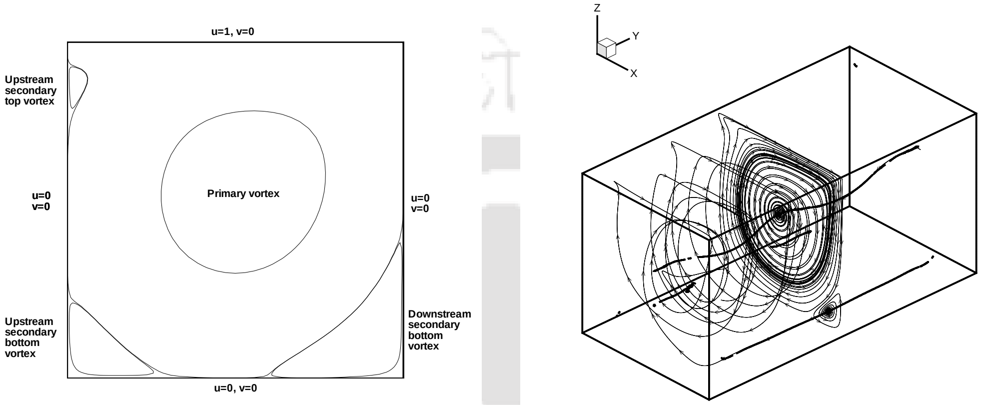

(a) (b)

Figure 3.1: *(a) Configuration of the 2D lid-driven square cavity and (b) typical flow in the plane of symmetry in the 3D cavity produced from our compution.*

Note that all the previous studies on the cavity flow are confined to either the study of its 2D or 3D configuration in isolation. To the best of our knowledge, no study of the cavity flow in the context of 2D vis a vis 3D are available in literature. The objective of the current study is to provide a perspective on the flow topology of the corner vortices of such flow from this angle.

The existence of corner vortices were established by considering cross-sections of the 3D flow. With the advent of more tools for vortex identification leading to the redefinition of a vortex [60] and the recent developments in topological fluid dynamics [36, 62, 97, 136, 148] may reveal some more interesting facets on these vortices. In the following, we present a 2D verses 3D comparison of the corner eddy structures in the lid-driven cavity flow using rigorous topological theory.

For this purpose, we have computed the flow inside a 3D lid-driven rectangular cavity with a spanwise aspect ratio two for $Re = 1000$. The 3D Navier–Stokes (N–S) equations are solved numerically by the commercially available software ANSYS Fluent 15.0 version on non-uniform grids on a grid of size $101 \times 201 \times 101$ (see figure 3.1(b)). The Kolmogorov length scale [37] has been taken care of by taking $h^* = 1.63 \times 10^{-3}$ where h^* is distance between the boundary wall and the point closest to it in the computational domain. The flow inside 2D cavity has been computed by utilizing recently developed $(9, 9)$ Higher-Order Compact scheme by Kalita *et al.* [78] on non-uniform space grid of size 321×321. For the details of numerical scheme and solution procedures, we refer to the aforementioned work of Kalita *et al.* [78].

The next section deals with the dynamical structures in the flow field inside the cavity, namely the critical points and the limit cycles, the identification of which leads to the prediction of separation and reattachment, and vortical structures. After that, we discuss about their topological implications where the Poincaré-Bendixson formula is used to validate the computed results i.e, the number of critical points arising out of our computation in the 2D cavity follow this formula. Further, the birth of a corner vortex preceded by a typical sequence of critical point structures in the light of the work of Perry and Chong [119] is detailed. We also present an overview of the 2D vis a vis 3D flows in the context of the lid-driven cavity.

3.2 Critical points in the flow field

In topological fluid dynamics, the vortical structures in a flow are explained in terms of critical points and limit cycles present in the flow field. Critical points in 3D flows are obtained by finding the fixed points of the trajectories given by

$$\frac{dx}{u(x,y,z)} = \frac{dy}{v(x,y,z)} = \frac{dz}{w(x,y,z)} \tag{3.1}$$

where $\vec{V} = u\hat{i} + v\hat{j} + w\hat{k}$ is the velocity vector in the 3D space (x, y, z). The critical point exists at the points where u, v and w vanish simultaneously. The background behind the characterization of the critical points as nodes, foci and saddles can be found in the work of Deléry [36] and Bakker [9].

In 3D flow domain all forms of critical points including half-saddles, half-nodes and quarter-saddles can be present. However, the surface wall contains only half-saddles and half-nodes, and the corners, quarter-saddles. As such

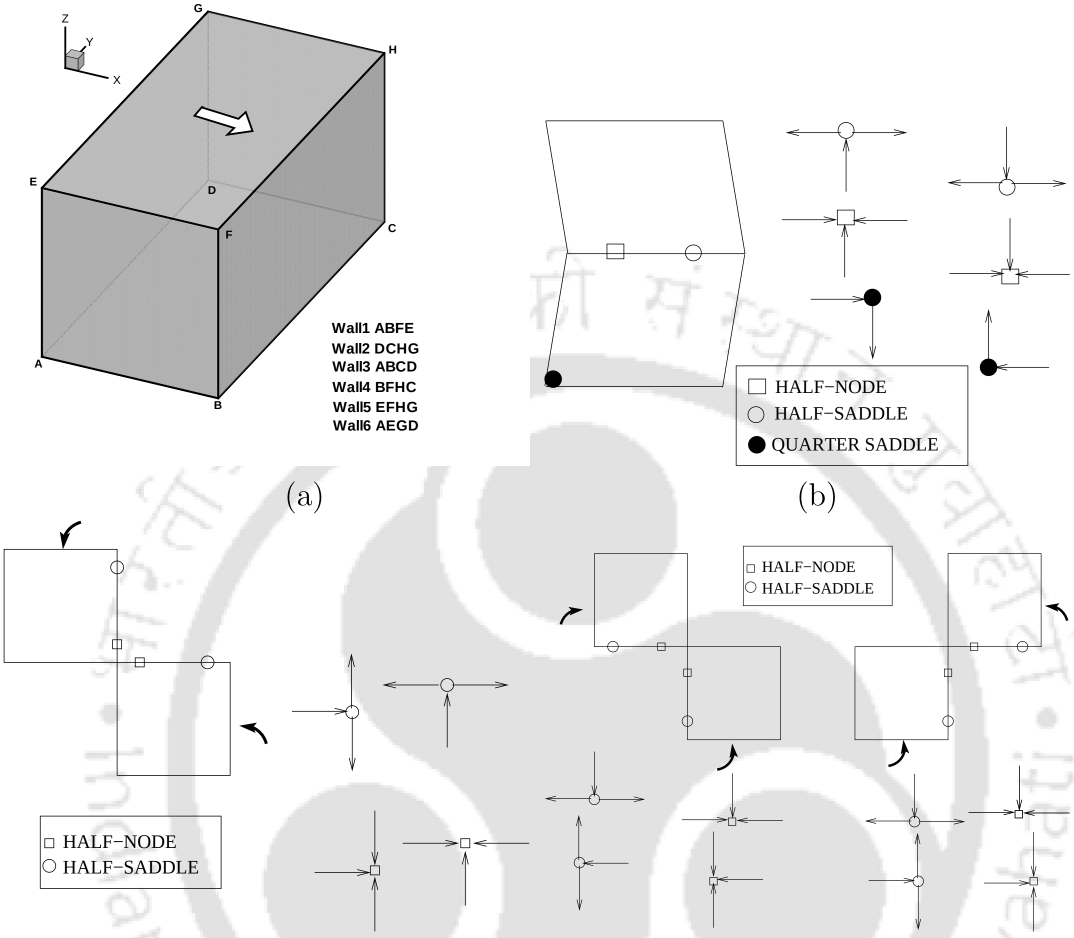

(a) (b)

(c) (d)

Figure 3.2: *(a) Configuration of 3D cavity, (b) Possible half-node, half-saddle scenario on the intersection of walls* 1-3, 2-3, 3-4 *and* 3-6, *(c)* 2-4, *(d)* 6-1 *and* 1-4.

the boundaries cut out from the cross section of the 3D or the ones of the 2D lid-driven cavity contains only half-saddles or half-nodes as critical points. The existence of such points leads to separation and attachment in the flow field, which paves the way for the creation of a new vortex. In figure 3.2(a), we mark the six walls of the 3D cavity and present certain possible half-saddle and half-node scenarios on the edges of the 3D cavity in figures 3.2(b)-(d). For example, figure 3.2(b) is the ideal representation of the walls 1, 2, 4 and 6 with wall 3, while figure 3.2(c) depicts the same for each pair of consecutive vertical walls, with the intersection of each representing the edges. In 2D flow, the scenario will be the same with the sides replacing the edges.

We now present the topology of corner vortices from our 2D computations for $Re = 1000$ in figure 3.3(a) and the flow in the plane of symmetry of the 3D lid-driven cavity in figure 3.3(b).

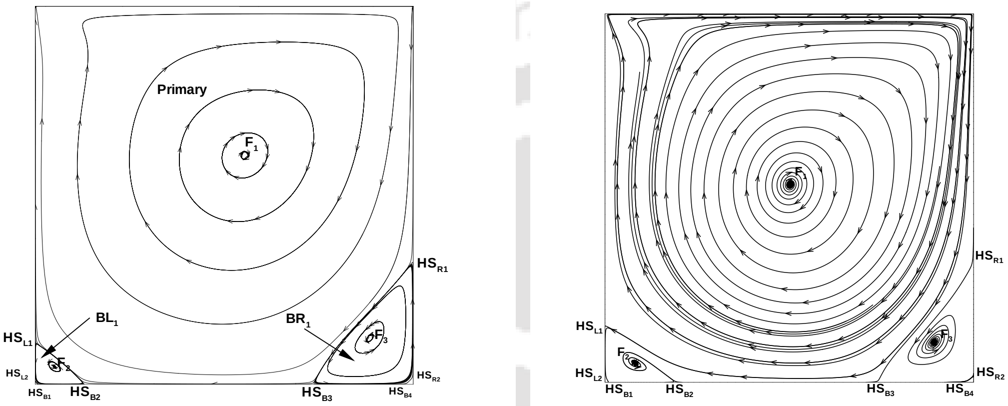

(a) (b)

Figure 3.3: *Critical points in the lid-driven cavity flow for* $Re = 1000$*: (a) 2D computation and (b) 3D computation.*

A close up view of the bottom right corners in these computations can be seen in figures 3.4 and 3.5. In figure 3.4, we reproduce the corner vortices BR_1, BR_2 of figure 2.15(b) with oriented streamlines. A close look at the points denoted by HS_{R1}, HS_{R2}, HS_{B1}, HS_{B2} etc. clearly reveals that all these points follow half-saddle structures. Note that the same point can act as a separation point for one vortex and reattachment point for another. For example HS_{B4} is a point of separation for BR_1 whereas it is a point of reattachment for BR_2. Similarly HS_{R1} is a point of separation for the primary vortex while at the same time it is a point of reattachment for BR_1. Along the boundary, theoretically only half-saddles (or half-nodes), and at the corners, quarter-saddles are possible as critical points in the flow field [36, 62, 97, 148].

A list of the critical points found by our computation for $Re = 1000$, both for the purely 2D flow computation and the flow in the plane of symmetry in the 3D computation are presented in table 3.1. As in figure 3.4, one can see from figure 3.5 that all the critical points present at the boundary walls are half-saddles. However, in 3D flows one can also observe the presence of half-nodes at the solid surfaces; apart from this one can see from figure 3.5 and table 3.1 that the center of the primary and secondary vortices as foci. Moreover, in a purely 2D flow computation or a flow which is two dimensional in nature like axi-symmetric flows, the structure of the vortices are such that the centers are encircled by close curves while in the 2D cross section of a 3D flow [36], trajectories spiral in or out towards or away from the limit cycles as would be seen in section 3.3.1.

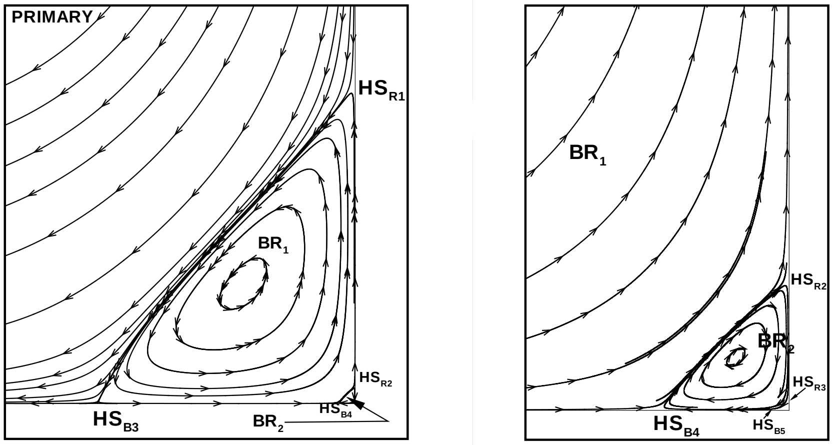

Figure 3.4: *Half-saddle point structures at the bottom right corner leading to separation and attachment in the 2D lid-driven cavity flow at* $Re = 1000$.

One can further notice that there are four half-saddle points HS_{L1}, HS_{B2}, HS_{B3}, HS_{R1} corresponding to the primary vortex, two each on the left and right wall and one center F_1. Then, at the left and right bottom corners, vortices are formed in succession each sharing two half-saddle points with the previous ones. For example, BL_1 and BR_1 each shares two half-saddle points with the primary vortex; half saddle points HS_{R2} and HS_{B4} are shared by both BR_1 and BR_2. Apart from these, for the 2D cavity, there exists four quarter-saddle (for schematic, see figure 3.2)(b) at each of its corners $(0, 0)$, $(1, 0)$, $(1, 1)$ and $(0, 1)$.

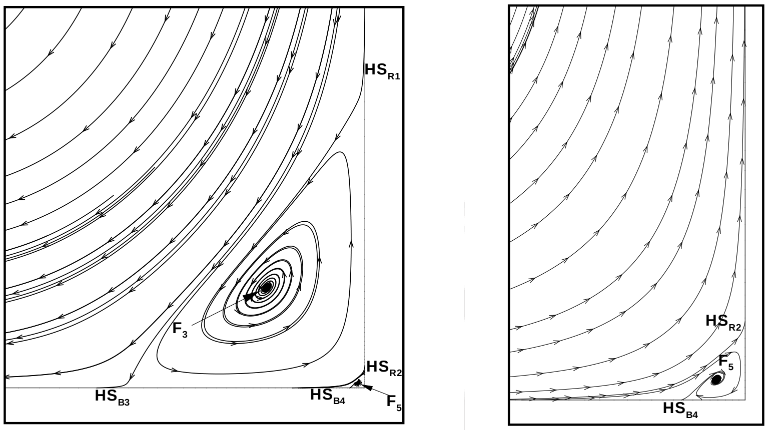

Figure 3.5: *Half-saddle point structures at the bottom right corner in the plane of symmetry of 3D lid-driven cavity flow at* $Re = 1000$.

Table 3.1: *Topology of critical points in lid-driven cavity for Re=1000*

	Spatial Location		
Critical Points	**2D Computation**	**3D Computation**	**Nature**
F_1	(0.5553, 0.6063)	(0.5029, 0.5379)	Center/Focus
F_2	(0.0502, 0.0459)	(0.0819, 0.0524)	Center/Focus
F_4	(0.0027, 0.0027)	(0.0015, 0.0058)	Center/Focus
F_6	(0.0001, 0.0001)	—	Center/Focus
F_3	(0.8842, 0.1230)	(0.8950, 0.1117)	Center/Focus
F_5	(0.9926, 0.0073)	(0.9924, 0.0054)	Center/Focus
F_7	(0.9995, 0.0004)	—	Center/Focus
HS_{L1}	(0, 0.1104)	(0, 0.1546)	Half-Saddle
HS_{L2}	(0, 0.0073)	(0, 0.0081)	Half-Saddle
HS_{L3}	(0, 0.0004)	—	Half-Saddle
HS_{B5}	(0.0004, 0)	—	Half-Saddle
HS_{B1}	(0.0073, 0)	(0.0099, 0)	Half-Saddle
HS_{B2}	(0.1308, 0)	(0.1952, 0)	Half-Saddle
HS_{B3}	(0.7358, 0)	(0.7392, 0)	Half-Saddle
HS_{B4}	(0.9826, 0)	(0.9850, 0)	Half-Saddle
HS_{B6}	(0.9989, 0)	—	Half-Saddle
HS_{R1}	(1, 0.3261)	(1, 0.3231)	Half-Saddle
HS_{R2}	(1, 0.0173)	(1, 0.0168)	Half-Saddle
HS_{R3}	(1, 0.0011)	—	Half-Saddle
QS_L	(0, 0)	(0, 0)	Quarter-Saddle
QS_R	(1, 0)	(1, 0)	Quarter-Saddle
QS_T	(0, 1)	(0, 1)	Quarter-Saddle
QS_B	(1, 1)	(1, 1)	Quarter-Saddle

3.3 Topological Implications

3.3.1 Limit cycles in the lid-driven cavity flow

Critical point theory [36] is an integral part of topological fluid dynamics, where the presence of limit cycles in the flow field represents one of the most

Indian Institute of Technology Guwahati

important non-linear phenomena. A *limit cycle* is an isolated closed trajectory. Isolated means that neighbouring trajectories are not closed; they spiral either toward or away from the limit cycle. If all the neighbouring trajectories approach the limit cycle, we say the limit cycle is stable (SLC). Otherwise, the limit cycle is unstable (ULC). In figure 3.6, we depict schematics of stable and unstable limit cycles.

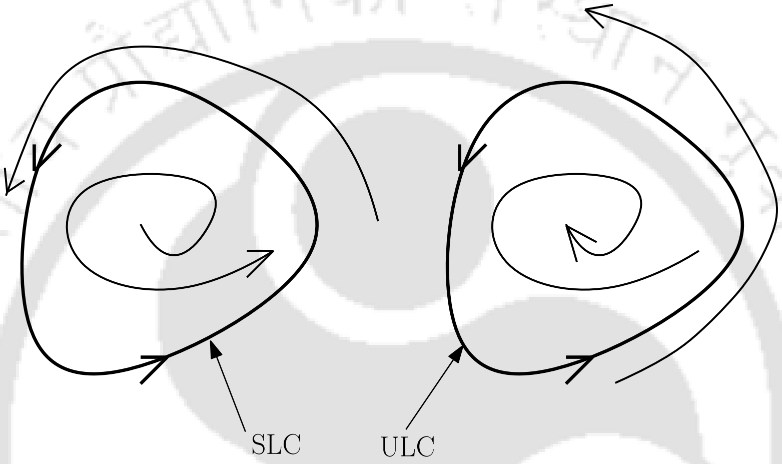

Figure 3.6: *Schematics of stable and unstable limit cycles.*

In 3D flows, the existence of limit cycles shaped by the streamlines can be found in the normal plane in the context of Frenet trihedron [25, 144] formed by the vectors $\hat{t}$, $\hat{n}$ and $\hat{b}$ as shown in figure 3.7, which is nothing but the plane spanned by the vectors $\hat{n}$ and $\hat{b}$. Note that $\hat{t}$ is the tangent vector to the vortical coreline at the point at which the Frenet trihedron is considered. Refer to the schematic of the normal plane in figure 3.7. The projection of the streamlines of the normal plane over the cross-flow plane are topologically equivalent, so it is enough to study the limit cycles projected on the cross-flow plane (see figure 3.1(b)).

We present the traces of the limit cycles (the dark solid closed curves in figure 3.8) in the plane of symmetry at the bottom right corners for the steady state flow in the 3D lid-driven cavity for $Re = 1000$. A close look at the neighbouring trajectories from the computed flow clearly reveals that irrespective of whether they lie inside or outside the dark solid closed curve, all of them spiral toward it and as such the limit cycles must be stable ones.

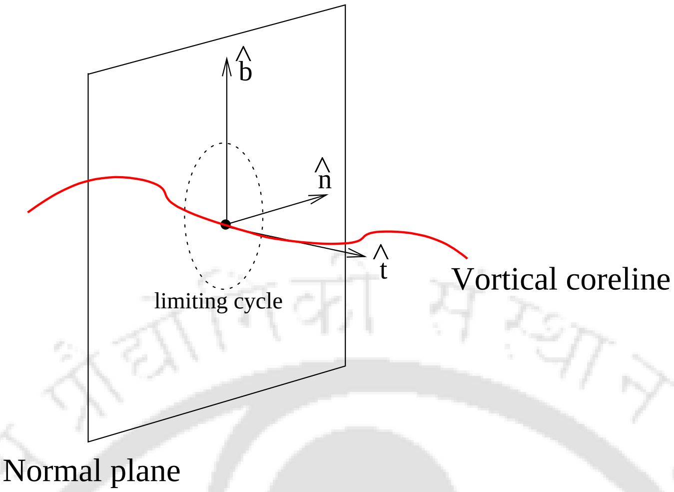

Figure 3.7: *Schematic of normal plane and limit cycles.*

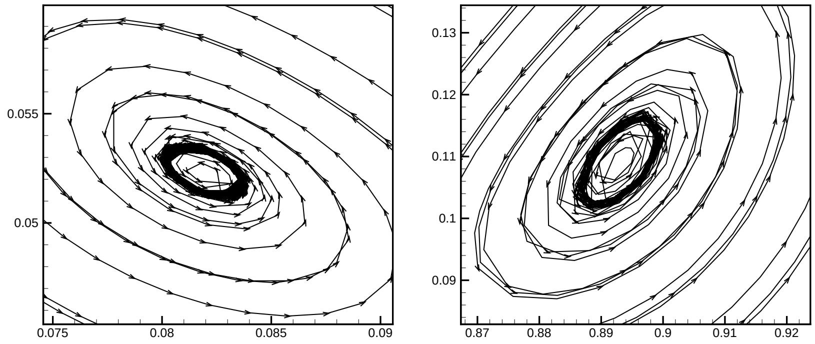

(a) (b)

Figure 3.8: *Close up view of the limit cycles (stable) in the 3D lid-driven cavity flow for Re* = 1000 *in the cross-flow plane: (a) Bottom left corner and (b) bottom right corner.*

In steady 3D flows, the limit cycles in the normal plane with the vortex centers at the foci are stable. For corner vortices, any two vortices in succession in the sequence, the trajectories originating in the foci have different orientations eventually approaching the limit cycles (figure 3.5). In purely 2D flow computations, these foci are *centers* (in dynamical sense) with the streamlines encircling the vortex centers. As such limit cycles cannot be present in purely 2D flow domain (See figure 3.3(a)). In a 3D flow field, vortices are indicated by the presence of limit cycles.

3.3.2 Critical points and the Poincaré-Bendixson formula

In the following, we use the Poincaré-Bendixson formula to ensure the number of critical points arising out of our computation are dynamically possible. The striking feature of the two figures 3.3, 3.4 and table 3.1 is that the critical points in the plane of symmetry of the cavity found out by us follow Poincaré-Bendixson topological formula [62, 148]:

On a two-dimensional plane cutting a three-dimensional body, if N, F, S, HN, HS, QS denote the node, focus, saddle, half-node, half-saddle and quarter-saddle (for schematic of these critical points, see figure 3.2(b)-(d)) respectively then following relation holds between them

$$\left[\sum(N+F)+\frac{1}{2}\sum HN\right]-\left[\sum S+\frac{1}{2}\sum HS+\frac{1}{4}\sum QS\right]=1-n$$

where n denotes the connectivity of the sectional flow defined by $n=1+p$, p being the surface complexity meaning the number of holes present in the flow domain.

In the plane of symmetry of the cavity, $p=0$, $\sum F=7$, $\sum N=0$, $\sum S=0$, $\sum HN=0$, $\sum HS=12$ and $\sum QS=4$. As such the critical points found out by us follow Poincaré-Bendixson formula.

Note that for the 2D lid-driven cavity flow with the top-lid moving from left to right, for moderately high Reynolds numbers, there appears a secondary vortex at the top left of the cavity. In general, if n_l, n_r, n_t represent the number of vortices at the left, right corners at the bottom and top-left respectively, then number of centers (or foci) present in the flow is $1+n_l+n_r+n_t$ (the additional one coming from the primary vortex). The number of half-saddles and quarter-saddles will be $2(n_l+n_r+n_t)$ and 4 respectively. As such the aforementioned topological formula holds here as well. In fact, if N is the total number of vortices in the lid-driven cavity including the primary vortex, then the number of centers (or foci) is N, number of half-saddles is $2(N-1)$ and quarter-saddles is 4. As such the Poincaré-Bendixson formula will always hold in the 2D lid-driven cavity flow. It is interesting to note that the critical points resulting from the 3D computation (see table 3.1) also satisfies the formula.

3.3.3 Topological evolution of corner vortices

Here, we present the details of the formation of corner vortices through a sequence of topological evolution of dynamical structures in the flow field. In figure 3.10, we depict different flow patterns leading to the onset of the very first vortex formation at the bottom left corner for $Re = 100$ in the plane of symmetry, viz., x-z plane at $y = 1.5$ of the 3D driven cavity of dimension $[0,1] \times [0,3] \times [0,1]$. These patterns are time dependent and they follow a typical sequence of topological changes giving birth to a corner vortex. The flow patterns evolve from a rotational saddle (the associated eigenvectors are non-orthogonal in the plane generated by these eigenvectors) to a non-canonical node and finally end up with a non-canonical focus. The evolution of these flow patterns are marked by (a) to (h) in figure 3.10.

In the process of evolution, at the very first stage, a half-saddle (HS) is formed on the left boundary at time $t = 0.0004$ (see figure 3.10(a)). The fluid in the neighbourhood of HS is pushed upwards giving rise to a saddle point at time $t = 0.00042$ near the corner and the saddle continues to exist until the saddle pattern of the critical point is broken. Such a situation is depicted in figure 3.10 (c) where one can see the trace of a node-saddle ($t = 0.00058$) structure. This structure has become more obvious in figure 3.10(d). At later stage of the evolution process, the saddle part completely disappears from this node-saddle structure (figure 3.10 (e)). At this stage, attachment and separation lines have now become clearly visible (depicted by arrows in the figure, on the line of separation (SL), the trajectories converges while on the attachment line (AL), they diverge, for details see ([36]) showing the indication for the formation a focus. At the stages 3.10(e)-(g), we observe degenerate patterns, viz., node-focus structure of the critical point in the flow field. Finally the advent of a non-canonical focus can be seen at the stage 3.10(h). This announces the birth of a vortex.

In their celebrated work, Perry and Chong [119] outlined the typical se-

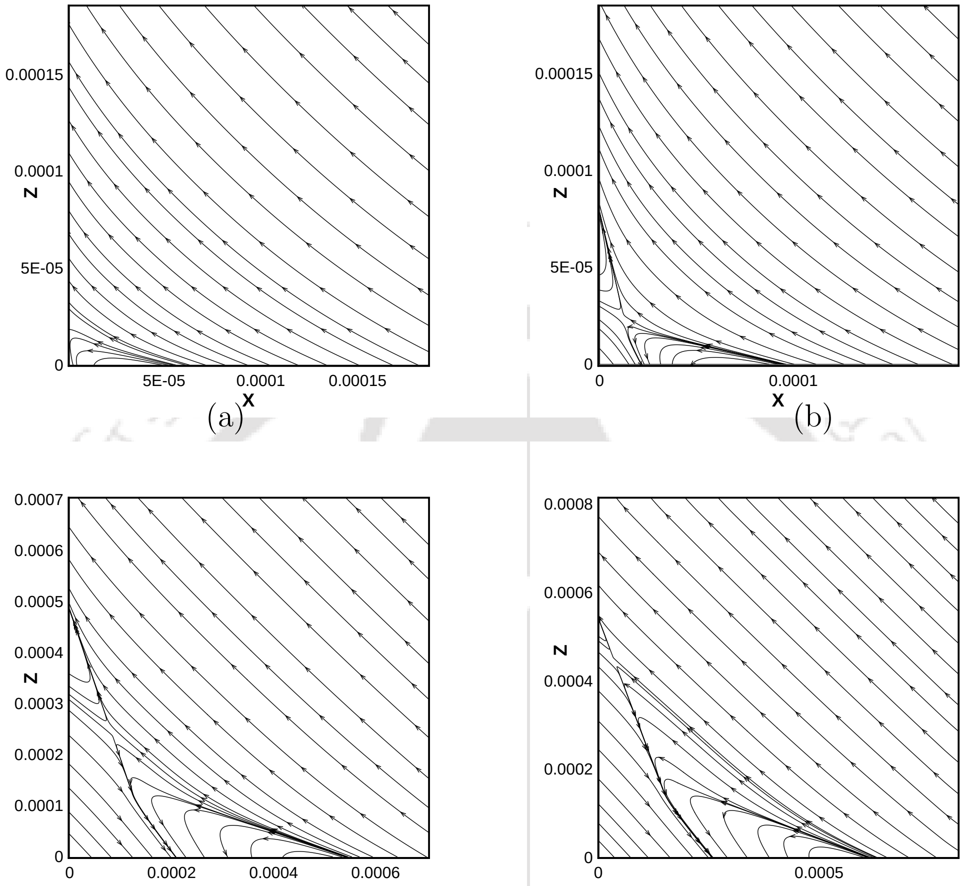

(a) (b)

(c) (d)

For the figure caption refer to the next page.

Institute of Technology Gu

quence of events in a vorticity region in a fluid domain leading to the formation of a vortex. They affirmed that whenever one can find a critical point in the flow field in the shape of a focus, there is a definite existence of a vortex. The description outlined in the above paragraph clearly corroborates the theory of Perry and Chong [119]. To the best of our knowledge, no study in the lid-driven cavity flow (both 2D and 3D) in the light of [119] has been carried out before.

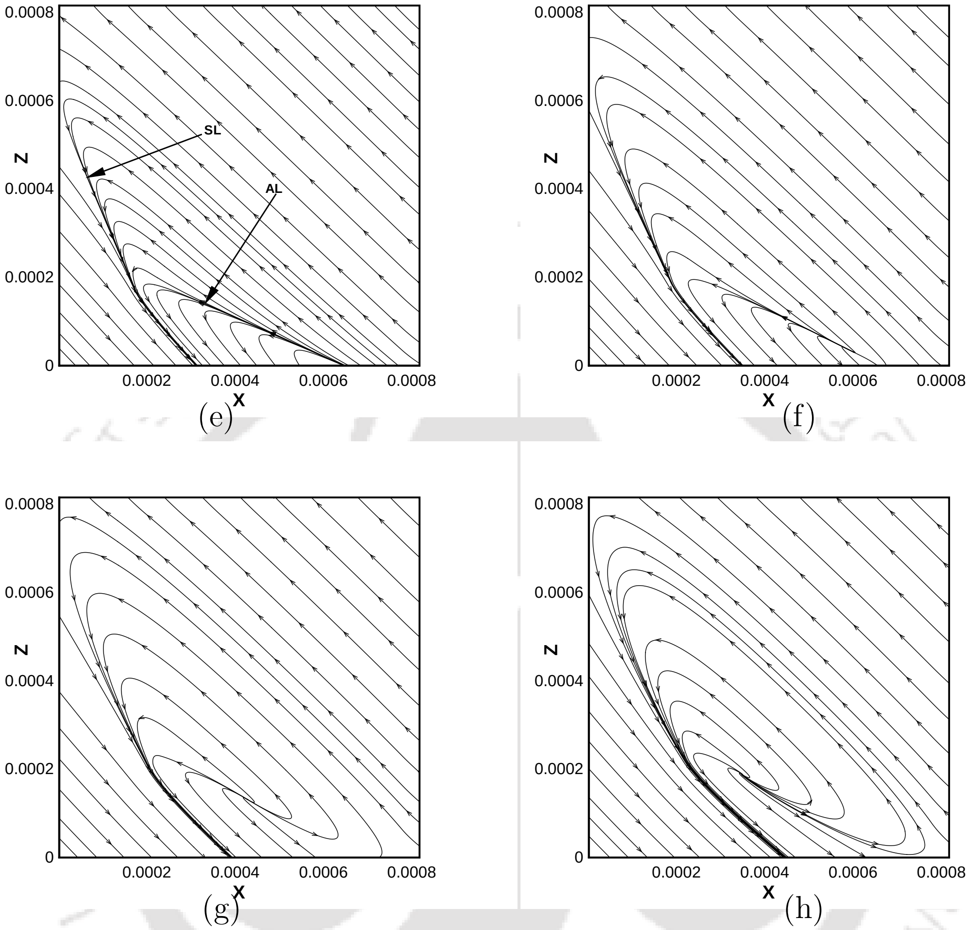

(e) (f) (g) (h)

Figure 3.10: *Topological evolution of corner vortices for* $Re = 100$ *of the 3D cavity at: (a)* $t = 0.0004$*, (b)* $t = 0.00042$*, (c)* $t = 0.00058$*, (d)* $t = 0.00062$*, (e)* $t = 0.00066$*, (f)* $t = 0.00068$*, (g)* $t = 0.0007$ *and (h)* $t = 0.00072$*.*

3.4 2D verses 3D separation

Note that in 2D lid-driven cavity flow corner vortices have been identified as the secondary, tertiary and quaternary vortices at the bottom corners of the cavity which are equivalent to the eddy shown in the bottom right at the plane of symmetry in figure 3.1(b). A close up view of this vortex and the secondary vortex at the bottom right corner from our 2D steady state computation for $Re = 1000$ is shown in figure 3.11. As one can see from 3.11(b), in 3D flows, velocity develops a transverse component allowing the flow to laterally escape.

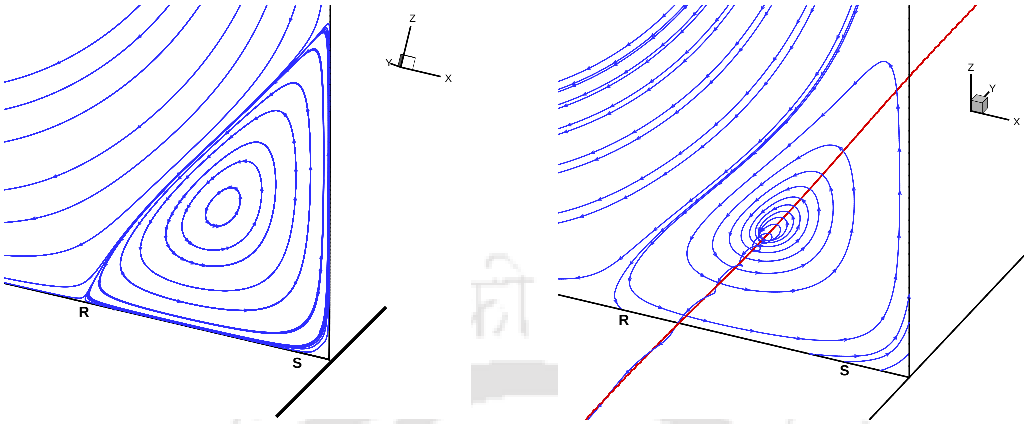

(a) (b)

Figure 3.11: *Flow separation: (a) two-dimensional (b) three-dimensional.*

The separated flow is not trapped in a closed recirculation bubble as in 2D flows (figure 3.11(a)), but can be evacuated along the transverse direction. Thus, in the context of critical point theory in dynamical system, the center of a vortex in 3D flow (unless it is a planar one) is a focus where the neighbouring trajectories spiral in or out of it, while in purely 2D planar flows it is a center; in this case the neighbouring trajectories are closed curves encircling the center. This is also obvious from figure 3.12, where streamtraces are plotted during the event of the first birth of of a corner vortex at the bottom left of the cavity for 2D (figure 3.12(a)) vis a vis 3D flow (figure 3.12(b)).

3.5 Conclusion

All the previous studies on the lid-driven cavity flow are confined to either the study of its 2D or 3D configuration in isolation. In the present study, we utilize the critical point concepts from the recent advances in the topological fluid dynamics theory to gain some physical insight into the corner vortices from the perspective of the flow topology in the 2D vis a vis 3D cavity. The separation, reattachment and vortical structures in the flow were analyzed by post-processing the computed flow through the identification of the critical points. The vortical structures found in the plane of symmetry of the 3D flow have been identified as stable limit cycles. Moreover, we utilize the Poincaré-

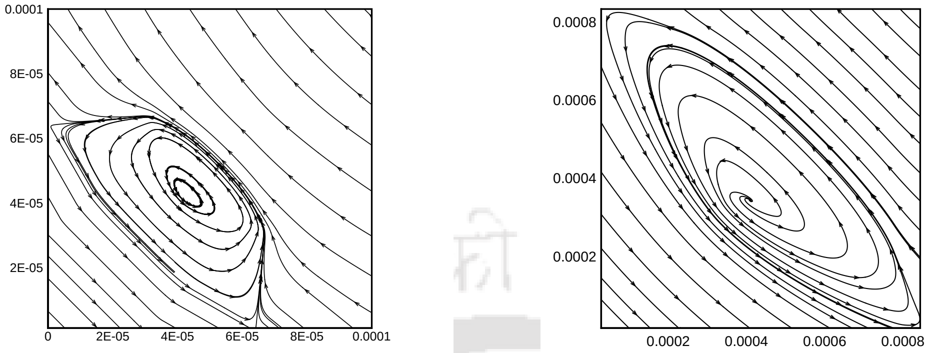

(a) (b)

Figure 3.12: *The birth of a corner vortex: (a) two-dimensional (b) three-dimensional.*

Bendixson formula to validate the computed flow in the two-dimensional cavity i.e, the possible number of critical points arising out of our computation follow the formula. The typical sequence of events in terms of the critical point structure leading to the very first birth of a vortex at the corner has been discussed in detail. The topological features of the corner vortices in actual 3D flow and its 2D idealization in the cavity has also been compared.

In the next chapter, we will discuss topological aspects of vortical structures in the 3D lid-driven rectangular cavities in detail. In particular, we consider the topological construction of TGL vortices and their relation with the "*U*-shaped and mushroom-shaped vortex" structures found in the region where transition to turbulence takes place.

भारतीय प्रौद्योगिकी संस्थान गुवाहाटी • Indian Institute of Technology Guwahati •

Chapter 4

TOPOLOGICAL ASPECTS OF VORTICAL STRUCTURES IN THE 3D LID-DRIVEN CAVITY FLOW

4.1 Introduction

The past few decades have seen viscous-vortex flows in a bounded domain as an important area of research among the fluid mechanics community. The flow in the lid-driven cavity (LDC) belongs to this class of flows. This problem has received considerable interest among the scientific community not only because of its geometric simplicity but also its direct relevance to many practical applications ranging from purely engineering [3, 20, 47] to medical sciences [13, 126]. Due to its geometric simplicity, conduct of experimental observations and numerical predictions of this flow are less cumbersome than other benchmark problems like the flow past a circular cylinder [18, 32, 33, 80, 143, 149, 150].

The experimental investigation of the LDC problem dates back to the work of Pan and Acrivos [114] who studied the steady flows in a rectangular cavity where the motion is driven by the uniform translation of the top wall.

Following this, a series of extensive experimental studies were conducted by Koseff and Street [83, 84, 85] in 1980's, who presented a synthesis of observations through the use of visualization pictures, and velocity and heat-flux measurements. Though the work of Pan and Acrivos [114] also contained some numerical solutions, purely numerical studies of this problem dates back to the pioneering work of Burggraf [24] in their two-dimensional (2D) analysis. The three-dimensional (3D) studies of lid-driven cavity was first considered by Davis and Mallinson [34]. Later, a host of numerical studies were performed by many researchers [31, 44, 45, 88], the most cited amongst them being the 2D work of Ghia *et al.* [48]. An excellent review of this topic could be found in the work of Shankar and Deshpande [130].

As could be seen from the previous chapter, highly complex flow patterns are observed inside the cavity despite its simple geometric configuration. These complex flow patterns are mainly characterized by the presence of vortical structures such as downstream secondary eddy (DSE), upstream secondary eddy (USE), primary eddy (PE), Taylor-Görtler-like (TGL) eddies and end wall corner eddies. The significance and role of these eddies in the flow have already been discussed by Chiang *et. al* [27, 28, 29, 131]. Although Sheu and Tsai initiated the study of flow topology for the steady 3D LDC in 2002 [131], a careful undermining into the existing literature reveals that there still are many topological aspects of vortical structures remained unexplored. Moreover, in [27, 28, 29, 131] the classification of critical points and the interpretation of Poincaré-Bendixson formula were seen to be ambiguous. In the current study, we endeavour to explain the the issues related to the classification and nature of the critical points, and then the Poincaré-Bendixson formula. Moreover, no detailed topological studies are available in the existing literature for higher Reynolds numbers (*Re*). As such, we provide an account of the flow topology in the cavity for $Re = 3200$, in particular, the topology of the TGL vortices.

The TGL vortices were experimentally observed in Standford Laboratory by Koseff and Street [83, 84, 85]. They reported the finding of eight pairs of TGL vortices for $Re \sim 3000$. For moderate Re s upto 6000, another three pairs of TGL vortices become visible [29, 38, 44, 131], while for $Re > 6000$ the flow was seen to make a transition towards turbulence. These vortices were first numerically confirmed by Freitas et al. [45] in 1985. Of late, there has been a surge of experimental and numerical studies on TGL vortices in 3D LDC [45, 51, 66, 88, 90, 103, 116]. In 1992, the GAMM-committee funded a workshop on numerical simulation of a lid-driven cavity flow at Re=3200 for SAR=3:1 [38]. The main aim of this workshop was to affirm the number of TGL vortex pairs in the transverse direction. Comparisons were made among the findings of contributors and surprisingly the conclusions from their simulations were seen to be quite different. The disagreement was not only on the issue of flow symmetry but also on the number of TGL vortex pairs.

A close look into the existing literature reveals mere mention of the existence of TGL vortices at moderate Reynolds numbers by numerous researchers in the 3D LDC without providing much insight into their topological construction. In the current study, we attempt to explore the dynamics of TGL vortices by a rigorous topological theory [9, 36, 62, 97, 142, 148] in the 3D LDC flow. The "U-shaped and mushroom-shaped vortex" structures have also been observed in the flow field through the visualization of λ_2 isosurfaces [67]. These structures are closely related to transition to turbulence and henceforth with TGL vortices.

4.2 Problem description and numerical methodology

The transient 3D incompressible Navier–Stokes (N–S) equations in the traditional primitive variable formulation in dimensionless form can be written as

$$\frac{\partial u}{\partial x}+\frac{\partial v}{\partial y}+\frac{\partial w}{\partial z}=0, \tag{4.1}$$

$$\frac{\partial u}{\partial t}+u\frac{\partial u}{\partial x}+v\frac{\partial u}{\partial y}+w\frac{\partial u}{\partial z}=-\frac{\partial p}{\partial x}+\frac{1}{Re}\nabla^2 u, \tag{4.2}$$

$$\frac{\partial v}{\partial t}+u\frac{\partial v}{\partial x}+v\frac{\partial v}{\partial y}+w\frac{\partial v}{\partial z}=-\frac{\partial p}{\partial y}+\frac{1}{Re}\nabla^2 v, \tag{4.3}$$

$$\frac{\partial w}{\partial t}+u\frac{\partial w}{\partial x}+v\frac{\partial w}{\partial y}+w\frac{\partial w}{\partial z}=-\frac{\partial p}{\partial z}+\frac{1}{Re}\nabla^2 w. \tag{4.4}$$

Here, we u, v, w are the velocity components along x-,y- and z- directions respectively, t is the time and p is the pressure. In the above equations, $Re = (U_0 B/\nu)$ is the Reynolds number, where ν stands for the kinematic viscosity, B is the width of the cavity, U_0 is the velocity at the roof of the cavity and $\nabla^2 \equiv \frac{\partial^2}{\partial x^2} + \frac{\partial^2}{\partial y^2} + \frac{\partial^2}{\partial z^2}$.

Computational modeling of the flow in the rectangular cavity requires numerically solving the above mentioned 3D N–S equations. Configuration of a 3D rectangular cavity with span-wise aspect ratio two has already been depicted in figure 3.2(a). A schematic of such flow in an experimental set up by Koseff and Street [83, 84, 85] is shown in Figure 4.1.

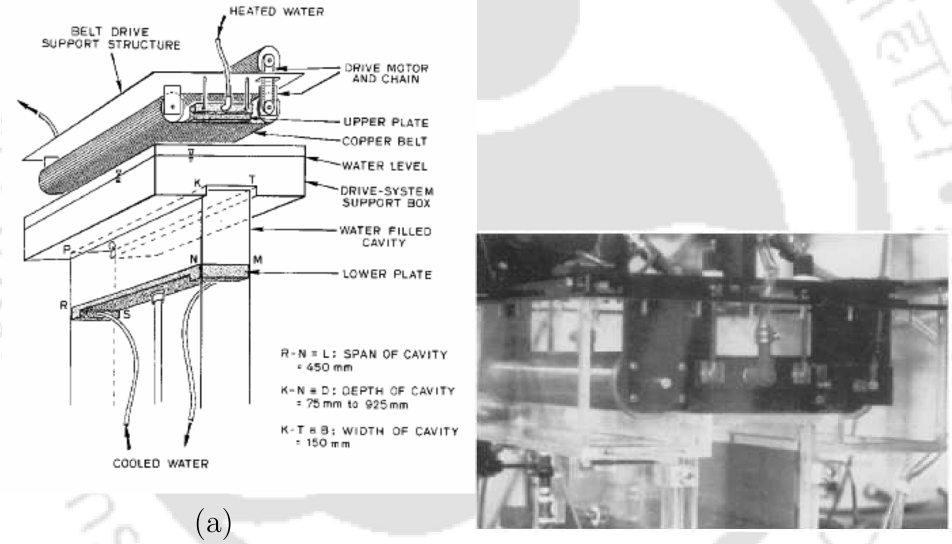

(a) (b)

Figure 4.1: *Experiment of Koseff and Street: (a) Schematic of the set up and (b) actual experimental set up [83, 84, 85].*

We employed the commercially available software package ANSYS Fluent (version 15.0) to solve the 3D N–S equations. This well established code has found its application in the computation of this complex flow phenomena, as can be found in references [42, 64, 139]. We utilized the segregated solver in which second-order upwind scheme has been used to descretize the momentum equations; for the pressure-velocity coupling the well-known SIMPLE algorithm [117] has been used. For computing the flow on non-uniform grid of sizes $101 \times 201 \times 101$ and $101 \times 301 \times 101$ with time steps varying from $\Delta t = 10^{-2}$ to 10^{-4}, double precision arithmetic was used. The iteration

Institute of Technology

procedure was terminated whenever the scaled residuals for the solutions for the velocity components and continuity equation approached a tolerance limit 10^{-6}. In cases where steady state is achievable, a time marching strategy is adopted till a steady-state is reached.

Our main aim of the present study is to explore different topological aspects of vortical structures in the driven cavity. In order to capture the vortical structures accurately, extreme clustering has been employed in the neighbourhood of the solid boundaries. The significance of the clustering parameter λ has already been explained in chapter 2. In figures 4.2(a)-(d), we depict clustered grids in the neighbourhood of the solid walls of the whole rectangular cavity; and also in different 2D planes cutting the 3D cavity.

4.3 Preliminaries

In this section, we briefly discuss different aspects of existing topological theory [9, 36, 62, 97, 142, 148] which will be widely used in the present study.

4.3.1 The concept of limiting streamlines/skin friction lines

Let us consider a body delimited by a surface S and an orthonormal local system $(\vec{i},\ \vec{j},\ \hat{n})$ defined by the unit vector $\hat{n}$ normal to the surface and two unit vectors $\vec{i}$, $\vec{j}$ lie on the plane tangent to S at the point of contact. The corresponding coordinates associated with local orthonormal system are x, y and z.

The fluid flow past a surface S exerts a force $\vec{F}$ on a surface element dS given by $\vec{F} = \vec{P}dS$, where $\vec{P}$ is the force per unit area decomposed in the form $\vec{P} = -p\hat{n} + \vec{\tau}$. The term $-p\hat{n}$ is the normal action of pressure and $\vec{\tau}$ is the shear stress. The shear stress $\vec{\tau}$ can be written in the form: $\vec{\tau} = \tau_x\vec{i} + \tau_y\vec{j}$. Thus in a 3D flow, the wall shear stress is a vector whereas in 2D flow, it is considered to be a scalar quantity. The shear stress exerted on the surface S of the body constitutes a vector field. The problem is to find the lines of force or trajectories of this vector field. The concept of limiting streamline

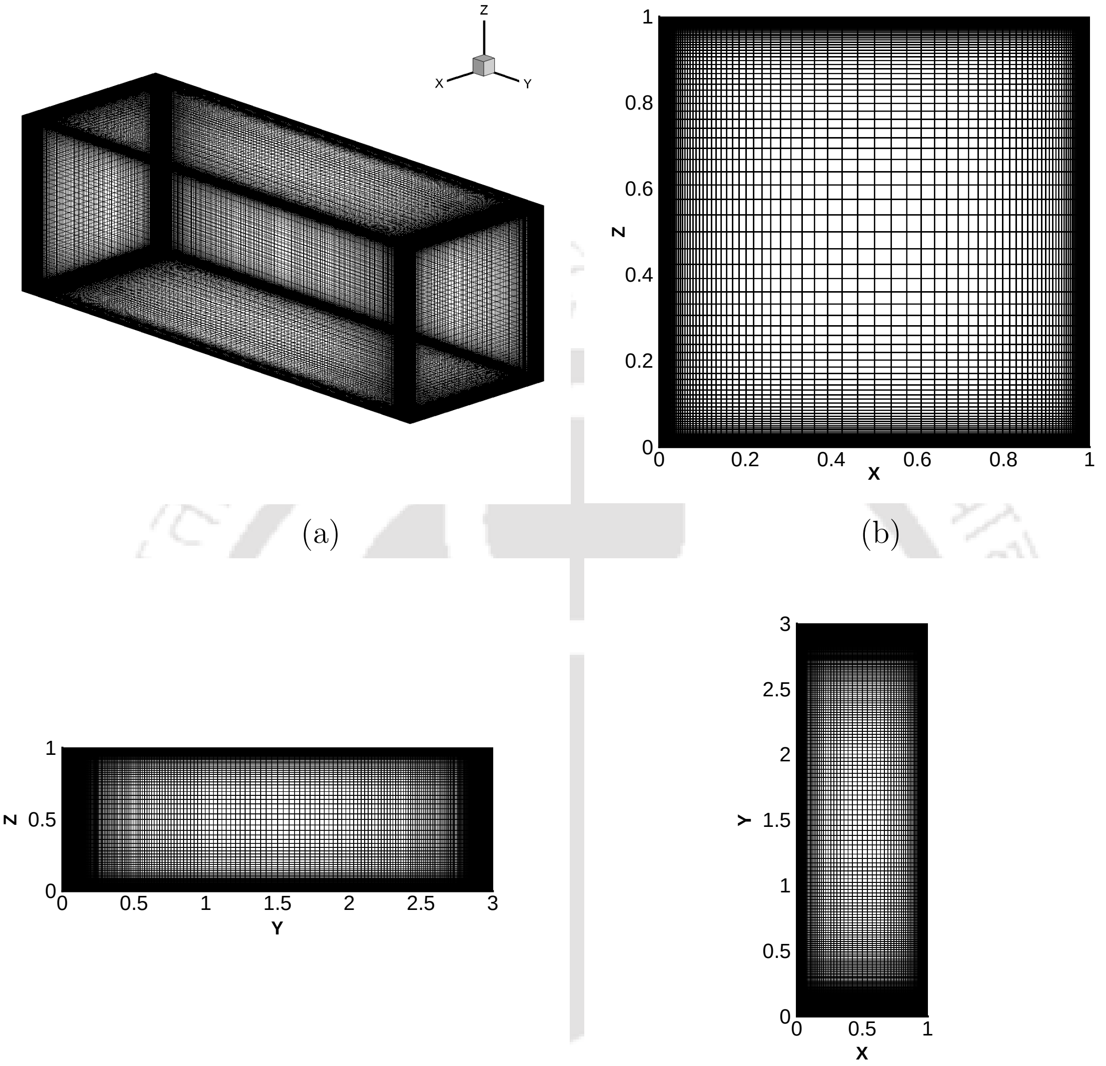

(a) (b)

(c) (d)

Figure 4.2: *Typical clustered grids : (a) in the cavity* $101 \times 301 \times 101$, $\lambda = 0.85$, *(b)* 101×101 *(*x*-*z *plane)*, $\lambda = 0.85$, *(c)* 301×101 *(*y*-*z *plane)*, $\lambda = 0.85$ *and (d)* 101×301 *(*x*-*y *plane)*, $\lambda = 0.85$.

was introduced by W. R. Sears [127] and is defined by the limiting position of a streamline when its distance to the surface tends to zero. The equation of a streamline in the 2D x-y plane is given by

$$\frac{dy}{dx} = \frac{v}{u}.$$

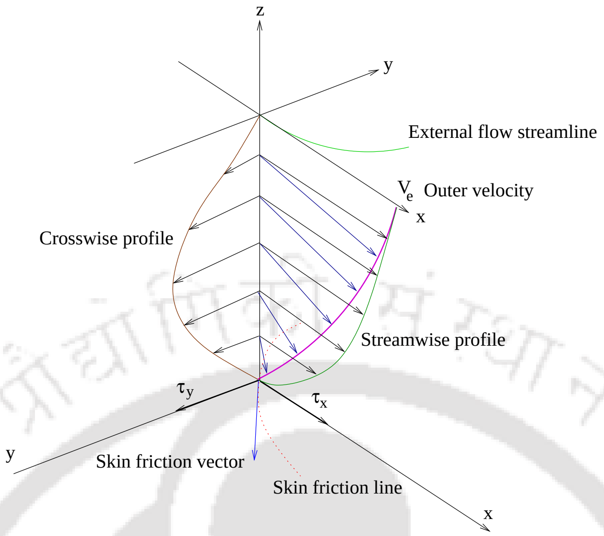

Figure 4.3: *Structure of a 3D boundary layer.*

By using L'Hospital's rule [123] and taking into account the effect of viscosity at the wall in the above equation we obtain

$$\frac{dy}{dx} = \frac{v}{u}\bigg|_{\lim_{z\to 0}} = \frac{\frac{\partial v}{\partial z}}{\frac{\partial u}{\partial z}}\bigg|_{\lim_{z\to 0}} = \frac{\tau_y}{\tau_x}$$

Therefore the lines of force or the trajectories of vector field generated by shear stress are defined as the solutions of the differential system (in xy-coordinate plane).

$$\frac{dx}{\tau_x(x,y)} = \frac{dy}{\tau_y(x,y)} = dt \tag{4.5}$$

Analogous to the streamlines, where the velocity vectors are tangent at each point, a skin friction line or curve is one where at each point, the skin friction vector is a tangent to it (refer to figure 4.3). In the current study, we will use the physical concept of skin friction lines rather than the limiting streamlines as in reality there is no flow in the surface.

4.3.2 Critical points of the skin friction line patterns

As described in the above section, the skin friction lines on a body are solutions of the system (4.5) and in general, one and only one trajectory known as skin friction line passes through a point on the surface. However, this is not true for a point P_0, where the skin friction vector vanishes. In such cases, the system (4.5) is singular. A point which do not satisfy the general rule for the tracing of the skin friction lines is called a singular or critical point at which (at the point P_0) $\tau_x(x,y) = 0$ and $\tau_y(x,y) = 0$ simultaneously. As such the solution of (4.5) leads to an eigenvalue problem. In order to study, the behaviour of skin friction lines near a critical point P_0 we make a first-order Taylor series expansion in the neighbourhood (vicinity) of P_0 as

$$\tau_x(x,y) = \left(\frac{\partial \tau_x}{\partial x}\right)_{P_0}(x - x_0) + \left(\frac{\partial \tau_x}{\partial y}\right)_{P_0}(y - y_0)$$

$$\tau_y(x,y) = \left(\frac{\partial \tau_y}{\partial x}\right)_{P_0}(x - x_0) + \left(\frac{\partial \tau_y}{\partial y}\right)_{P_0}(y - y_0)$$

Without loss of generality, one can assume the origin to be at P_0 and consequently equation (4.5) reduces to

$$\frac{dx}{\frac{\partial \tau_x}{\partial x}x + \frac{\partial \tau_x}{\partial y}y} = \frac{dy}{\frac{\partial \tau_y}{\partial x}x + \frac{\partial \tau_y}{\partial y}y}$$

Assuming skin friction derivatives to be different from zero, one gets

$$\frac{dx}{\frac{\partial \tau_x}{\partial x}x + \frac{\partial \tau_x}{\partial y}y} = \frac{dy}{\frac{\partial \tau_y}{\partial x}x + \frac{\partial \tau_y}{\partial y}y} = \frac{\lambda dx + \mu dy}{\lambda\left(\frac{\partial \tau_x}{\partial x}x + \frac{\partial \tau_x}{\partial y}y\right) + \mu\left(\frac{\partial \tau_y}{\partial x}x + \frac{\partial \tau_y}{\partial y}y\right)} \tag{4.6}$$

A solution for (4.5) is sought by writing (4.6) in the form

$$\frac{\lambda dx + \mu dy}{\lambda\left(\frac{\partial \tau_x}{\partial x}x + \frac{\partial \tau_x}{\partial y}y\right) + \mu\left(\frac{\partial \tau_y}{\partial x}x + \frac{\partial \tau_y}{\partial y}y\right)} = \frac{d(\lambda x + \mu y)}{C(\lambda x + \mu y)}.$$

where C is a constant. If this form is possible, then letting $\dfrac{d(\lambda x+\mu y)}{C(\lambda x+\mu y)}=-dt$, we have $\lambda x+\mu y=Ae^{-Ct}$, where t is the integration variable and A is constant; it is assumed that the trajectories are represented by the parametric equations $x=x(t)$, $y=y(t)$ with $-\infty<t<\infty$. The above form is possible if the following conditions are satisfied:

$$\lambda\frac{\partial\tau_x}{\partial x}x+\mu\frac{\partial\tau_y}{\partial x}x=C\lambda x \quad \text{and} \quad \lambda\frac{\partial\tau_x}{\partial y}y+\mu\frac{\partial\tau_y}{\partial y}y=C\mu y$$

Solving for non-trivial solution of λ and μ results in the following condition

$$\begin{vmatrix} \frac{\partial\tau_x}{\partial x}-C & \frac{\partial\tau_y}{\partial x} \\ \frac{\partial\tau_x}{\partial y} & \frac{\partial\tau_y}{\partial y}-C \end{vmatrix}=0$$

Thus, finding the values of the constant C is equivalent to finding the eigenvalues of the Jacobian matrix

$$J=\begin{pmatrix} \frac{\partial\tau_x}{\partial x} & \frac{\partial\tau_y}{\partial x} \\ \frac{\partial\tau_x}{\partial y} & \frac{\partial\tau_y}{\partial y} \end{pmatrix}$$

which are given by $C_{1,2}=\dfrac{-p\pm\sqrt{p^2-4q}}{2}$ where $p=-\text{trace}(J)$ and $q=\text{determinant}(J)$. The dynamical structures of the critical points depend on the nature (real or complex) and the sign of the eigenvalues which can be seen in figure 4.4.

The preceding considerations applied to any vector field can be extended to 3D flow as well. For a steady regime (though not essential), the streamlines are defined by

$$\frac{dx}{u(x,y,z)}=\frac{dy}{v(x,y,z)}=\frac{dz}{w(x,y,z)}$$

where $\vec{V}=u\hat{i}+v\hat{j}+w\hat{k}$ is the velocity vector. We examine their behaviour in the vicinity of a critical point, where $u=v=w=0$. As in the planar case, by expanding the velocities in the vicinity of the critical points by a first-order Taylor series expansion, the above equation is integrated in such a way that a

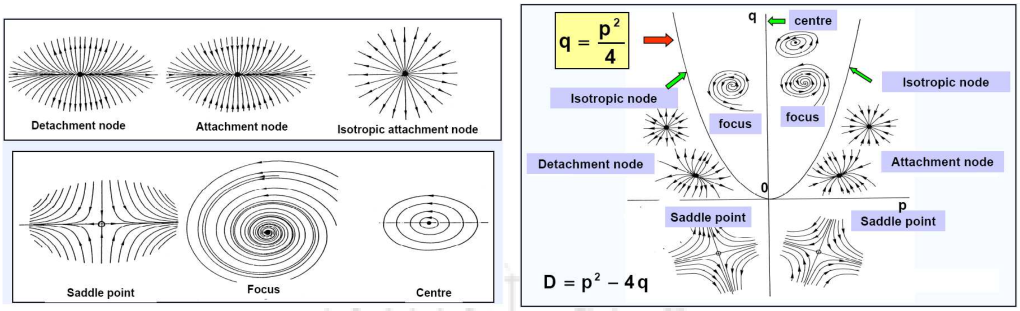

(a) (b)

Figure 4.4: *Classification of critical points: (a) Overall and (b) in the p-q plane (Courtesy [36]).*

logarithmic solution is obtained from the equation

$$\frac{d(\lambda x + \mu y + \nu z)}{C(\lambda x + \mu y + \nu z)} = -dt.$$

This will result in a third order matrix having three eigenvalues C_1, C_2 and C_3.

(a) If the roots C_1, C_2 and C_3 are real and of the same sign, the critical point is a node.

(b) If C_1, C_2 and C_3 are real with different signs, the critical point is a saddle point.

(c) If C_1 is real and C_2 and C_3 are complex conjugates, the critical point is a focus.

Apart from the above classification, the other critical points in 3D flows are half-node, half-saddle present on the surface walls and quarter-saddle at the corners [36, 62, 65, 148]. In particular, these points can be found on the boundaries cut out from a 3D domain. A point is called half-saddle/half-node if there are three trajectories/integral curves connecting the point on the boundary of the flow domain. In case of half-saddle, out of three trajectories one differs in direction from other two. However, direction of all three trajectories is same for a half-node. A quarter-saddle is defined to be a point connecting two trajectories having opposite direction. The following figure (figure 4.5) depicts schematic of half-node, half-saddle and quarter-saddle in different situations.

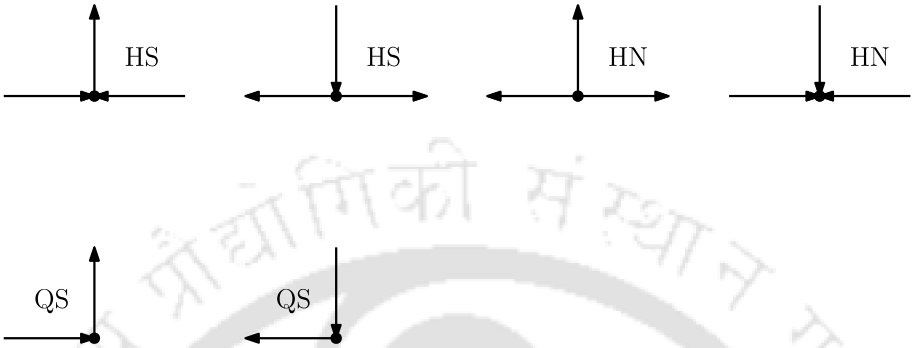

Figure 4.5: *Schematic of half-saddle, half-node and quarter-saddle.*

4.3.3 Mathematical criteria of separation and attachment

In their work, Surana *et al.* [136] established some mathematical criteria to determine the presence of separation and attachment lines in the flow field. Here we briefly state these criteria [137].

I. A point $\vec{p}$ on the boundary wall $z = 0$ is said be a separation point if, and only if, $\vec{\tau}(\vec{p}) = 0,\ \vec{\nabla}_x \cdot \vec{\tau}(\vec{p}) < 0,\ \det \vec{\nabla}_x \vec{\tau}(\vec{p}) > 0$, that is, $\vec{p}$ is either a stable node or a stable spiral of the wall-shear field.

II. A point $\vec{p}$ on the boundary wall $z = 0$ is said be a attachment point if, and only if, $\vec{\tau}(\vec{p}) = 0,\ \vec{\nabla}_x \cdot \vec{\tau}(\vec{p}) > 0,\ \det \vec{\nabla}_x \vec{\tau}(\vec{p}) > 0$, that is, $\vec{p}$ is either a unstable node or a unstable spiral of the wall-shear field.

As mentioned in [136], there are infinitely many wall-shear streamlines on the boundary $z = 0$. Therefore, in order to identify separation and attachment lines, additional criteria are required. The following criterion are the necessary and sufficient conditions for the existence of these lines.

I. *Separation line criterion:*

A bounded trajectory γ of the wall-shear field is a separation line if, and only if, one of the following conditions holds:

1. γ originates from a saddle $\vec{p}$ with $\vec{\nabla}_x \cdot \vec{\tau}(\vec{p}) < 0$ and ends at a stable spiral $\vec{q}$ with $\vec{\nabla}_x \cdot \vec{\tau}(\vec{q}) < 0$.
2. γ originates from a saddle $\vec{p}$ with $\vec{\nabla}_x \cdot \vec{\tau}(\vec{p}) < 0$ and ends at a stable node $\vec{q}$ with $\vec{\nabla}_x \cdot \vec{\tau}(\vec{q}) < 0$.
3. γ originates from a saddle $\vec{p}$ with $\vec{\nabla}_x \cdot \vec{\tau}(\vec{p}) < 0$ and spirals onto a stable limit cycle Γ with

$$\int_\Gamma \vec{\nabla}_x \cdot \vec{\tau}[\vec{x}(s;\vec{x}_0)]\mathrm{d}s < 0.$$

4. γ is a stable limit cycle with

$$\int_\Gamma \vec{\nabla}_x \cdot \vec{\tau}[\vec{x}(s;\vec{x}_0)]\mathrm{d}s < 0,$$

where $\vec{x}(s;\vec{x}_0)$ denotes a trajectory of the wall-shear field $\vec{\tau}(\vec{x})$ with $\vec{x}(s,\vec{x}_0) = \vec{x}_0$.

II. *Attachment line criterion:*

A bounded trajectory γ of the wall-shear field is an attachment line if, and only if, one of the following conditions holds:

1. γ originates from an unstable spiral $\vec{p}$ with $\vec{\nabla}_x \cdot \vec{\tau}(\vec{p}) > 0$ and ends at a saddle $\vec{q}$ with $\vec{\nabla}_x \cdot \vec{\tau}(\vec{q}) > 0$.
2. γ originates from an unstable node $\vec{p}$ with $\vec{\nabla}_x \cdot \vec{\tau}(\vec{p}) > 0$ and ends at a saddle $\vec{q}$ with $\vec{\nabla}_x \cdot \vec{\tau}(\vec{q}) > 0$.
3. γ spirals off from an unstable limit cycle Γ with

$$\int_\Gamma \vec{\nabla}_x \cdot \vec{\tau}[\vec{x}(s;\vec{x}_0)]\mathrm{d}s > 0$$

and ends at a saddle $\vec{q}$ with $\vec{\nabla}_x \cdot \vec{\tau}(\vec{q}) > 0$.

4. γ is an unstable limit cycle with

$$\int_\Gamma \vec{\nabla}_x \cdot \vec{\tau}[\vec{x}(s;\vec{x}_0)]\mathrm{d}s > 0.$$

All the critical points i.e, saddles, spirals, nodes and limit cycles highlighted in the separation and attachment criteria must be non-degenerate. The conditions for these critical points to be non-degenerate and details of the separation and attachment lines criteria at corner can be found in [136, 137].

4.3.4 Topological rules

The following topological rules [36, 62, 65, 148] have been used to validate the computed solutions for the possible number of critical points present in the flow field. These rules ensure that all the critical points obtained through above mentioned eigenvalue analysis [36] are kinematically (dynamically) possible.

Theorem 4.3.1. *(Poincaré-Bendixson formula: version-1) On a three-dimensional body surface, if N, F and S denote the node, focus and saddle point respectively then the following relation holds*

$$\sum (N+F) - \sum S = 2 - 2p$$

where p denotes the complexity of the flow surface.

The version 2 of Poincaré-Bendixson theorem is nothing but the one described in section 3.3.2, which is as follows.

Theorem 4.3.2. *(Poincaré-Bendixson formula: version-2) On a two-dimensional plane cutting a three-dimensional body, if N, F, S, HN, HS, QS denote the node, focus, saddle, half-node, half-saddle and quarter-saddle respectively then following relation holds between them*

$$\left[\sum (N+F) + \frac{1}{2}\sum HN\right] - \left[\sum S + \frac{1}{2}\sum HS + \frac{1}{4}\sum QS\right] = 1 - n$$

where n denotes the connectivity of the sectional flow defined by $n = 1 + p$, p being the surface complexity meaning the number of holes present in the flow domain.

The above theorems enable us to validate the number of critical points in the flow field in different fluid flow situations.

4.3.5 Vortex identification: λ_2 criterion

In the following, we briefly discuss a robust criterion known as λ_2 criterion for the vortex identification developed by Jeong and Hussain [67]. This criterion has been extensively used in the present study to visualize vortical phenomena in the driven cavity.

The λ_2 criterion has been formulated by keeping in mind that the local minimum pressure or maximum vorticity in a two-dimensional plane fails to identify vortices due to the high viscous and unsteady effects. By neglecting these effects one may obtain the symmetric part of the gradient of the N–S equations in the following form

$$S_{ik}S_{kj} + \Omega_{ik}\Omega_{kj} = -\frac{1}{\rho}p_{,ij},$$

where

$$S_{ij} = \frac{1}{2}\left(\frac{\partial u_i}{\partial x_j} + \frac{\partial u_j}{\partial x_i}\right) \text{ and } \Omega_{ij} = \frac{1}{2}\left(\frac{\partial u_i}{\partial x_j} - \frac{\partial u_j}{\partial x_i}\right)$$

represent the symmetric (rate-of-strain tensor) and anti-symmetric (vorticity tensor) components of the velocity gradient tensor ∇u respectively; $p_{,ij} = \dfrac{\partial^2 p}{\partial x_i \partial x_j}$ denote the Hessian of the pressure. In order to capture the region where instantaneous pressure is minimum, Jeong and Hussain [67] define the vortex core as a connected region with two negative eigenvalues of the symmetric 3×3 tensor $A_{ij} = \sum_{k=1}^{3} \Omega_{ik}\Omega_{kj} + S_{ik}S_{kj}$. Given the three eigenvalues of A_{ij} at each grid point, a vortex core is identified as any neighbouring region having two negative eigenvalues. If λ_1, λ_2 and λ_3 are eigenvalues of A_{ij} and sorted them as $\lambda_1 \geq \lambda_2 \geq \lambda_3$, then the region correspond to a vortex core in which $\lambda_2 < 0$. The main advantage of this criterion is that vortices can be identified as isosurfaces. Moreover, this criterion is scale invariant (Galilean-invariant) which means it produces the same result; so there is no ambiguity in selecting which isosurface value to render. Further details of this criterion can be found in [26, 60, 67, 94].

4.4 Results and discussions

In the following, we provide flow topology in the 3D LDC for $Re = 1000$ and 3200. Vortical phenomena and surface flow topology are our key interest as important events like separation, attachment etc. take place in the vicinity of solid walls/surfaces due to large viscous effects. In order to observe the surface flow patterns, we compute the flow in a parallel setup by solving the 3D N–S equations on a Intel Xeon 8 Core E5-2650 based PC with 64GB DDR3 ECC RAM by using 12 processors. We identify different critical points by post-processing the computed data.

4.4.1 Flow topology for $Re = 1000$

In this section, we present different kinematically possible flow structures in the neighbourhood of critical points identified by us from the parallel computation on grid of size $101 \times 201 \times 101$. All these structures are associated with the different fluid mechanical phenomena such as separation, attachment, spiralling motion in the driven cavity. In the following, we discuss all these aspects in detail.

4.4.1.1 Critical points and dynamical structures in the flow field

In order to visualize the surface flow topology, we plot skin friction line patterns on the five stationary walls of the cavity. Through streamtraces we observe different topological structures in the neighbourhood of critical points such as separation and attachment lines. The separation lines are those in which all the neighbouring trajectories converge towards these lines; on the other hand for the line of attachment, the trajectories adjacent to it repelled from these lines [36]. In figure 4.6, we depict a 3D view of skin friction line patterns on five solid surfaces in which various topological structure such as separation and attachment lines and stream surfaces of separation and attachment have been observed. These skin friction line patterns are characterized by different form of critical points in the flow field. The critical points such as node, focus and saddle points are present (see figure 4.4) in the interior of flow domain.

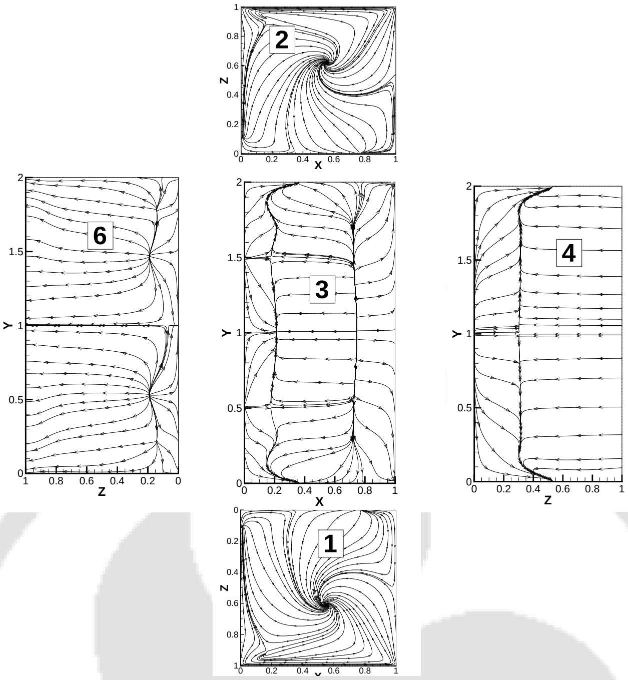

Figure 4.6: *Streamtraces indicating the critical points on five stationary walls of the cavity for* $Re = 1000$.

However, the edges (boundaries) of the surface walls contain half-saddle and half-node; including quarter-saddle at the corners (see figure 4.5). A schematic has been shown (see figures 3.2(b)-3.2(d)) for possible different critical points on the intersection of different walls of the driven cavity.

A plot of distinct critical points on the five solid walls of the cavity has been provided in figure 4.7. The list of these critical points found by our computation for $Re = 1000$ are also presented in table 4.1. In this table, we provide spatial locations and topological nature of those critical points.

We observe that our identification of critical points is consistent with the work of Surana *et al.* [136]. In figure 4.8, we present the divergence of the wall-shear stress along with the streamtraces of velocity field on the base ($z = 0.001$ plane) of the cavity. From the figure, one can clearly see that the separation line lies in the region where $\vec{\nabla}_x \cdot \vec{\tau} < 0$; and the region where $\vec{\nabla}_x \cdot \vec{\tau} > 0$ determines the presence of attachment line. In order to distinguish these regions, two different color code has been used in figure 4.8. Further, a close look at table 4.1 reveals that the separation line originates from saddle S_{13}

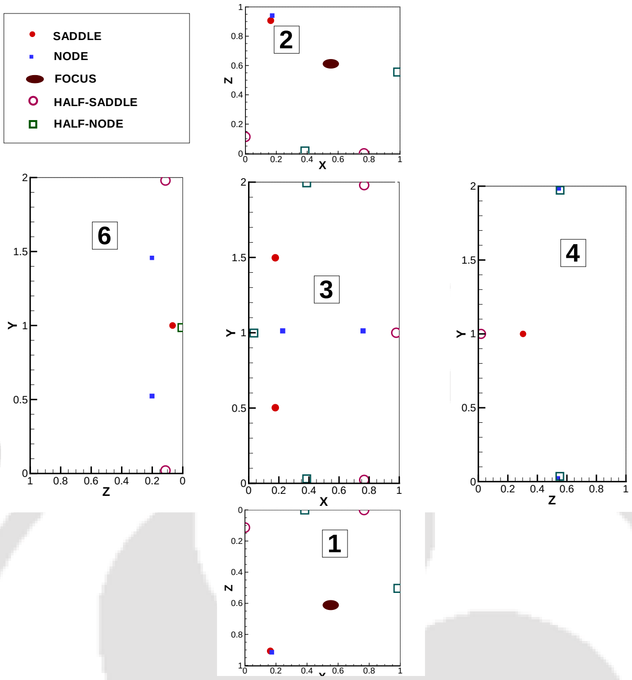

Figure 4.7: *Different critical points on five stationary walls of the driven cavity for* $Re = 1000$.

Table 4.1: *Topology of critical points in 3D lid-driven cavity for Re=1000 on the stationary walls.*

Wall	**Critical Points**	**Nature**	**Spatial Location**	$\vec{\nabla}_x \cdot \vec{\tau}$	$\det\vec{\nabla}_x\vec{\tau}$
Wall 1	S_{11}	Saddle	(0.1639, 0, 0.9069)	1.9103	-11661.8695
	N_{11}	Repelling-Node	(0.1608, 0, 0.9275)	7.2547	11.0124
	F_{11}	Focus	(0.5542, 0, 0.6116)	-0.1205	1471.4910
Wall 2	S_{21}	Saddle	(0.1639, 2, 0.9069)	1.9103	-11661.8695
	N_{21}	Repelling-Node	(0.1608, 2, 0.9275)	7.2547	11.0124
	F_{21}	Focus	(0.5542, 2, 0.6116)	-0.1205	1471.4910
Wall 3	N_{13}	Repelling-Node	(0.7469, 1, 0)	29.3727	195.9993
	N_{23}	Attracting-Node	(0.2129, 1, 0)	-7.7421	12.0861
	S_{13}	Saddle	(0.1763, 0.5022, 0)	-5.6257	-5063.9238
	S_{23}	Saddle	(0.1763, 1.4978, 0)	-5.5873	-5076.2662
Wall 4	S_{14}	Saddle	(1, 1, 0.3027)	0.0027	-1754.1068
	N_{14}	Attracting-Node	(1, 0.0107, 0.527)	-1.8292	0.7348
	N_{24}	Attracting-Node	(1, 1.9893, 0.527)	-1.6361	0.5123
Wall 6	S_{16}	Saddle	(0, 1, 0.0668)	0.0126	-5823.0552
	N_{16}	Repelling-Node	(0, 0.5299, 0.1893)	1.1832	0.2723
	N_{26}	Repelling-Node	(0, 1.4701, 0.1893)	2.9035	1.5675
				$\vec{\nabla}_x \cdot \partial_x\vec{\tau}$	$\det\vec{\nabla}_x\partial_x\vec{\tau}$
Wall 1 corners	HN_{113} or HN_{131}	Half-Node	(0.3601, 0, 0)	-30.7986	198.7325
	HS_{113} or HS_{131}	Half-Saddle	(0.767, 0, 0)	23.2328	-40013.8855
	HS_{116} or HS_{161}	Half-Saddle	(0, 0, 0.1133)	-13.2690	-75388.1913
	HN_{114} or HN_{141}	Half-Node	(1, 0, 0.529)	-32.5095	209.7640
Wall 2 corners	HN_{123} or HN_{132}	Half-Node	(0.3601, 2, 0)	-30.7986	198.7325
	HS_{123} or HS_{132}	Half-Saddle	(0.767, 2, 0)	23.2002	-40111.7285
	HS_{126} or HS_{162}	Half-Saddle	(0, 2, 0.1133)	-13.2112	-74992.8725
	HN_{124} or HN_{142}	Half-Node	(1, 2, 0.529)	-30.6884	206.3394
				$\vec{\nabla}_x \cdot \partial_y\vec{\tau}$	$\det\vec{\nabla}_x\partial_y\vec{\tau}$
Wall 3 corners	HN_{136} or HN_{163}	Half-Node	(0, 1, 0)	-1.0216	0.2315
	HS_{134} or HS_{143}	Half-Saddle	(1, 1, 0)	2.1012	-1966.3911

$(\det\vec{\nabla}_x\vec{\tau} < 0)$ and ends at a stable node N_{23} $(\vec{\nabla}_x \cdot \vec{\tau} < 0)$; the attachment line originates from unstable node N_{13} $(\vec{\nabla}_x \cdot \vec{\tau} > 0)$ and ends at a half-saddle HS_{123}/HS_{132} $(\det\vec{\nabla}_x\partial_x\vec{\tau} < 0)$. All saddles, nodes, foci, half-saddles, half-nodes identified by us are non-degenerate. These facts are in accordance with the necessary and sufficient criteria for separation and attachment lines (see section 4.3.3).

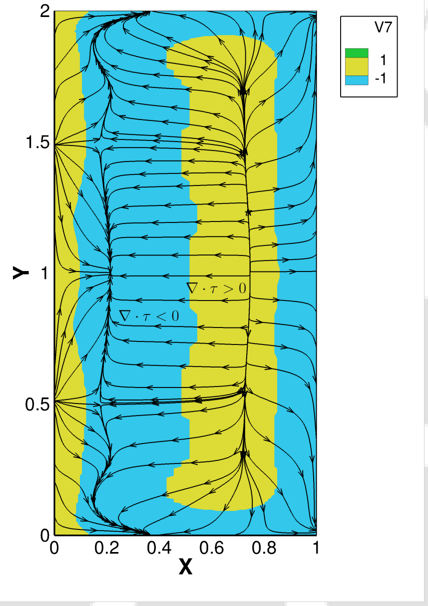

Figure 4.8: *Divergence of the wall-shear stress along with the streamtraces on the base of the cavity.*

In figure 4.9, we depict the steady flow structure in the plane $x = 0.5$ of the cavity for $Re = 1000$ which is obtained using a time-marching strategy. The spatial locations of the possible critical points along with their topological classification also have been presented in table 4.2.

Observation: In the cross-flow plane, $p = 0$, $\sum F = 8$, $\sum N = 0$, $\sum S = 6$, $\sum HN = 2$, $\sum HS = 6$ and $\sum QS = 0$. As such the critical points found out by us follow Poincaré-Bendixson formula (see theorem 4.3.2). Note that in their study of flow topology in a steady 3D lid-driven cubical cavity for $Re = 400$, Sheu and Tsai [131] counted foci as nodes in the Poincaré-Bendixson formula despite of the fact that foci and nodes as critical points have distinct characteristics.

Indian Institute of Technology Guwahati

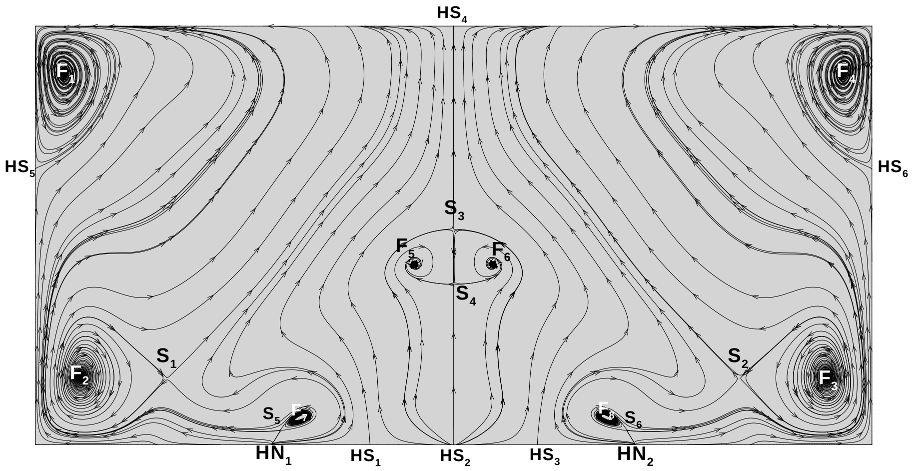

Figure 4.9: *Flow structure on the cross-flow plane* $x = 0.5$ *for* $Re = 1000$.

Table 4.2: *Topology of critical points on the cross-flow plane* $x = 0.5$ *for* $Re = 1000$.

Critical Points	**Spatial Location**	**Nature**
F_1	(0.0680, 0.8884)	Focus
F_2	(0.1097, 0.1619)	Focus
F_3	(1.8903, 0.1619)	Focus
F_4	(1.9320, 0.8884)	Focus
F_5	(0.9049, 0.4300)	Focus
F_6	(1.0951, 0.4300)	Focus
F_7	(0.6345, 0.0652)	Focus
F_8	(1.3655, 0.0652)	Focus
S_1	(0.3157, 0.1581)	Saddle
S_2	(1.6843, 0.1581)	Saddle
S_3	(1.0000, 0.5142)	Saddle
S_4	(1.0000, 0.3831)	Saddle
S_5	(0.5860, 0.0341)	Saddle
S_6	(1.4140, 0.0341)	Saddle
HN_1	(0.5657, 0.0000)	Half-Node
HN_2	(1.4343, 0.0000)	Half-Node
HS_1	(0.7995, 0.0000)	Half-Saddle
HS_2	(1.0000, 0.0000)	Half-Saddle
HS_3	(1.2005, 0.0000)	Half-Saddle
HS_4	(1.0000, 1.0000)	Half-Saddle
HS_5	(0.0000, 0.6610)	Half-Saddle
HS_6	(2.0000, 0.6610)	Half-Saddle

4.4.1.2 Vortical coreline and limiting cycle

In the following, we study the flow topology on the plane which is locally orthogonal to a curve/line, known as vortical coreline/corecurve. All the trajectories in the neighbourhood of this line roll up/wrap around it and formation of a 3D vortex is observed. As such the vortical coreline is regarded as the main signature of the vortical flow phenomena (refer to the schematic of vor-

Indian Institute of Technology Guwahati

tical coreline of figure 3.7 in which the normal plane is spanned by the vectors $\hat{n}$ and $\hat{b}$). The vortical coreline is the collection of spatial locations, at which points u_n and u_b (with respect to the velocity $\vec{V} = u_n\hat{i} + u_b\hat{j} + u_t\hat{t}$) on n-b-plane with an outward normal $\hat{t}$ vanishes.

In figure 4.10, we depict the vortical coreline in the cavity for both $Re =$ 1000 and 3200. The solid red lines in the middle of the cavity indicate the presence of primary vortical structure; on the other hand other two near the base of the cavity confirm presence of corner vortex structures for $Re = 1000$. The solid red curves near the base in figure 4.10(b) indicate the presence of TGL vortices in the spanwise direction and the trace of U-shaped structures are also evident. This phenomena will be discussed in section 4.4.2 in detail.

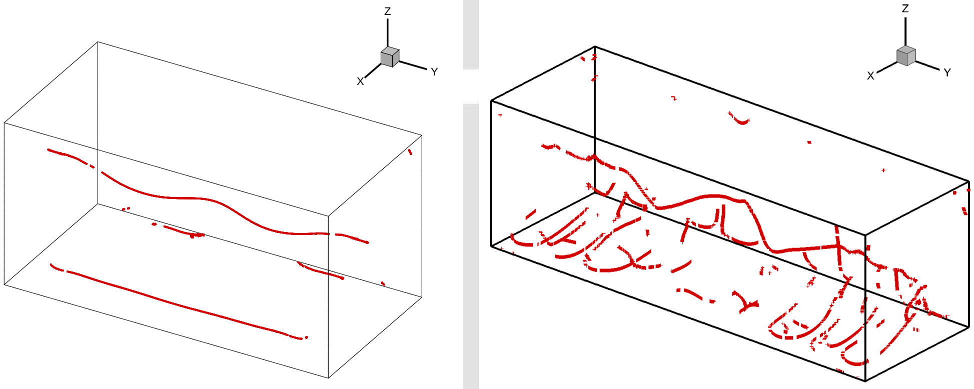

(a) (b)

Figure 4.10: *Vortical coreline in the cavity for (a) SAR=2:1, $Re = 1000$ and (b) SAR=3:1, $Re = 3200$.*

A snapshot of the swirling motion of the fluid particles around the vortical coreline is presented in figure 4.11. The flow is seeded with markers near the two stationary end walls. The fluid particles exhibit a swirling motion around the vortical coreline in its neighbourhood. One can observe that in the plane of symmetry, the fluid particles spiral towards the primary vortex center in either side of the span-wise direction. For the vortical coreline corresponding to the secondary vortex, similar phenomenon is observed, but now the particles spiral outward from the plane of symmetry. The monotonically spiralling motion of fluid particles in the span-wise direction is a clear effect of no-slip boundary

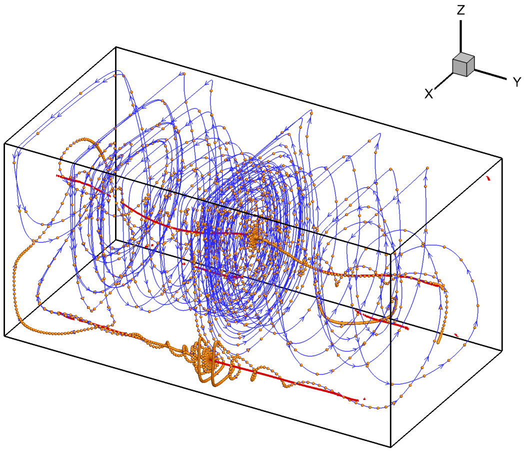

Figure 4.11: *Spiralling motion around the vortical coreline in the cavity.*

walls.

Moreover, spiralling streamlines around the point of intersection of n-b-plane and the vortical coreline pave the way for the existence of limit cycles. According to the Dulac theorem [69], streamlines on n-b-plane are of closed-type in the form of a ring like structure. This ring is called a limit or limiting cycle.

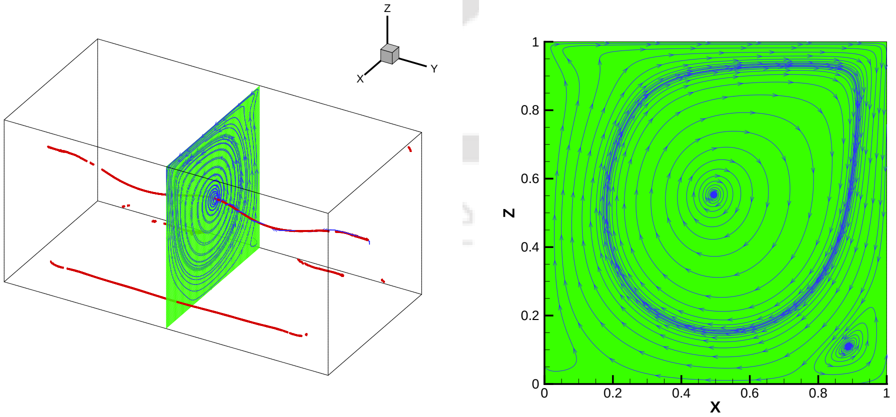

(a) (b)

Figure 4.12: *(a) Flow structure in the plane of symmetry* $y = 1.0$ *(b) Close up view of of the limiting cycle on the plane* $y = 1.0$.

The projection of the streamlines of the normal plane over the cross-flow plane remains invariant (topologically equivalent [9, 97]). So the presence of limit cycle can also be observed in the cross-flow plane (plane of symmetry) as well. In figure 4.12(a), we present flow structure in the plane of symmetry ($y = 1.0$) of the cavity. We observe that spiralling streamlines in the vicinity of the point of intersection of the vortical coreline and the plane $y = 1.0$ ensure the presence of limiting cycle. A close up view of the flow structure on $y = 1.0$ has been shown in figure 4.12(b) in which formation of the limiting cycle (closed trajectory/ring-like trajectory) clearly visible (the blue solid curve). The presence of limiting cycle has also been observed at bottom right corner associated with the secondary vortex.

4.4.2 Topology of Taylor-Görtler-like vortices

Flow simulations for $Re = 3200$ have been carried out on a non-uniform space grid of size $101 \times 301 \times 101$ with a time step $\Delta t = 10^{-4}$. In the current study under consideration, we attempt to explore various topological aspects namely U-shaped vortex structures, mushroom-shaped structures which are closely associated with the formation of TGL vortices. To the best of our knowledge, these aspects have yet not been explored by the scientific community for this flow.

The eddies which are distributed along the span-wise direction of the cavity in the planes perpendicular to the lid and enlarge along the streamlines of the primary eddy are known as "Taylor–Görtler-like (TGL)" vortices. These vortices resemble the Taylor vortices present between two rotating cylinders and the Görtler vortices occurring at concave surface of the boundary layer. The TGL vortices develop in pairs having different orientations and occur in the downstream secondary eddy region (DSE) of the cavity. These vortices occur due to force imbalance between the viscous and centrifugal forces.

In figure 4.13, we depict a snapshot of the instantaneous flow topology on the cross-flow plane at time $t = 1092.976$ in which one can see the formation of TGL vortices for $Re = 3200$ along the span-wise direction ($\text{SAR} \equiv \text{L} : \text{B} = 3$) of the cavity. From our computation, we were able to trace eight pairs of TGL vortices. We adopt the following nomenclature to mark them in the flow field.

From the left, TL1 denotes the first TGL vortex pair, TL2 the second and so on. We observe that each of the pairs is asymmetric in nature. These pairs of counter-rotating vortices ejects low speed fluid up from the lid of the cavity and on either side, drives high speed fluid down towards the stationary walls of the cavity. This event causes a non-uniform/irregular velocity distribution along the span of the cavity. Further, a close look at TGL pairs reveals that each of the pair consists of two unstable foci. This facts ensure the flow instability; the appearance of flow transition and may be regarded as the onset of turbulence phenomenon.

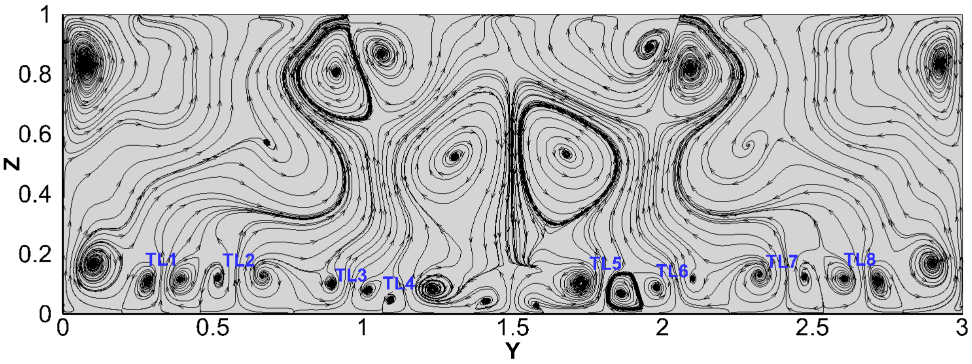

Figure 4.13: *Formation of TGL vortices on the cross-flow plane* $x = 0.5$.

It is well known that, a flow is separated if its surface flow pattern contains at least one saddle point [36]. Further, in the flow domain, two nodes or two saddle points having same nature (separation or reattachment) cannot be connected by the same skin friction line. The separation (attachment) line presents a string of nodes and saddle points. A schematic of such structure has been shown in figure 4.14 where two nodes are separated by a saddle point is topologically consistent as the surface flow pattern is associated with either separation or an attachment process due to orientation of skin friction lines. To the best of our knowledge, this is the first time the presence of a string of nodes and saddles ensuring the appearance of TGL vortices along the span of the cavity have been observed. In figure 4.15, we provide vector plots of

TGL vortices and wall shear stress patterns. We notice that node and saddle points occur in an alternate fashion and separation (attachment) line is formed along the span-wise direction of the cavity which ensures the presence of TGL vortices along the span of the cavity.

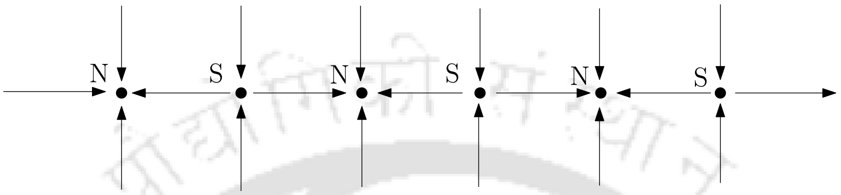

Figure 4.14: *Schematic of a string of nodes and saddle points in an alternate fashion.*

A recent study by Liu *et. al* [94] via direct numerical simulation (DNS) of flow transition over a flat plate reveals that due to the breakdown of hairpin vortex structure, a U-shaped vortex is generated to form a turbulent spot [134]. The presence of this U-shaped vortex structures leans towards the event of onset of turbulence. In the present study under consideration, we for the first time observe the presence of these structures on the floor of the 3D cavity. Note that the floor of the cavity can be thought of locally as a flat plate having finite span. In figure 4.16, a global view of the U-shaped vortex structure in the cavity is presented by plotting the λ_2 isosurfaces.

We observe that U-shaped vortex structures are present along the span-wise direction of the cavity. Note that each TGL pair is associated with two U-shaped vortex structures. A close look at figures 4.17-4.18 reveals that while one of the vortex of a TGL pair associated with a leg of a U-shaped vortex, the other one associated with a leg of a another U-shaped vortex. The cross-section of U-shaped vortex legs with the $z = 0.5$ plane detects a TGL pair. This fact clearly exemplifies that each TGL pair consists of two counter-rotating vortices. In order to have a clear view of this fact, one TGL pair namely TL1 is encircled in the figures 4.17(a) and 4.18(a) and close up view of TL1 has been shown in figures 4.17(b) and 4.18(b).

Our study has also been able to identify mushroom-shaped structures along the span of the cavity. Such a structure consists of a cap and a stem, schematic of which has been shown in figure 4.19. In figure 4.20, we depict vorticity

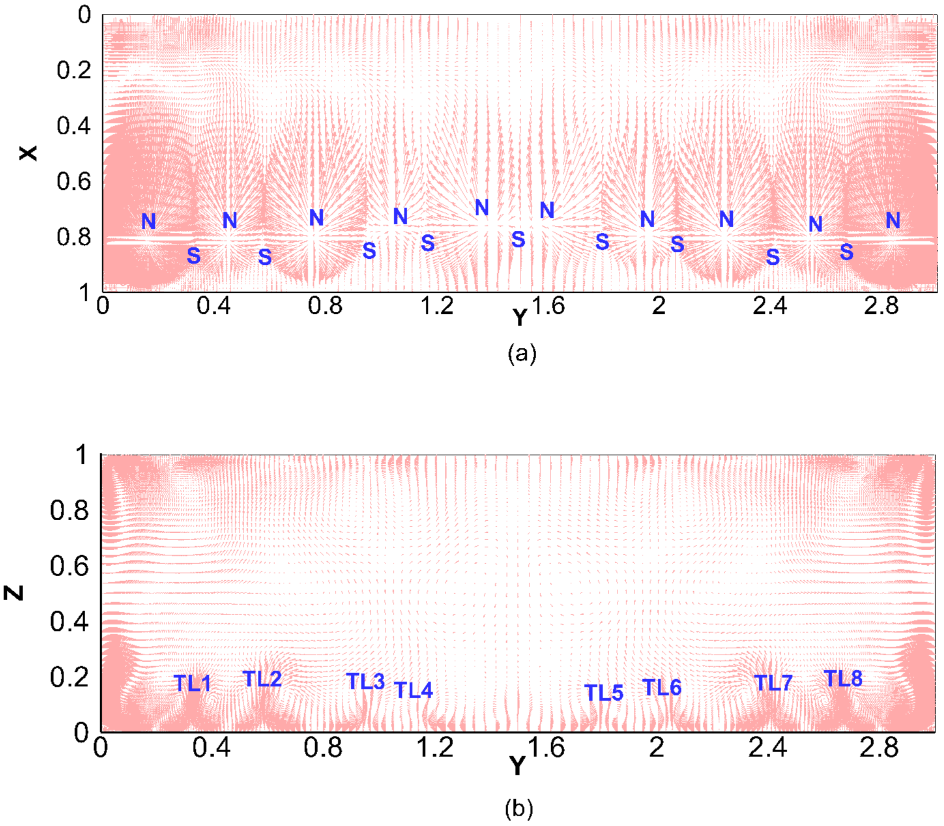

Figure 4.15: *Vector plots of (a) instantaneous wall-shear stress patterns on the plane* $z = 0.01$ *and (b) TGL vortices (on the plane* $x = 0.5$*) along the span-wise direction of the cavity.*

Institute of Technology Gu

contour on the plane $x = 0.5$ in which mushroom-shaped structures are clearly visible. One typical structure has been encircled in the figure for a clear view. The development of these mushroom-shaped structures is triggered due to high non-linear effects in the y-z plane. The fluid (low momentum) adjacent to the 'stem' of the mushroom ejects from the stationary walls of the cavity and returns back in the region of maximum shear that give rise to the formation of mushroom 'cap'. The streamtraces and vector plots in the y-z plane (see figure 4.13 and figure 4.15(a)) confirms the non-linear regions in which boundary layer flow is dominated by these mushroom-shaped structures. These mushroom-shaped structures are nothing but TGL vortices as observed

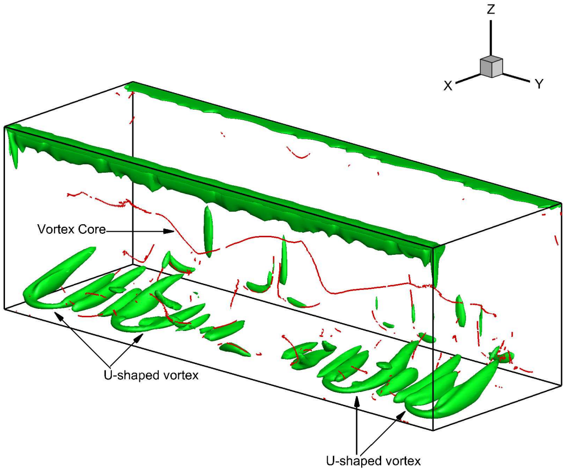

Figure 4.16: *U-shaped vortex structures in the cavity.*

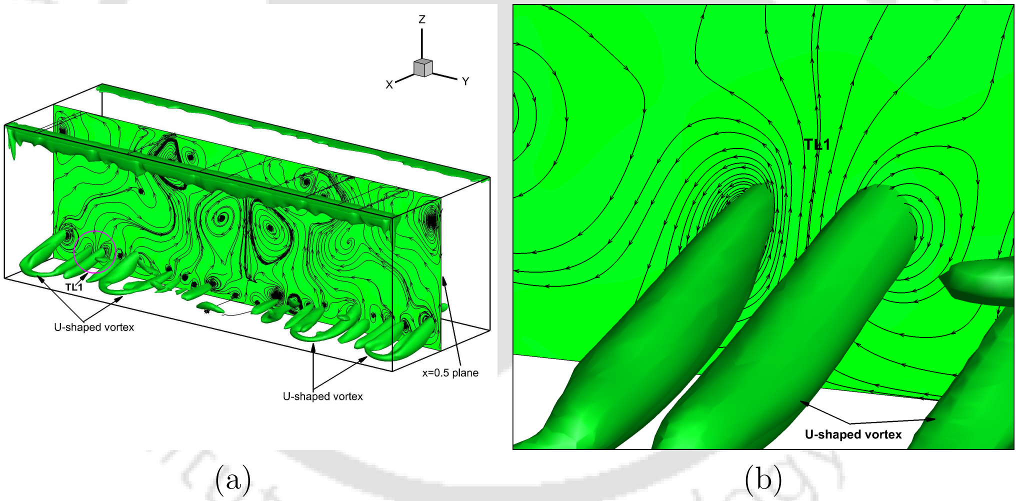

(a) (b)

Figure 4.17: *(a) TGL vortices on the plane* $x = 0.5$ *and U-shaped vortex structures in the cavity (b) a close up view of a TGL pair* TL_1

by Aidun *et. al* [3] experimentally. We noticed that the size of these mushrooms are not uniform and distributed in a random manner which resembles somewhat wavy and irregular flow patterns. This indicates rapid evolution of flow transition/instability leading to turbulence. Note that we were able to trace eight mushroom structures which is consistent with the total number of TGL pairs present in the cavity.

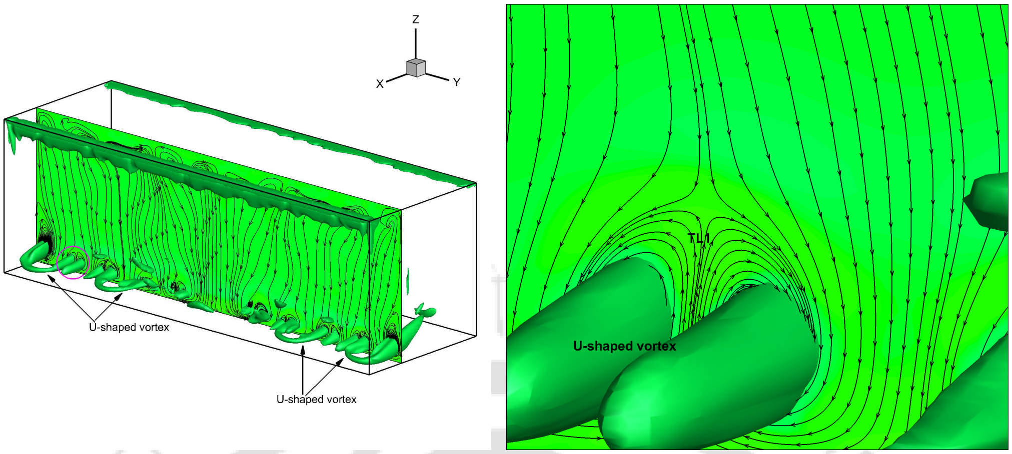

(a) (b)

Figure 4.18: *(a) TGL vortices on the plane $x = 0.7$ and U-shaped vortex structures in the cavity (b) a close up view of a TGL pair TL_1*

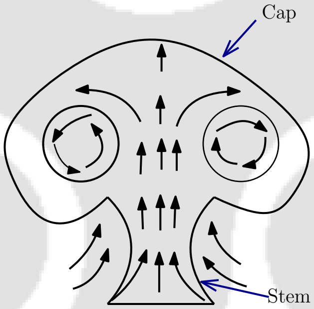

Figure 4.19: *Schematic of mushroom-shaped vortex structure.*

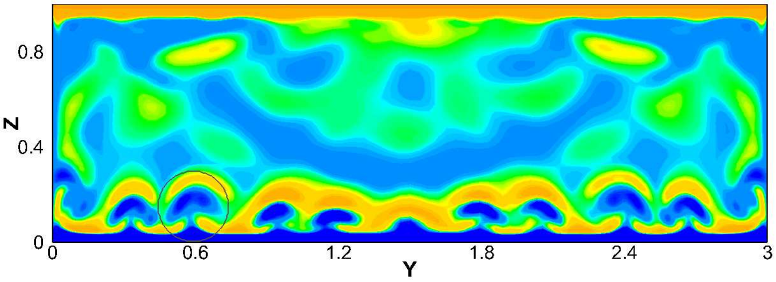

Figure 4.20: *TGL vortices in the form of mushroom-shaped structures.*

4.5 Conclusion

In this work, we present a detailed discussion of three-dimensional flow in a rectangular cavity with values of SAR ($\equiv$ L : B = 2, 3), subject to a constant velocity on the lid. We explore some physical insight into the vortical flow by using rigorous theories in the field of topological fluid dynamics. For this purpose, we have computed the flow inside the cavity by solving 3D N–S equations for $Re = 1000,\ 3200$ by the commercially available software ANSYS Fluent 15.0 version on non-uniform space grids on a parallel set up. We post-process the computed data to identify different form of critical points present in the flow field. The topological structures in the neighbourhood of these critical points have been explained in detail. The Poincaré-Bendixson formula has been used to ensure that all the critical points obtained through eigenvalue analysis are dynamically possible. Further, the topology of TGL vortices has been discussed. We observe some interesting flow structures such as U-shaped vortex structures and mushroom shaped structures which are closely associated with the formation of TGL vortices indicating the onset of turbulence.

After investigating the corner vortices of the 2D and 3D lid-driven cavity flow from the computed data of the numerical solution of the N–S equations, we will now endeavour to throw some more light on these vortices through theoretical approach. The rest of the thesis is devoted to the development of some new theories on corner vortices by employing some concepts from the geometric theories of incompressible viscous flows.

Institute of Technology

Chapter 5

EXISTENCE OF TOPOLOGICAL EQUIVALENCE CLASS IN MOFFATT VORTICES

5.1 Introduction

A close look at the existing literature [5, 30, 82, 86, 99, 100, 106, 107, 129] reveals that the study of Moffatt vortices is mainly confined to the flow in a wedge-shaped geometry, in particular in the triangular cavity in Stokes regime. These vortices, which are characterized by their size and intensities, follow a geometric sequence. This fact, which was first established by H. K. Moffatt [106, 107] was used by later researchers as a check for the existence of such vortices in their numerical computation of the flow in triangular cavities [40, 70].

Demonstration of such a check is also evident from figures 5.1(a)-(b) where a comparison between the streamlines obtained from the experimental results of Taneda [140] and numerical results obtained through the HOC computation of flow in a lid-driven triangular cavity for Stokes flow by us (for further details refer to Appendix A) are presented side by side. Further probing figure 5.1(c), one can see a clear reversal in the direction of flow in successive vortices alternatively where dashed lines indicate that the direction of rotation of a vortex

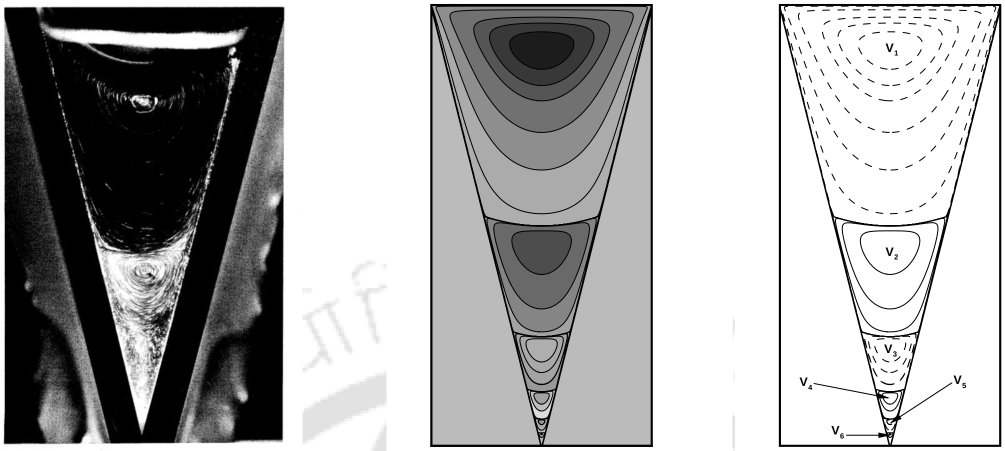

(a) (b) (c)

Figure 5.1: *(a) Streamlines from Taneda's experiment* [140] *(b) simulation from our HOC computation and (c) flow reversal in successive vortices.*

is clockwise and solid lines denote anti-clockwise one. In the present study, we endeavour to provide a distinct characterization of the Moffatt vortices by utilizing this very notion of orientation.

Right from the time the term Moffatt vortices [106, 107] has been coined, their study has mostly been through the eigenvalue analysis. To the best of our knowledge, the study of Moffatt vortices under the purview of their topology and critical point theory has not been carried out before. In the current study, we for the first time, establish some novel theories on Moffatt vortices where we propose two topological equivalence [1] classes of Moffatt vortices. Firstly, we characterize the equivalence class in terms of orientation-preserving homeomorphism, a key concept in the field of general topology [8, 101, 122].

Our next approach is through half-saddle point structures from critical point theory [9, 36, 148]. Both these approaches convey the same conclusion on their topological equivalence. We further quantify the centers of vortices as fixed points in the topological sense through Brouwer fixed-point theorem [52] and define boundary of a vortex as circle cell by extending the same idea

---

[1] In the present context, two objects are topologically equivalent means that they are homeomorphic and having the same direction of rotation.

of Ma and Wang [97] for divergence-free vector fields.

5.2 Preliminaries

In the following, we provide some definitions, theorems and results of general topology [8, 43, 52, 101], topological fluid dynamics [9, 97, 118, 122] and some of our own newly developed theories, which will be used in the next chapter to prove the finiteness of Moffatt vortices.

5.2.1 Notations

- $\mathbb{R}$ is the set of real numbers.
- $\mathbb{N} = \{1, 2, 3, \cdots\}$ is the set of natural numbers.
- $\tilde{V} = \{q\colon q \in V_i$, the i-th vortex in the sequence of Moffatt vortices$\}$.
- M is a planar region.
- On the boundary ∂M of the region M, $\hat{\tau}$ denotes the tangential vector and $\hat{n}$ the normal vector.
- $T_pM = \{w \mid w$ is tangent to M at $p\}$.
- $TM = \{(p, T_pM) \mid p \in M\}$ is the tangent bundle of M.
- Assume $r \geq 1$ is an integer. Let $\mathcal{C}^r(TM)$ be the space of all r-th differentiable vector fields v on M.
- $\mathcal{C}^r_{\hat{n}}(TM) = \{v \in \mathcal{C}^r(TM) \mid v \cdot \hat{n} = 0$ on $\partial M\}$.
- $\mathcal{D}^r(TM) = \{v \in \mathcal{C}^r_{\hat{n}}(TM) \mid \nabla \cdot v = 0\}$.
- $\mathcal{B}^r_0(TM) = \{v \in \mathcal{D}^r(TM) \mid v = 0$ on $\partial M\}$.

5.2.2 Some essential topology

In the following, we provide some definitions, theorems and results of topology [8, 9, 43, 52, 101, 122] which will be used in appropriate junctures later to prove the finiteness of Moffatt vortices.

5.2.2.1 The notion of topological mapping

Definition 5.2.1. A topological mapping (homeomorphism) between two regions in a plane is a one-to-one and bi-continuous mapping: each point m is mapped onto exactly one point m' and that distinct points m_1 and m_2 are mapped onto distinct points m_1' and m_2', and the mapping is continuous either way.

An intuitive notion of a topological mapping of the plane onto itself is delineated by Andronov *et al.* [7] which is as follows: "imagine the plane is to be made from rubber which is deformed in some way, stretching and squeezing it at various points, but without tearing or folding. Any topological mapping of the plane into itself is either a deformation of the above type (without tearing and folding) or a mirror-reflection of the plane followed by such a deformation."

For further illustration, let us consider the following two dynamical systems in a region $D \subset \mathbb{R}^2$:

$$\dot{x} = f_1(x) \tag{5.1}$$

$$\dot{x} = f_2(x) \tag{5.2}$$

where, $x = (a, b) \in D$ and f_1, f_2 are sufficiently smooth functions on D. The phase portraits (whole set of solution curves) of the systems (5.1) and (5.2) have the same topological structure if there exists a topological mapping T which maps D onto D and which takes paths of (5.1) over into paths of (5.2). If two points x_1 and x_2 lie on the same path of the system (5.1), then their images Tx_1 and Tx_2 lie on the same path of the system (5.2). Also, if two points x_1 and x_2 lie on the same path of the system (5.2), then their images $T^{-1}x_1$ and $T^{-1}x_2$ lie on the same path of the system (5.1). As for example, phase portraits in a regular domain (domain in the phase space where f_1, f_2 are non-zero vector functions) can be mapped by a homeomorphism onto a family of parallel trajectories (see figure 5.2).

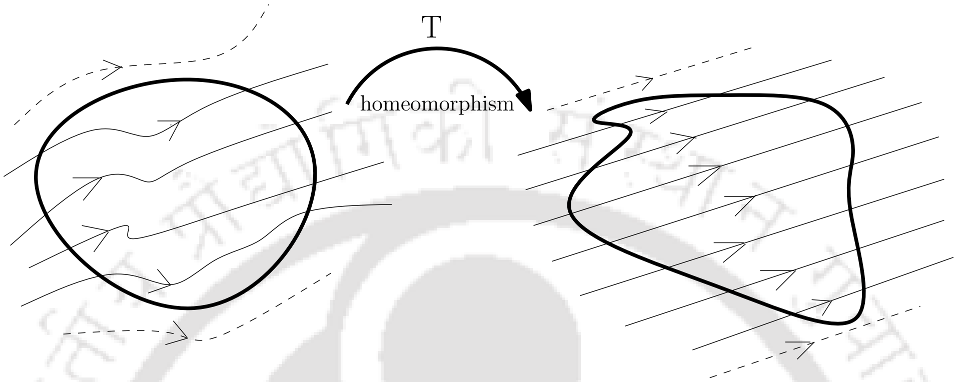

Figure 5.2: *Schematic of a topological mapping of the trajectories in a regular domain into a field of parallel paths.*

Definition 5.2.2. Let A_1 and A_2 be subsets of $\mathbb{R}^n$ with $n = 2$ or 3, and let $h : A_1 \to A_2$ and $g : A_1 \to A_2$ be homeomorphisms. We say that h and g are isotopic if there exists a continuous function $F : A_1 \times I \to A_2$ where $I = [0, 1] \subset \mathbb{R}$ such that $F(x, 0) = h(x),\ F(x, 1) = g(x)$, and for every fixed $t \in I$, the function $F(x, t)$ is a homeomorphism.

Intuitively, two homeomorphisms are isotopic if one can be continuously deformed into the other. An important result in topology is that every homeomorphism $h : \mathbb{R}^n \to \mathbb{R}^n$ with $n = 2$ or 3 is isotopic to either the identity map or to a reflection map, but not to both. In the existing literature, these two types of homeomorphisms are defined as follows.

Definition 5.2.3. Let h be a homeomorphism from $\mathbb{R}^n$ to itself with $n = 2$ or 3. If h is isotopic to the identity map, then we say that h is *orientation preserving*. If h is isotopic to a reflection map, then we say that h is *orientation reversing*.

Every homeomorphism of $\mathbb{R}^2$ or $\mathbb{R}^3$ is either orientation preserving or reversing. An orientation reversing homeomorphism maps an embedded graph to its mirror image, possibly deforming it as well, while an orientation-preserving homeomorphism maps an embedded graph to itself or to a deformation of the graph in space. A reflection map is orientation reversing, whereas any translation or rotation is orientation preserving.

5.2.2.2 The Brouwer fixed-point theorem

Definition 5.2.4. A mapping f of an open set $U \subset \mathbb{R}^n$ into $\mathbb{R}^m$ is called smooth if it has continuous partial derivatives of all orders.

Theorem 5.2.5. [52] *Any smooth map* Ψ *of the closed unit ball* $B^n \subset \mathbb{R}^n$ *into itself must have a fixed point, that is,* $\Psi(x) = x$ *for some* $x \in B^n$.

5.2.3 Geometric theories of incompressible viscous flows

Definition 5.2.6. [97] A point $p \in M$ is called a singular point of $v \in \mathcal{C}^r_{\hat{n}}(TM)$ if $v(p) = 0$.

Definition 5.2.7. [97] A singular point p of $v \in \mathcal{C}^r_{\hat{n}}(TM)$ is called non-degenerate if the Jacobian matrix of v at p, $J_v(p)$ is invertible.

Definition 5.2.8. [97] A vector field $v \in \mathcal{C}^r_{\hat{n}}(TM)$ is called regular if all singular points of v are non-degenerate.

Definition 5.2.9. [97] An orbit $\{\Phi(x,t)\}_{t\in\mathbb{R}}$ is called a closed (periodic) orbit if there is a time $T_0 > 0$ such that for any $t \in \mathbb{R}$, $\Phi(x,t) = \Phi(x, t + T_0)$.

Definition 5.2.10. [97] Let $v \in \mathcal{D}^r(TM)$ and $p \in M$ be a center; then, there is an open neighbourhood C of p, such that for any $x \in C(x \neq p)$, the orbit $\{\Phi(x,t)\}_{t\in\mathbb{R}}$ is closed. The largest such neighbourhood C of p is called a circle cell of v.

Lemma 5.2.11. [97] *Let* $v \in \mathcal{D}^r(TM)(r \geq 1)$. *Then, each non-degenerate singular point of* v *is either a center or a saddle point. A non-degenerate singularity on the boundary* ∂M *must be a saddle point.*

Theorem 5.2.12. (Structural Classification Theorem I [97]): *Let* $v \in \mathcal{D}^r(TM)(r \geq 1)$ *be regular. Then, the topological structure of* v *(flow field in the context of the current study) consists of a finite number of connected components, which are of the following types:*

(1) *circle cells, which are homeomorphic to open disks,*

(2) *circle bands, which are homeomorphic to open annuli,*

(3) *ergodic sets, and*

(4) *saddle connections.*

Definition 5.2.13. [**97**] Let $u \in \mathcal{B}_0^r(TM)(r \geq 2)$.

(1) A point $p \in \partial M$ is called a ∂-regular point of u if $\dfrac{\partial u_{\hat{\tau}}(p)}{\partial n} \neq 0$; otherwise, $p \in \partial M$ is called a ∂-singular point of u.

(2) A ∂-singular point $p \in \partial M$ of u is called non-degenerate if

$$\det \begin{bmatrix} \frac{\partial^2 u_{\hat{\tau}}(p)}{\partial \hat{\tau}^2} & \frac{\partial^2 u_{\hat{\tau}}(p)}{\partial \hat{\tau} \partial \hat{n}} \\ \frac{\partial^2 u_{\hat{n}}(p)}{\partial \hat{\tau} \partial \hat{n}} & \frac{\partial^2 u_{\hat{n}}(p)}{\partial \hat{n}^2} \end{bmatrix} \neq 0$$

A non-degenerate ∂-singular point of u is also called a ∂-saddle point of u.

Lemma 5.2.14. [**97**] *Each non-degenerate ∂-singular point of $u \in \mathcal{B}_0^r(TM)$ is isolated. Therefore, if all ∂-singular points of u on ∂M are non-degenerate, then the number of ∂-singular points of u is finite.*

Definition 5.2.15. [**97**] Let $\Omega \subset M$ be a closed domain. A point $p \in \Omega$ of v (flow field) is called Ω-boundary saddle (half-saddle) if there are only three orbits connecting p in Ω.

5.2.4 Some essential theories of limit cycle

Definition 5.2.16. [**118**] Consider the autonomous system

$$\dot{\mathbf{x}} = \mathbf{f}(\mathbf{x}) \tag{5.3}$$

with $\mathbf{f}(\mathbf{x}) \in \mathcal{C}^1(E)$ where E is an open subset of $\mathbb{R}^2$. A point $\tilde{\mathbf{p}} \in E$ is an *ω-limit point* of the trajectory $\phi(\cdot, \mathbf{x})$ (which is a function from $\mathbb{R}$ to E) of the system (5.3) if there is a sequence $t_n \to \infty$ such that $\lim\limits_{n \to \infty} \phi(t_n, \mathbf{x}) = \tilde{\mathbf{p}}$.

TH-1927_126123012

Similarly, if there is a sequence $t_n \to -\infty$ such that $\lim_{n\to\infty} \phi(t_n, \mathbf{x}) = \tilde{\mathbf{q}}$, then the point $\tilde{\mathbf{q}}$ is called an *α-limit point* of the trajectory $\phi(\cdot, \mathbf{x})$.

Definition 5.2.17. [118] The set of all *ω-limit points* of a trajectory Γ is called the *ω-limit set* of Γ and it is denoted by $\omega(\Gamma)$. The set of all *α-limit points* of a trajectory Γ is called the *α-limit set* of Γ and it is denoted by $\alpha(\Gamma)$.

Definition 5.2.18. [118] A *limit cycle* Γ of a planar system is a closed solution curve (cycle) of (5.3) which is the α or *ω-limit set* of some trajectories of (5.3) other than Γ. If a cycle Γ is the *ω-limit set* of every trajectory in some neighbourhood of Γ, then Γ is called an *ω-limit cycle* or *stable limit cycle*; and if Γ is the *α-limit set* of every trajectory in some neighbourhood of Γ, then Γ is called an *α-limit cycle* or *unstable limit cycle.*

Theorem 5.2.19. (Dulac [118]): *In any bounded region of the plane, a planar analytic system (5.3) with $\mathbf{f}(\mathbf{x})$ analytic in $\mathbb{R}^2$ has at most a finite number of limit cycles.*

Theorem 5.2.20. (Poincaré [118]): *A planar analytic system (5.3) cannot have an infinite number of limit cycles which accumulate on a cycle of (5.3).*

Theorem 5.2.21. (The generalized Poincaré-Bendixson Theorem [118]): *Suppose that $\mathbf{f}(\mathbf{x}) \in \mathcal{C}^1(E)$ where E is an open subset of $\mathbb{R}^2$. Then, the system (5.3) has only a finite number of critical points, it follows that $\omega(\Gamma)$ is either a critical point of (5.3), a period orbit of (5.3), or that $\omega(\Gamma)$ consists of a finite number of critical points, $\tilde{\mathbf{p}}_\mathbf{1}, \tilde{\mathbf{p}}_\mathbf{2}, \cdots \tilde{\mathbf{p}}_\mathbf{m}$, of (5.3) and a countable number of limit orbits of (5.3) whose α and ω limit sets belong to $\{\tilde{\mathbf{p}}_\mathbf{1}, \tilde{\mathbf{p}}_\mathbf{2}, \cdots \tilde{\mathbf{p}}_\mathbf{m}\}$.*

In the following, we provide some of our newly developed theories on Moffatt vortices which will be utilized for proving our hypothesis (see section 6.4) on the finiteness of Moffatt vortices.

5.3 Topological equivalence class of Moffatt vortices

In this section, we propose two equivalence classes of corner vortices based on different characterizations. By a corner we mean the point of intersection of two converging solid boundaries or one solid boundary and an interface [82, 106, 107, 132]. The corner may be sharp or rounded off. In case of the later which renders the boundary to be analytic, the corner is locally the point of maximum curvature. Note that in situations where the boundary is locally smooth and the point of maximum curvature does not exist as in the flow in a semi circular cavity [50], the vortices occurring in the flow cannot qualify as Moffatt vortices.

5.3.1 Equivalence class in terms of orientation

The members in the sequence of Moffatt vortices are of two types: **(a)** Vortices having positive orientation (anti-clockwise rotation), **(b)** Vortices having negative orientation (clockwise rotation). Let us consider the set $\mathcal{M}$ of all sequence of Moffatt vortices. We can define a relation $\tilde{\rho}_R$ on $\mathcal{M}$ such that for any two sequences of vortices $\mathcal{V} = (V_1, V_2, \cdots), \mathcal{V}' = (V_1', V_2', \cdots) \in \mathcal{M}$, $\mathcal{V} \ \tilde{\rho}_R \ \mathcal{V}'$ iff the leading vortex of both $\mathcal{V}$ and $\mathcal{V}'$ have the same orientation (i.e. same direction of rotation). Clearly $\tilde{\rho}_R$ is an equivalence relation [123] on $\mathcal{M}$ which partitions $\mathcal{M}$ into two equivalence classes. For each of these two classes we can characterize the sequences of vortices with odd and even indices respectively in the following manner:

Class-I (cl_1): Moffatt vortices in which the leading vortex has positive orientation.

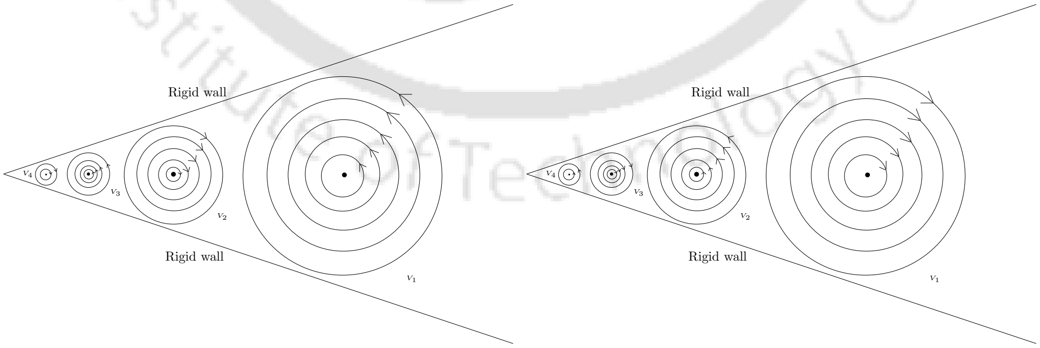

(a) (b)

Figure 5.3: *Sketch of Moffatt vortices (a) class-I (cl_1) and (b) class-II (cl_2).*

Odd sequence of Moffatt vortices say, $V_{2n-1}^{cl_1}(= D_{2n-1}^{cl_1}$, closed disks): All the members in this sequence have positive orientation, and even sequence of Moffatt vortices say, $V_{2n}^{cl_1}(= D_{2n}^{cl_1}$, closed disks): All the members in this sequence have negative orientation. For reference, see figure 5.3(a).

Class-II (cl_2): Moffatt vortices in which the leading vortex has negative orientation.

Odd sequence of Moffatt vortices say, $V_{2n-1}^{cl_2}(= D_{2n-1}^{cl_2}$, closed disks) : All the members in this sequence have negative orientation, and even sequence of Moffatt vortices say, $V_{2n}^{cl_2}(= D_{2n}^{cl_2}$, closed disks): All the members in this sequence have positive orientation. For reference, see figure 5.3(b).

Moreover, it can be observed that these two classes (cl_1, cl_2) differ by a reflection map [91].

In view of topology, each of the vortex is essentially a rotating disk (as our flow situation is in 2D set up) with a fixed center. The members from the subsequence of indices with same parity has the same direction of rotation. Topologically any two disks are equivalent. Since here we are also considering the direction of rotation (referred as orientation), so the members from the odd sequence (similarly even) become topologically equivalent. Also, any two consecutive members are not equivalent as they differ by orientation (reflection map). Note that in the present context, a topological equivalence is not only a homeomorphism, but also an orientation preserving homeomorphism. The upshot of the above discussions are the following remarks:

Remark 5.3.1. Any two members in the odd sequence are (topologically) equivalent for both class of Moffatt vortices. Similarly any two members in the even sequence are (topologically) equivalent for both class of Moffatt vortices.

Remark 5.3.2. Any member in the sequence $\{V_{2n-1}^{cl_1}\}_{n\in\mathbb{N}}$ is topologically equivalent to a member in the sequence $\{V_{2n}^{cl_2}\}_{n\in\mathbb{N}}$. So we can define a map $f_n : V_{2n-1}^{cl_1} \longrightarrow V_{2n}^{cl_2}$, which is an orientation preserving homeomorphism. Similarly, any member in the sequence $\{V_{2n}^{cl_1}\}_{n\in\mathbb{N}}$ is topologically equivalent to a member in the sequence $\{V_{2n-1}^{cl_2}\}_{n\in\mathbb{N}}$. So we can define a map $g_n : V_{2n}^{cl_1} \longrightarrow V_{2n-1}^{cl_2}$, which is an orientation preserving homeomorphism.

5.3.2 Equivalence class in terms of the nature of critical points

We observe that for the corner vortices under consideration, only two types of half-saddles can be present on the boundary of the flow domain leading to separation and reattachment and thus paving the way for the creation of a vortex [36, 97]. We define them as *half-saddle of first kind* HS^1 leading to separation and *half-saddle of second kind* HS^2 leading to reattachment. Note that for a particular corner vortex, the point of separation and the point of reattachment lies on different boundary walls lying on the either side of the corner point. In the sequence of vortices, for any two members in succession, the rear of the former coincides with the front of the later (figure 5.4).

We consider $\mathcal{L}$ as the set of the portions of the streamlines connecting the points of separation and reattachment for a particular vortex as shown in figure 5.4. Define a relation ρ_R on $\mathcal{L}$ such that for $L_1, L_2 \in \mathcal{L}$, $L_1 \ \rho_R \ L_2$ iff the corresponding half-saddles on the same boundary wall are of same type (HS^1 or HS^2). It can be easily verified that ρ_R is an equivalence relation [123] which partitions $\mathcal{L}$ into two equivalence classes. Furthermore, the equivalent members in $\mathcal{L}$ occur at indices with same parity.

Remark 5.3.3. Equivalence class in terms of orientation and half-saddles defined in this way is essentially same as the nature of half-saddles (HS^1 or HS^2) determines the orientation of the vortices. As any vortex is homeomorphic to a disk, the two classes cl_1 and cl_2 of vortices defined in section 5.3.1 are classified only by the orientation of their leading vortices which are determined by the types of the corresponding half-saddles HS^1 or HS^2.

As mentioned earlier in chapter 2, the vorticity distribution along the solid walls also confirms the region in which Moffatt vortices exist and the change in sign in vorticity reveals two vortices in succession having opposite orientation. Therefore, the same conclusion on equivalence class can be made by making use of vorticity as well.

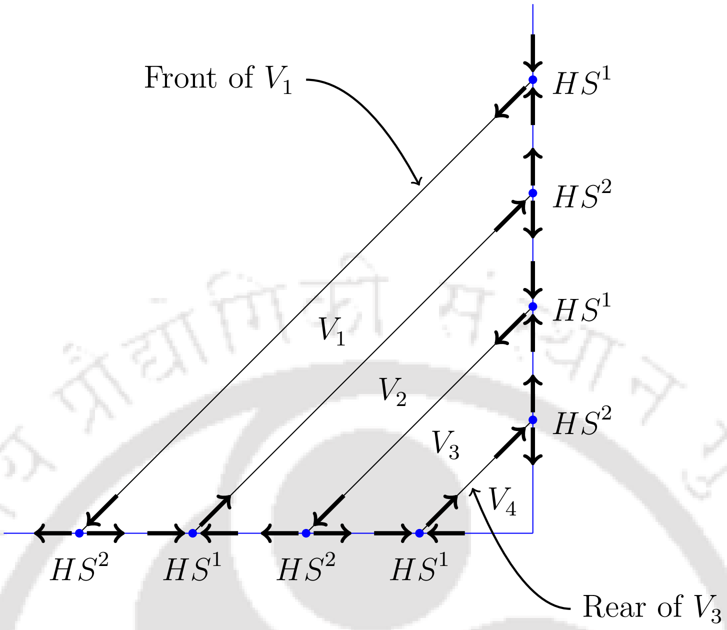

Figure 5.4: *Sketch of equivalence class of Moffatt vortices in terms of half-saddle structures.*

5.4 Some novel theories on Moffatt vortices

In the following, we provide some of our newly developed theories on Moffatt vortices that would be utilized in the next chapter to prove our hypothesis on the finiteness of Moffatt vortices in the light of geometric theories of incompressible viscous flows.

5.4.1 Centers of Moffatt vortices: topological fixed points and its neighbourhood

Proposition 5.4.1. *The centers of Moffatt vortices are fixed points.*

Proof. Consider the i-th member V_i in the sequence of Moffatt vortices whose center is at C_i. When the flow reaches steady state, vortices will not deform. In other words at steady state, if we consider a fluid particle on a specific streamline ($\overline{SL}$) then the particle will always move along that specific streamline.

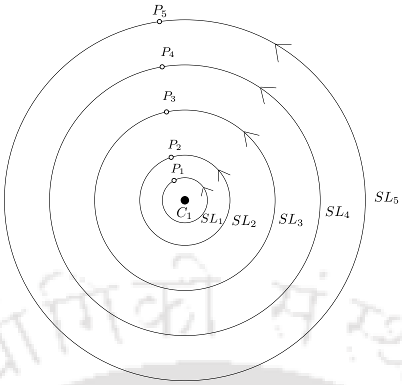

Figure 5.5: *Periodic motion of the particles* ($P_i,\ i = 1, 2, \cdots, 5$) *along the streamlines* ($\overline{SL}_i,\ i = 1, 2, \cdots, 5$) *in the interior of a vortex.*

As such, in steady state we can define a map $\mathcal{F}_i : \overset{\circ}{\tilde{V}_i} \longrightarrow \overset{\circ}{\tilde{V}_i}$, where $\overset{\circ}{\tilde{V}_i}$ is in the interior of $\tilde{V}_i$ obtained from V_i by removing only the outermost streamline and the map $\mathcal{F}_i$ defines the rotation of the vortex V_i. Then each streamline will remain invariant under that function. As $\mathcal{F}_i$ is a linear map, so $\mathcal{F}_i$ is a smooth map. Therefore by Brouwer fixed-point theorem (theorem 5.2.5) with $n = 2$, $\mathcal{F}_i$ must have atleast one fixed point but any point in $\overset{\circ}{\tilde{V}_i}$ other than the center is lying on a streamline and hence they are always in a periodic motion. Therefore, in the present case the center of the vortex C_i is the only possible fixed point. ☐

Definition 5.4.2. Let C_i be the center of the i-th vortex V_i in the sequence of Moffatt vortices. If an open neighborhood $\mathcal{O}$ ($\subset \tilde{V}$) of C_i is considered, then for any $x \in \mathcal{O}(x \neq C_i)$, the orbit (the path followed by fluid particles around the center C_i) $\{\Phi(x, t)\}_{t \in \mathbb{R}}$ is closed (periodic). The largest such neighborhood $\mathcal{O}$ of C_i is defined as the "*Circle Cell*" of the vortex V_i.

5.5 Conclusion

Till date, Moffatt vortices have been characterized only through the establishment of a common ratio of their computed size and intensities. To the best of our knowledge, no rigorous mathematical characterization of these vortices with respect to their orientations is available in the existing literature. In an effort in this direction, we have established two topological equivalence classes of Moffatt vortices, firstly in terms of orientation preserving homeomorphism and then critical point theory. We further established the centers of these vortices as fixed points through Brouwer fixed-point theorem and identified the boundary of a vortex as a circle cell. The outcome of our results may be useful in describing complicated flow structures in a much simpler form in a transformed domain and prove to be an important addition to the existing geometric theories of incompressible viscous flows.

Chapter 6

MOFFATT VORTICES: CONCERNS AND FINITENESS

6.1 Introduction

Terms like incompressible, inviscous, inviscid and impermeable have assimilated into the vocabulary of fluid mechanics quite naturally over the years [12, 146]. The usage of these words seems to be very casual in the context of the desired precision or accuracy in the field of mathematics and physics, yet one has hardly seen any resistance from the scientific community over the usage of such words. This is probably because of the fact that all these words have certain quantification. For example, although no flow in the real world is incompressible, this word has wide acceptability among the fluid dynamics community for fluid flows that remain within a Mach number limit of 0.3 [12, 111]. However, it is highly questionable whether one can apply the word *infinite* in the same vein to mean a large number of vortices present in a fluid flow without actually quantifying it, which of course is an extremely difficult task.

In fluid flow, vortices are known to occur in the vicinity of solid walls where the flow separation takes place; scientists have always been keener on probing the nature of vortices at the corners of solid structures. The existence of a sequence of vortices at the corner of a solid structure for internal flows with decreasing size and rapidly decreasing intensity has been indicated by several physical experiments and mathematical asymptotics [106, 107, 108, 109, 140]. Their formation, evolution and progression on different geometrical and physical set up have always generated a lot of interest both among fluid dynamicists and mathematicians.

Study on the existence of these vortices dates back to the pioneering work of Dean and Montagnon [35] which was later consolidated by Moffatt [106, 107]. The flow near a sharp corner between two bounding planes was considered, and a solution of the purely biharmonic equation (refer to chapter 2 along with equation 2.3) for creeping flows [115] was sought in terms of some exponential power Λ of the distance $\tilde{r}$ from the corner. They found this Λ to be a complex number when the angle between the two planes is less than about 146°, implying infinite oscillations and hence concluded that there exists an infinite sequence of counter-rotating eddies as one approaches the corner. From then onwards, the occurrence of such corner vortices has always been synonymous with the existence of an infinite sequence, albeit without any rigorous mathematical proof.

In 1976, Collins and Dennis [30] computed the flow of a slow viscous fluid in a curved tube having a cross-section in the shape of a right-angled isosceles triangle. They observed vortices of Moffatt's type firstly in the secondary flow in the 45° corners and then in the 90° corner. By refining the grid size of the computational domain and making use of extrapolation technique, they were able to trace 13 vortices in the 45° corner and six pairs of vortices in the 90° corner. In 1979, Taneda [140] tried to establish the existence of these vortices experimentally in a V-notch (refer to figure 5.1(a)). However, the visualization of such vortices revealed the existence of only a few of them in the corner. This was followed by several theoretical and numerical experiments [56, 61, 93, 102, 108, 109, 113, 121] on vortices around a corner in solid structures.

Of late, there has been a surge of theoretical and numerical studies on corner vortices [15, 37, 57, 59, 82, 86, 87, 100, 129, 130, 132] for slow viscous flows on different geometries. In 1993, Anderson and Davis [5] presented a local picture of steady, two-dimensional (2D) viscous flow of two fluids in a wedge. They figured out the geometries for which wedge angle solutions exist and also identified conditions under which Moffatt vortices may appear in the flow. During 1998–2000, Shankar and Deshpande [130], and Deshpande and Milton [37] studied their existence in the 2D lid-driven cavity flow. In 2004, Biswas *et al.* [15] investigated laminar backward-facing step flow for a wide range of Reynolds number and based on the theory of Moffatt [106, 107] concluded that an infinite sequence of closed eddies with decreasing size and strength is expected for $Re \to 0$. It is worth mentioning that although the study of Moffatt vortices mainly pertains to Stokes flow, the sequence of corner vortices in decreasing size and intensity can be found for moderately high Reynolds number flows as well. This is well documented in the enormous amount of numerical and experimental studies being carried on the lid-driven cavity flows [4, 16, 37, 84, 125, 128, 130, 135].

In 2005, Malhotra *et al.* [99] reviewed the Moffatt problem [106] and established the existence of Moffatt vortices for the Stokes flow bounded by two concentric coaxial cones with a common vertex through eigenvalue analysis and described the asymptotic distribution of eigenvalues for both even and odd flow structures. In the same year, Malyuga [100] considered Stokes flow in a circular cone driven by a non-zero velocity applied to the boundary within the ring which is represented in the form of Fourier series. They obtained the transcendental equation for the eigenvalues, which determines the asymptotic behavior of the flow in the neighbourhood of the vertex, arriving at a conclusion similar to that drawn by Moffatt [106, 107]. In 2014, Kirkinis and Davis [82], by using a hydrodynamic theory of liquid slippage on a solid substrate, concluded that an infinite sequence of vortices is formed in a moving liquid wedge of certain angle between a gas–liquid interface and a rigid boundary. Other recent studies in this direction worth mentioning are [59, 86, 87, 129, 132].

All the existing geometrical theories on incompressible viscous flows (Bakker [9], Délery [36], Ma and Wang [97], Hirschel [62], Wu *et al.* [148]) based on the concept of dynamical system [118] express vortical structures in terms of critical points in bounded domains. They again indicate a strong opposition to the notion of infiniteness. The presence of a sequence of vortices at the corner of decreasing size and intensity has already been emphatically established by laboratory and numerical experiments [15, 16, 30, 37, 57, 140]. However, neither any authentic mathematical proof nor any laboratory experiment to date has been able to establish their infiniteness. Despite this, mathematicians and engineers alike went on producing a large number of works on the topic of corner vortices propounding their infiniteness, as evidenced by many of the works cited above. Even for the lid-driven cavity problem, which over the years has become the most frequently used benchmark problem among the computational fluid dynamics community and is an obvious example of internal incompressible viscous flow, claims of infinite sequence of corner vortices can still be found in the existing literature for this problem [4, 37, 84, 125, 128, 130, 135].

No one paid much attention to this issue until Gustafson *et al.* [55] in 1989 tenderly questioned on the issue of the infiniteness of Moffatt vortices. They concluded that the computational resources available at that time was not sufficient to provide a conclusive answer to this question (more details in section 6.2.2). As such, the task of establishing the finiteness of the sequence of such vortices still remained unaccomplished and the question on infiniteness unanswered. The objective of the current study is to explore a possible missing link between the contrasting theories of Moffatt vortices [5, 15, 19, 30, 37, 59, 61, 82, 86, 87, 93, 99, 100, 102, 106, 107, 108, 109, 113, 121, 129, 132] and the recent geometrical theories on incompressible viscous flows [9, 36, 49, 62, 80, 97, 112, 148]. We endeavour to bridge the gap between the factions by pinpointing what could have possibly gone wrong with the assumptions of the existing theories upon which the conclusion of infiniteness is built.

Based on the newly developed theories by us in the previous chapter and some recent developments in geometric theory of incompressible viscous flows [36, 97], and making use of some elementary mathematical analysis [123], we prove that the sequence of Moffatt vortices in fluid flows around solid corners is finite [1]. It is worth mentioning that the same conclusion is reached by tackling the hypothesis through six different approaches. Note that in all the studies mentioned above, two-dimensional flows as an idealization of a three-dimensional (3D) one or 3D flows having symmetry in one direction were considered. As such, all the theories developed by us will be considered over plane regions only.

---

[1] A part of this work has been published in *Zeitschrift für angewandte Mathematik und Physik (ZAMP)* [74].

6.2 The backdrop

In this section, we throw some lights on the controversies surrounding the notion of infiniteness. They include the mathematical origin of Moffatt vortices, certain concerns and questions over the issue which have not been settled till date.

6.2.1 The mathematical origin of the infiniteness of Moffatt vortices

The existence of vortices in a flow field is a highly non-linear phenomena, and most importantly there exists an inherent connection between their occurrence and the non-linear nature of Navier–Stokes (N–S) equations [16]. However, the theoretical studies on Moffatt vortices seek the solution of the biharmonic form of the steady-state N–S equations for Stokes flow in the stream function, which is a linear one (for details refer to chapter 2 along with equation 2.1). Thus, it completely annihilates all the effects of non-linearity.

The existence of the infinite sequence of vortices follows from ones ability in arriving at a solution of the form (2.3). Making use of (2.3), one can find the transverse component of velocity on the plane $\phi = 0$ as [106]

$$v_{\phi=0} \sim \gamma \frac{1}{\tilde{r}} \left(\frac{\tilde{r}}{\tilde{r}_0} \right)^{p_1+1} \sin \left(q_1 \ln \frac{\tilde{r}}{\tilde{r}_0} + \tilde{\epsilon} \right). \tag{6.1}$$

The notion of an infinite sequence of vortices near the corner comes from the above expression by concluding that it changes sign infinitely as $\tilde{r} \to 0$.

Another argument for the existence of the infinite sequence of eddies near a solid corner comes from the concept of discrete self-similarity. Consider a flow domain $\Omega = \{(x, y) \in \mathbb{R}^2 | x = \tilde{r} \cos \phi,\ y = \tilde{r} \sin \phi,\ \tilde{r} > 0,\ |\phi| < \alpha\}$, in which these vortices are defined in the flow whose stream function ψ has the form

$$\psi(x, y) = \mathrm{Re}\Big(\tilde{r}^{\Lambda} \{ A \cos \Lambda\phi + B \cos(\Lambda - 2)\phi \} \Big),$$

where Re stands for real part of a complex variable expression; $A,\ B$ are some nonzero constants which satisfy

$$\sin 2(\Lambda - 1)\alpha + (\Lambda - 1)\sin 2\alpha = 0.$$

Then, if one considers the scaling

$$\psi_{\Lambda_n}(x, y) = \Lambda_n^{-(\mathrm{Re}(\Lambda-1)+1)}\psi(\Lambda_n x, \Lambda_n y),$$

both the domain Ω and stream function ψ remain invariant under the action of the scaling $(x, y) \to (\Lambda_n x, \Lambda_n y)$, where $\Lambda_n = \dfrac{2\pi n}{|\mathrm{Im}(\Lambda - 1)|}$, $n \in \mathbb{N}$; i.e, $\psi_{\Lambda_n}(x, y) = \psi(x, y)$. Note that the concept of discrete self-similarity follows from this notion of invariance.

6.2.2 The concerns over infiniteness

Probably, the earliest concern over the infiniteness of Moffatt vortices was raised by Gustafson *et al.* in the year 1989 [55] where they questioned: "*Are any of these entities truly infinite dimensional?*"; by *these entities*, they meant the corner vortices in the famous lid-driven cavity flow. According to them, what actually had been sought physically or mathematically was their existence in a large finite dimensional dynamical system without further venturing into the metaphysical meaning of infinity. They further mentioned that though the theory predicts an infinite sequence of vortices at the corner of the solid structure (in particular they considered the lower two corners of the driven cavity), it is a linearized one (see equation (2.1)). They had reservations on how much it depends on the linearizing assumptions and for what range of Reynolds numbers it continues to hold for the full non-linear N–S equations, which are the governing equations for incompressible viscous flows [55]. Then in 1991, Gustafson and Sethian [58] commented "*When one reflects on the fact that all dissipation has been represented in the single term $\nu\Delta u$, one can conclude that at these scales the N–S equations are near the limits of their validity*". Gustafson [58] further commented "*I conjecture that there will only be a finite number of corner eddies allowed by the non-linear equations*". True to their concerns, many of the existing and recent theorems on separation of incompressible viscous flows [9, 36, 62, 80, 97, 148] lean toward the existence of a finite number of vortices in a finite domain including corners.

In their study of unsteady separation induced by a vortex, Obabko and Cassel [112] discuss about the viscous–inviscid interaction leading to spike formation. The presence of a primary vortex induces an adverse pressure gradient along a solid surface, and the aforesaid interaction accelerates the spike formation leading to the formation of secondary vortices. The mechanisms for the creation of the tertiary, quaternary and the succeeding vortices are the same [80]. The *structural bifurcation theory* of Ghil *et al.* [49], by predicting the exact location and time of the birth of a vortex clearly, establishes that the birth of the vortices in the sequence in a corner occurs one after another in succession. The clear implication of all these theories [97] is the following fact: The birth of two vortices in succession or any two vortices in the same sequence cannot take place at the same instant of time. This is in direct contrast with the infiniteness of corner vortices in steady-state flow resulting from the solution of (2.1), which would have taken infinite time to reach the steady state through time marching.

It is a well known fact that the formation of the so-called infinite sequence of vortices in Stokes flow is due to the effect of certain stirring/rotating force far from the corner [5, 19, 30, 59, 61, 82, 87, 93, 99, 100, 102, 106, 107, 108, 109, 113, 129, 132]. A further undermining into the existing literature reveals a very vague picture of the extent of the domains over which the flow is considered. If the source of the force is an infinite distance away from the corner, the effect of stirring/rotating force will decrease gradually with a proportional fall in the intensity of the force or the strength of the vortices at their centers as one moves away from the source. At a certain distance from the source of the given force, no effect of it will be felt. Thus, the process of the formation of the vortices will be well over much before reaching the corner. On the other hand, the theory of Moffatt vortices considers the existence of the infinite sequence vortices in the neighborhood of the corner where $\tilde{r} \to 0$. Thus a source force at an infinite distance from the corner nullifies the presence of the so-called infinite sequence of vortices at the corner indicated by mathematical asymptotes.

One of the main sources of the infiniteness of the sequence of vortices is the so-called discrete self-similarity of infinite degree of these vortices, which unfortunately is not physically feasible. Though it is quite a common practice to quote natural objects like fern and cauliflower exhibiting self-similarity, it exists only under finite degrees of magnification (up to finite number of stages/steps). Moreover, if this notion of infinite degree of magnification is to hold true, even in Stokes flow, one must be able to actually accommodate an entire "tail" of eddies sequence below the Kolmogorov (see section 6.2.3.1) length scale, which is physically impossible.

6.2.3 The unanswered questions

Only recently, in 2006, Moffatt and Branicki [19] have broached upon the possibility of the finiteness of these sequences of vortices for certain cases. Analyzing the time-periodic evolution of Stokes flow near a corner, they concluded that depending upon the smoothness and angle of the corner, and on the nature of the forcing, an infinite sequence of corner eddies may be present if the corner is sharp. On the other hand, if corners are rounded off so that the boundary is everywhere analytic, it is expected that a finite sequence of eddies may still form in regions near points of maximum curvature on the boundary. But the big question here is: Is there a slight transition from a smooth to a sharp corner good enough to trigger infiniteness to the sequence of vortices? If so, how does one quantify this sudden jump from finite to infinite number of vortices and then again, what is this thin line between the extent of smoothness and sharpness leading to this enormous jump?

Moreover, as mentioned in section 6.2.1, the concept of Moffatt vortices comes from the solution of the linearized version of the N–S equations. These equations are derived under the assumption of "*Continuum Hypothesis*" [12, 146]. According to this hypothesis, even the smallest volume scale cannot be zero; for example, for air, it is of the order 10^{-9}mm^3 containing approximately 3×10^7 molecules under standard conditions.

Note that an infinite sequence of vortices of decreasing size renders a size zero to the vortices belonging to the tail of the sequence (see proof 4 of theorem 6.4.1 in section 6.4). However, this conclusion stems from the solution of equation (2.1) which is built under the assumption of continuum hypothesis requiring a minimum non-zero volume scale. This clearly contradicts the existence of an infinite number of vortices in the corner of solid structures. The Kolmogorov length scale corroborates this fact.

6.2.3.1 Kolmogorov (length scale) theory

Stokes flow and turbulent flows are at the extreme ends of the spectrum of incompressible viscous flow regime characterized by the Reynolds numbers. Therefore, the mention of the Kolmogorov length scale [92, 95, 104, 105, 120] may sound totally irrelevant in the context of Stokes flow. Juxtaposed to this, this length scale plays an important role in our analysis. The Kolmogorov's theory clearly states that vortices cannot exist below a certain non-zero length scale [37, 145], since the local value of power density (ε) would be so high that the kinetic energy would be fully dissipated as heat.

An estimate for the scales at which the energy is dissipated is based only on the dissipation rate and viscosity. If the dissipation rate per unit mass (ε) has dimensions (m^2/sec^3) and viscosity, ν has dimension (m^2/sec) then the length scale formed from these quantities is given by

$$\eta = \left(\frac{\nu^3}{\varepsilon}\right)^{1/4}.$$

This length scale is called the Kolmogorov length scale [6, 46, 68].

Note that the smallest length scale for incompressible viscous flows occurs in the turbulent regime. Stokes flow, for that matter laminar flows in the moderate Reynolds number regimes, will have vortices having much bigger scales than those prevalent in turbulent regime. As such, the size of a vortex under consideration in the current study cannot fall below the Kolmogorov length scale.

6.3 The notion of infiniteness: diagnosing the assumptions

In the above, we listed the concerns and the related questions in connection with the infiniteness of Moffatt vortices. In the following, we endeavour to bridge the gap by addressing what actually went wrong with the notion of infiniteness and subsequently providing our own set of proofs on the finiteness of corner vortices. Here, we will reflect upon the shortcomings of the assumptions of the existing theorems upon which the conclusion of infiniteness of corner vortices is built. These observations will help us pinpoint where the existing hypothesis went wrong and pave the way for providing a concrete mathematical basis that predicts the correct physical phenomenon.

The foremost argument provided in favor of the infinite sequence of vortices stems from the velocity component (6.1) arising out of equation (2.1). As discussed in sections 6.2.1 and 6.2.3, (2.1) inherently assumes the "*Continuum Hypothesis,*" can this $\tilde{r}$ in the expression

$$\sin\left(\log\frac{\tilde{r}}{\tilde{r}_0}\right)$$

actually tend to zero? Note that the absolute size of the eddies is directly proportional to the length scale $\tilde{r}_0$. For a large $\tilde{r}_0$, one may mathematically let $\dfrac{\tilde{r}}{\tilde{r}_0} \to 0$ by letting $\tilde{r}_0 \to \infty$, however, in reality $\tilde{r}$ can never tend to zero. Moreover on a finite domain, $\tilde{r}_0$ is bounded and hence can never tend to ∞. As such, the assumption in [106] that $\tilde{r}_0$ is an arbitrary length scale is physically incorrect. This is where the mathematical exuberance tends to overshadow physical reality in a conflicting manner; ideally, one would desire mathematics to go hand in hand with physics.

Furthermore, the number of eddies will decrease even more due to dampening effect after the collision of the fluid with the wall. This effect is completely ignored in this context. Note that the notion of infiniteness comes from the so-called infinite oscillations of the sine waves depicting the stream function value as a solution of (2.1). However, on a finite domain, the number of such waves must be finite and they can be thought as representing discrete oscillations [21]. The maximum wave length that can be accommodated inside a finite domain is the longest inscribable rectilinear length in the domain. The measure of the minimum wavelength is equal to twice the mean free path of the fluid molecules, which is nothing but the average distance travelled by a moving fluid particle between successive collisions. Thus, even when the vortices reach molecular level, this minimum wavelength cannot be zero. As such, the largest number of vortices having a one to one correspondence with the oscillatory waves must be finite.

6.4 Proof of finiteness of Moffatt vortices

In incompressible viscous flows, all equations governing the flows are valid only under the assumption of continuum hypothesis. According to this hypothesis, the smallest volume scale under consideration is non-zero. Besides, the Kolmogorov theory [145] asserts that eddies below a certain size cannot be formed. These facts clearly lean toward the existence of a finite sequence of vortices in the corner. In the following, we prove the finiteness of corner vortices employing the concept of limit of a sequence from mathematical analysis [123]. We further provide an alternative proof by developing the notion of diametric disk. Besides, we provide more proofs which are based on geometric theories of incompressible viscous flows.

Theorem 6.4.1. *Suppose* Ω *is a closed subset of* $\mathbb{R}^2$ *representing an enclosed domain bounded by solid walls (or combination of solid walls and free surfaces). Then, for a steady incompressible viscous flow, for every point* p *on the boundary including corners, any neighborhood of* p *contains at most a finite number of vortices.*

Main proofs:

Proof: Let $\mathcal{V} = (V_1, V_2, \cdots)$ be the sequence of vortices in the corner and the size of the i^{th} vortex be $S(V_i)$ which is defined as the distance of the center of the i^{th} vortex from the corner. In the sequence of vortices, any two consecutive vortices maintain a fixed ratio in size $R = S(V_{i+1}) : S(V_i)$

where $R < 1$ [16, 30, 106, 107]. Consider the sequence $(X_n)_{n\in\mathbb{N}}$, where $X_n = S(V_1)R^{n-1}$ represents the size of the n-th vortex. Since, $R < 1$ therefore, $X_n \to 0$ as $n \to \infty$. From the definition of the limit of a sequence from elementary analysis [123], we obtain for every $\epsilon > 0$, $\exists\ n_0 \in \mathbb{N}$ such that $|X_n| < \epsilon$ for all $n \geq n_0$. In other words, given any such positive ϵ, the vortices in a "tail of the sequence" (all the members after a fixed index, n_0 here) will lie within a distance of ϵ from the corner.

From Kolmogorov length scale (section 6.2.3.1), if we choose $\epsilon = \eta$ then there exists an index $N_\eta \in \mathbb{N}$ such that $|X_n| < \eta$ for all $n \geq N_\eta$. Consequently, the number of vortices can never exceed N_η, which is a finite quantity as in order to have the number of vortices more than N_η , we must have vortices violating the Kolmogorov length scale, which is impossible. ☐

Lemma 6.4.2. *Let us define the diameter of a vortex V by*

$$d = \operatorname{diam}(V) := \min_{x\in\partial\tilde{V}}\{2\|C - x\|_2 \colon C \text{ is the center of the vortex } V\}.$$

This d is always a finite positive real number.

Proof. Note that $\partial\tilde{V} \neq \phi$ and C does not belong to $\partial\tilde{V}$. Therefore, the set $\{2\|C - x\|_2 \colon x \in \partial\tilde{V}\}$ is non-empty. Further the set is bounded below as $\|C - x\|_2 > 0$ for all $x \in \partial\tilde{V}$. Since $\partial\tilde{V}$ being a simple closed curve is a closed set, $\exists\ x_0 \in \partial\tilde{V}$ such that

$$\begin{aligned}\|C - x_0\|_2 &= \inf_{x\in\partial\tilde{V}}\{\|C - x\|_2 \colon C \text{ is the center of the vortex } V\}\\ &= \min_{x\in\partial\tilde{V}}\{\|C - x\|_2 \colon C \text{ is the center of the vortex } V\} > 0.\end{aligned}$$

Letting $d = 2\|C - x_0\|_2$ clearly asserts that it is a finite positive real number. This completes the proof of the lemma. ☐

Alt. Proof: We define diameter, d of a vortex as the diameter of the largest disk which can be inscribed inside the vortex such that the center of the disk coincides with the center of the vortex. We term such a disk as the diametric disk. Refer to figure 6.1 for a schematic of this situation. (Note that the sequence of disks in this figure is actually inscribed inside the boundaries of the sequence of vortices obtained from our own simulation of the flow in a 2D triangular lid-driven cavity for a creeping flow corresponding to $Re = 1$.)

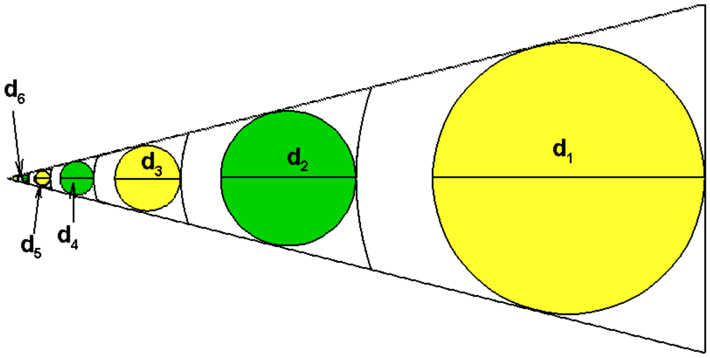

Figure 6.1: *The diametric disks inscribed inside the vortices. The color code used here follows the alternate directions of flow inside successive vortices.*

The above lemma clearly asserts the existence of such a length scale. Furthermore, the diametric disks corresponding to a sequence of vortices are mutually disjoint as otherwise any two intersecting diametric disks will result in overlapping of two distinct vortices which is physically impossible. Now, the sequence of diameters, $(d_n)_{n\in\mathbb{N}}$ corresponding to the sequence of vortices is monotonically decreasing in nature and bounded below as they are positive quantity. So this sequence is convergent and it converges to a non-negative real number, say β.

Case-I: when $\beta \neq 0$, then the total length required to accommodate all those vortices in the flow domain is greater or equal to $\sum_{n\in\mathbb{N}} d_n$. If the sequence of vortices is infinite and we replace d_n by β (limiting diameter) in the summation, we have $\sum_{n\in\mathbb{N}} d_n > \sum_{n\in\mathbb{N}} \beta = \infty$. This is impossible, as size of the fluid flow domain is finite. Therefore, number of vortices in the flow domain cannot be infinite if $\beta \neq 0$.

Case-II: When $\beta = 0$, then in order to have infinite number of vortices in the flow domain, the diameter of the extreme smallest vortex has to drop below the Kolmogorov length scale (see section 6.2.3.1), η (> 0) , feasible length scale to measure fluid vortices. Now as $d_n \to 0$, this implies $\exists\, n_\eta \in \mathbb{N}$ such that $|d_n| < \eta$ for all $n \geq n_\eta$. Consequently, we can never have a vortex with diameter d_n for any $n \geq n_\eta$. Therefore, the maximum possible number of vortices becomes less than n_η, which is finite.

Therefore, the number of vortices in the flow domain must be finite. □

A note on using Kolmogorov length scale for depicting the size of a vortex in the above proofs can be found in Appendix B.

Additional proofs:

1. We established that centers of Moffatt vortices are nothing but fixed points (referred as singular points or critical points) in section 5.4.1 of chapter 5. By theorem 5.2.21, any non linear dynamical system can have only finite number of singular points. If we consider a neighbourhood in the corner of the solid structure, then the neighbourhood contains finitely many singular points. So number of vortices cannot be infinite. □

2. We have already defined the largest neighbourhood of the center of a vortex as a circle cell. By structural classification theorem I (theorem 5.2.12), the number of circle cells must be finite. Since only one circle cell is uniquely connected with one vortex in the flow field, the number of vortices in the corner must be finite. □

3. In the flow domain, flow separation (reattachment) is connected with half-saddle points (boundary saddle points) and separation is the mechanism paving the way for the formation of a new vortex. By lemma 5.2.14, the number of separation points is finite in the flow domain. Therefore, the number of vortices is finite in the flow domain. □

4. This proof is based on the concept of limit cycles. In order to have a clear understanding of limit cycles present in incompressible viscous flows, we exhibit certain results from our own simulation of the 3D lid-driven cavity flow. In 3D flows, vortices are formed swirling around a three-dimensional space curve known as the vortical coreline. Such a scenario can be seen from figure 6.2 where we present the vortical structure around the vortical coreline from our own simulation of the flow for $Re = 1000$. From our previous discussions (refer to section 3.3.1 of chapter 3), we observe that in 3D flows, all the vortices correspond to stable limit cycles originating in foci, while in 2D flows, they are simply *centers* (in dynamical sense) with the streamlines encircling the vortex centers. Thus, each limit cycle gives rise to a vortex in the flow field. Therefore, by theorems (5.2.19), (5.2.20) and (5.2.21) we conclude that number of vortices in the flow field must be finite. ☐

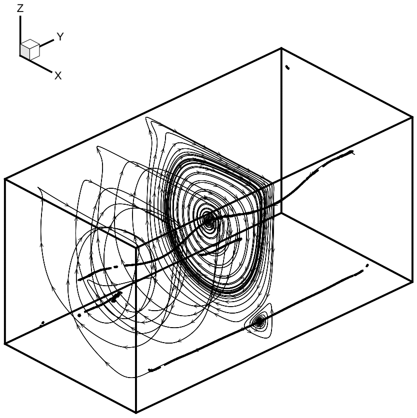

Figure 6.2: *Streamlines at the plane of symmetry for the 3D lid-driven cavity flow at* $Re = 1000$. *One can actually see the vortical structures swirl around the vortical corelines in the figure.*

6.5 Conclusion

In the existing literature, the occurrence of Moffatt vortices has always been synonymous with the existence of an infinite sequence. Despite the continuum axiom providing the base for the governing equations for incompressible viscous flows and the concept of Kolmogorov length scale in vogue, the issue of the finiteness of such sequence has continued to remain unattended. In an effort toward addressing this issue, firstly we have listed the concerns and the pertinent questions on the notion of infiniteness of such sequences and pinpointed where the assumptions of the existing hypothesis might have gone wrong. Making use of some elementary concepts of mathematical analysis and our own construction of diametric disks, we proved that the number of vortices in solid corners in a bounded domain must be finite. Our observations are consistent with the recent developments of geometric theories of incompressible viscous flows. Note that the ideas developed in the current chapter pertains to the specific class of vortices in a corner. In the next chapter, we utilize the same ideas to prove the finiteness of vortices for the more generalized case, viz., in a bounded domain.

Indian Institute of Technology Guwahati

Chapter 7

THE FINITENESS OF VORTICES IN STEADY INCOMPRESSIBLE VISCOUS FLUID FLOW

7.1 Introduction

The study of a general system of vortices generated due to flow separation in incompressible viscous flows in a finite domain has eluded proper investigation for quite a long period of time. Most of the available literatures are concerned about flow in some nice and standard geometry only, such as Moffatt vortices (sequence of vortices present in the solid corners of internal viscous incompressible flows) [16, 82, 86, 100, 106, 129, 132], vortices in a semi-circular domain [50] etc. The finiteness of such system in the general scenario is still wide open. In the present work, we propose a couple of rigorous proofs in the direction of finiteness of such an arbitrary system of vortices.

Studies on the finiteness of critical points in a flow domain found through dynamical system approach can be found scantily in the existing literature [96, 97]. However, the connection between these critical points and the finiteness of vortices in a bounded domain has not yet caught the attention of the scientific community. To the best of our knowledge, no rigorous mathematical proof was provided to establish this connection. In order to achieve this, we utilize the ideas developed in the previous chapters to prove the finiteness of an arbitrary system of vortices in a bounded domain.

7.2 Finiteness of vortices

In this section, we will establish the finiteness of an arbitrary system of vortices (in incompressible viscous flows) through two different approaches. The first proof has its origin in mathematical analysis [123] and recently developed geometric theory of incompressible viscous flows [96, 97]. The second proof leans more on the geometric aspects of the vortices which incorporates of the concept of diametric disk (section 6.4 of chapter 6).

Theorem 7.2.1. *Suppose Ω is a closed subset of $\mathbb{R}^2$, representing an enclosed domain bounded by solid walls (or combination of solid walls and free surfaces). Then for a steady incompressible viscous flow field defined by the velocity vector v, for every point p on the boundary, any neighbourhood of p contains at most a finite number of vortices.*

Proof: It is well known that the process of flow separation on the solid boundaries of a domain leads to the creation of vortices in the flow field. The points on the boundary where this flow separation takes place, are termed as separation points. This class of critical points (for details refer to section 4.3.2 of chapter 4) follow the definition of non-degenerate ∂-singular points [96, 97].

If possible, suppose number of such critical points is infinite. Let us denote the set of separation points by $\mathfrak{C}$. But since the flow domain ($\subset \mathbb{R}^2$) is always bounded, and all these critical points are points from the solid boundary of the flow domain, hence $\mathfrak{C}$ is an infinite bounded subset of $\mathbb{R}^2$. By Bolzano-Weierstrass theorem [123], $\mathfrak{C}$ must have a limit point (c_0 say) in $\mathbb{R}^2$. Therefore, there exists a sequence $(c_k) \subset \mathfrak{C}$ such that $c_k \to c_0$ as $k \to \infty$. Moreover, since flow separation takes place in presence of a solid boundary, this point c_0 has to lie in the flow domain on the solid boundary. Also, the flow field is continuously differentiable, hence a convergent sequence of ∂-singular points must converge to a ∂-

singular point. This contradicts the fact that ∂-critical points are isolated (lemma 5.2.14). Therefore, number of separation points must be finite.

Since, separation points lead to the creation of vortices, the finiteness of separation points leads to the finiteness of vortices (see the note at the end of alt. proof) in the flow domain. □

Alt. Proof: Let V be the set representing a vortex. Define,

$$\mathrm{diam}(V) = \min_{p\in\partial V}\{2\|c_v - p\|_2 : c_v \text{ is the center of the vortex } V\}.$$

Consider the disk of radius $\frac{\mathrm{diam}(V)}{2}$ centered at c_v. This is the largest disk inscribed in the vortex V with center at c_v. We call them the diametric disk of V. Refer to figure 7.1 for a schematic of diametric disk in the lid-driven cavity flow [16].

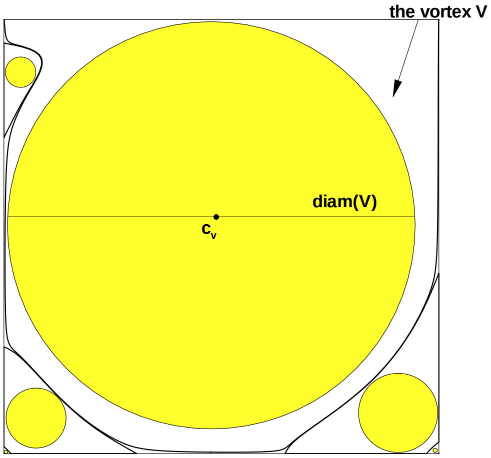

Figure 7.1: *Schematic of diametric disk in the lid-driven cavity flow.*

The total area of the flow domain covered by V must be $\geq \frac{\pi}{4}\,\mathrm{diam}^2(V)$. Moreover, since the vortices are non-overlapping, hence the diametric disks are mutually disjoint. Therefore, the total area covered by the vortices must be $\geq$ the sum of the areas of the diametric disks, i.e.

$$Area(\text{flow domain}) > \sum_{k\in\Lambda} Area(V_k) \geq \frac{\pi}{4}\sum_{k\in\Lambda} \text{diam}^2(V_k),$$

where Λ is an index set. But since none of the diameters can drop below the Kolmogorov length scale [145], therefore

$$\sum_{k\in\Lambda} \text{diam}^2(V_k) < \infty \text{ only if } |\Lambda| < \infty.$$

As the total area of the flow domain is itself finite, hence the result follows. ☐

Therefore, the finiteness of the system of vortices is indeed independent of the geometry of the flow domain. The second proof suggests that even if the flow domain is not simply connected (contains holes), still the finiteness of number of vortices is guaranteed.

NOTE:

The separation points on the solid boundary paves the way for the formation of a new vortex. But one separation point (∂-singular point) does not necessarily generate only a single vortex in general over a period of time. In fact, in the event of breakdown of vortices during vortex-shedding for flow past bluff bodies, at a particular instant of time the set of vortices generated from the same separation point is still finite. The instantaneous vortex will be attached to the solid boundary, whereas the earlier ones will be pushed into the downstream of the flow domain. The second proof of finiteness of vortices ensures the finiteness of vortices corresponding to the same separation point. So the set of all vortices in the flow domain being a finite union of finite sets, is finite.

7.3 Conclusion

The geometric theories of incompressible viscous flows as a discipline of topological fluid dynamics mainly revolve around the existence of critical points in a flow field. To the best of our knowledge, no connection of these critical points to the number of vortices in a flow field has been established so far. We provide two rigorous mathematical proofs to show that the number of vortices in an incompressible fluid flow in a finite domain is finite. For the first proof, a recently developed geometric theory of incompressible viscous flows along with an existing mathematical analysis concept has been used. The second proof adopts the Kolmogorov's length scale criterion in conjunction with the notion of diametric disks.

TH-1927_126123012

भारतीय प्रौद्योगिकी संस्थान गुवाहाटी • Indian Institute of Technology Guwahati •

Chapter 8

CONCLUDING REMARKS AND SCOPE FOR FUTURE WORKS

We sum up the thesis by highlighting its major achievements in this chapter and also throw some light on the scopes for possible future works based on the present study.

8.1 Concluding remarks

1. We compute with care and precision, the features of corner vortices in lid-driven square cavity flow, examining along the way the intensity and size ratios of successive vortices. In order to compute the flow, a recently developed efficient transient Navier–Stokes (N–S) solver is used on compact non-uniform space grids with extreme clustering at the corners. We have explored the possibility of them qualifying as Moffatt vortices for a wide range of Reynolds numbers: starting from the Stokes flow to a moderately high $Re = 3200$. The size and intensities of the corner vortices are measured and their accuracy is further strengthened by extrapolating the computed data on finer grids through Richardson's extrapolation and Lagrange interpolation. This is probably for the first time that the vortices in the 2D lid-driven cavity have been resolved and documented with extreme details up to the post-quaternary level, both qualitatively and quantitatively. As such this study is also an effort towards benchmarking the corner vortex data for the flow under consideration. We further observe that these vortices exhibit self-similarity like a fractal object does. Besides, we have introduced a novel approach to the grid independence analysis where the concept of adverse pressure gradients is used as a tool to validate that the separation zones in the neighbourhood of the corners are consistent with the vortices obtained from the computed solution. This strengthens our case that the smallest scales resulting from the computation are actual physical phenomena, not numerical artefacts.

2. All the previous studies on the lid driven cavity flow are confined to either the study of its 2D or 3D configuration in isolation. In the present study, we utilize the critical point concept from the recent advances in the topological fluid dynamics theory to gain some physical insight into the corner vortices from the perspective of the flow topology in the 2D vis a vis 3D cavity. The separation, reattachment and vortical structures in the flow were analyzed by post-processing the computed flow through the identification of the critical points. The vortical structures found in the plane of symmetry of the 3D flow have been identified as stable limit cycles. Moreover, we utilize the Poincaré-Bendixson formula to validate the computed flow in the two-dimensional cavity for the possible number of critical points present in the flow field. The typical sequence of events in terms of the critical point structures leading to the very first birth of a vortex at the corner has also been discussed in details. The topological features of the corner vortices in actual three-dimensional flow and its two-dimensional idealization in the cavity has also been compared.

3. We explore some physical insight into the vortical flow in a rectangular cavity with values of SAR (Spanwise Aspect Ratio) ($\equiv$ L : B = 2, 3), subject to a constant velocity on the lid by using rigorous theories in the field of topological fluid dynamics. For this purpose, we have computed the flow inside the cavity by solving the 3D N–S equations for $Re = 1000$ and 3200 by the commercially available software ANSYS Fluent 15.0 version on non-uniform grids on a parallel set up. We post-process the computed data to identify different form of critical points present in the flow field. The topological structures in the neighbourhood of these critical points have been explained in details. The Poincaré-Bendixson formula has been used to ensure all the critical points obtained through eigenvalue analysis are dynamically possible. Further, the topology of TGL vortices has been discussed. We observe some interesting flow structures such as U-shaped vortex structures and mushroom shaped structures which are closely associated with the formation of TGL vortices and responsible for the onset of turbulence.

4. Till date, Moffatt vortices have been characterized only through the establishment of a common ratio of their computed size and intensities. To the best of our knowledge, no rigorous mathematical characterization of these vortices with respect to their orientations is available in the existing literature. In an effort in this direction, firstly we have established two topological equivalence classes of Moffatt vortices in terms of orientation-preserving homeomorphism as well as critical point theory. We further established the centers of these vortices as fixed points through Brouwer fixed-point theorem and identified the boundary of a vortex as circle cell. The outcome of our results may become useful in describing complicated flow structures in a much simpler form in a transformed domain and prove to be an important addition to the existing geometric theories of incompressible viscous flows.

5. In the existing literature, the occurrence of Moffatt vortices has always been synonymous with the existence of an infinite sequence. Despite the continuum axiom providing the base for the governing equations for incompressible viscous flows and the concept of Kolmogorov length scale in vogue, the issue of the finiteness of such sequence has continued to remain unattended. In an effort toward addressing this issue, firstly we have listed the concerns and the pertinent questions on the notion of infiniteness of such sequences and pinpointed where the assumptions of the existing hypothesis might have gone wrong. Making use of some elementary concepts of mathematical analysis and our own construction of diametric disks, we proved that the number of vortices in solid corners in a bounded domain must be finite. Our observations are consistent with the recent developments of geometric theories of incompressible viscous flows.

6. The geometric theories of incompressible viscous flows as a discipline of topological fluid dynamics mainly revolve around the existence of critical points in a flow field. To the best of our knowledge, no connection of these critical points to the number of vortices in a flow field has been established so far. We provide two rigorous mathematical proofs to show that the number of vortices in an incompressible fluid flow in a finite domain is finite. For the first proof, a recently developed geometric theory of incompressible viscous flows along with an existing mathematical analysis concept has been used. The second proof adopts the Kolmogorov's length scale criterion in conjunction with the notion of diametric disks.

8.2 Scope for future works

The ideas developed in the thesis could lead to a host of interesting research possibilities; a brief outline of them are presented below.

(i) Whether the self-similarity of Moffatt vortices that had been observed in the driven cavity may also exist in other flow situations, could be an interesting area of research. Another possibility is the study of self-similarity of Moffatt vortices from fractal point of view with a more rigorous theoretical approach.

(ii) In reality, vortical structures are very complicated; they are not necessarily of regular shapes. The notion of smooth deformation/homeomorphism and topological equivalence allow us to study them in a much simpler form. This could open up a number of exciting research possibilities on vortical structures in different fluid flow situations.

(iii) Further studies on TGL vortices could be taken up by the structural bifurcation theory approach. Moreover, the identification of U-shaped vortex structures in the 3D lid-driven cavity for flow regimes other than the ones considered in the dissertation could be an interesting research topic. Besides, it will be worthwhile to explore the connection between λ_2 criterion and mushroom-shaped vortex structures.

(iv) Till date, no single definition of a vortex is universally accepted. The current study may pave the way for developing a novel definition of a vortex, which could be a significant contribution in the field of incompressible viscous flows.

Indian Institute of Technology Guwahati

भारतीय प्रौद्योगिकी संस्थान गुवाहाटी • Indian Institute of Technology Guwahati •

Appendices

भारतीय प्रौद्योगिकी संस्थान गुवाहाटी • Indian Institute of Technology Guwahati •

Appendix A

HOC SIMULATION OF MOFFATT EDDIES IN THE TRIANGULAR CAVITY FLOW

A.1 The problem and the governing equations

The problem considered here is that of the motion of an incompressible viscous fluid inside a triangular cavity. The cavity is in the shape of an isosceles triangle with an altitude twice the size of its base as in figure A.1 defined inside the rectangular region $(x, y) \in [0, 1] \times [0, 2]$ in the xy-plane.

The equations governing the flow inside the cavity is the famous Navier–Stokes (N–S) equations which in the conventional non-dimensional primitive variable form in steady state are given by

$$\frac{\partial u}{\partial x} + \frac{\partial v}{\partial y} = 0, \tag{A.1}$$

$$u\frac{\partial u}{\partial x} + v\frac{\partial u}{\partial y} = -\frac{\partial p}{\partial x} + \frac{1}{Re}\nabla^2 u, \tag{A.2}$$

$$u\frac{\partial v}{\partial x} + v\frac{\partial v}{\partial y} = -\frac{\partial p}{\partial y} + \frac{1}{Re}\nabla^2 v, \tag{A.3}$$

where u, v are the velocities along the x- and y- directions respectively, p is the

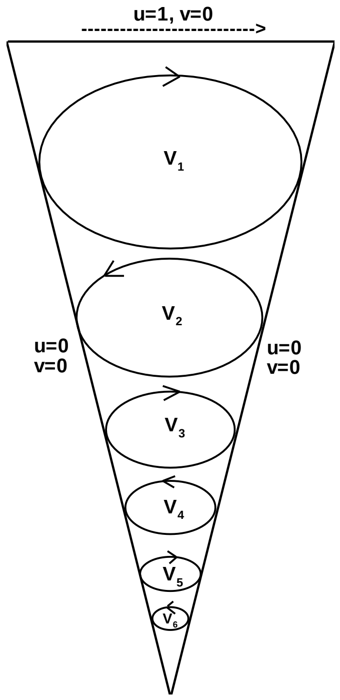

Figure A.1: *Flow configuration in the triangular cavity flow.*

pressure, Re is the Reynolds number (non-dimensional),∇^2 is the Laplacian operator and U is the wall velocity at the lid of the cavity.

Due to the presence of pressure term in the above equations (A.1-A.3), its direct solution is difficult to obtain. To overcome this difficulty, an alternative approach is to employ the streamfunction-vorticity formulation (ψ-ω) of N–S equations [146].

$$u\omega_x + v\omega_y = \frac{1}{Re}(\omega_{xx} + \omega_{yy}), \tag{A.4}$$

$$\psi_{xx} + \psi_{yy} = -\omega(x, y), \tag{A.5}$$

with

$$u = \psi_y,\ v = -\psi_x \quad \text{and} \quad \omega = v_x - u_y. \tag{A.6}$$

Although this formulation has been quite successful in computing both external and internal incompressible viscous flows, certain difficulty arises as

Indian Institute of Technology Guwahati

vorticity values along the no-slip boundaries are not specified. Consequently, one needs to look for special measures for obtaining vorticity at the boundaries.

In order to avoid all such difficulties stated above, another alternative formulation can be obtained by the elimination of vorticity term in the (ψ-ω) formulation yields a fourth-order partial differential equation:

$$\Delta^2\psi - Re(v\nabla^2 u - u\nabla^2 v) = 0, \tag{A.7}$$

with (A.6), where

$$\Delta^2\psi = \frac{\partial^4\psi}{\partial x^4} + 2\frac{\partial^4\psi}{\partial x^2\partial y^2} + \frac{\partial^4\psi}{\partial y^4}. \tag{A.8}$$

By utilizing the equations (A.6) and (A.8), the equation (A.7) results in the following form:

$$\frac{\partial^4\psi}{\partial x^4}+2\frac{\partial^4\psi}{\partial x^2\partial y^2}+\frac{\partial^4\psi}{\partial y^4}-Re\left(\frac{\partial^3\psi}{\partial x^3}+\frac{\partial^3\psi}{\partial x\partial y^2}\right)u-Re\left(\frac{\partial^3\psi}{\partial y^3}+\frac{\partial^3\psi}{\partial x^2\partial y}\right)v = 0. \tag{A.9}$$

The above form (A.9) is known as the streamfunction-velocity formulation or biharmonic formulation of the N–S equations in 2D set up. The major advantages of this formulation have been discussed by Kalita and Gogoi [79].

The rationale behind choosing the above formulation for identifying Moffatt eddies in the triangular cavity is that the origin of these vortices lie in the theoretical studies on Stokes flow governed by the biharmonic form of N–S equations.

In the triangular cavity under consideration (refer to figure A.1 again), all the walls are immobile except the top one in which the non-dimensional x-velocity equals to the wall velocity $u = U = 1.0$ has been specified. On the immobile walls x- and y- velocities must be zero due to the presence of no-slip condition. Due to the motion of the top lid, the fluid in contact with it is set into motion and evolves in the interior of the cavity. The typical flow structure is depicted in figure A.1 where one can see a sequence of vortices is generated inside the cavity starting from the ones bigger in size and strength at the top, each one driving the next smaller one and the process continues.

A.2 Numerical procedures

A.2.1 The scheme used

The recently developed second order compact scheme by Gupta and Kalita [53] has been used to discretize the equation of the form (A.9). In the following, we briefly discuss about their scheme. The aforementioned compact formulation for the 2D steady state N–S equations in biharmonic form is given by

$$\begin{aligned}
&\psi_{i-1,j-1} - 8\psi_{i,j-1} + \psi_{i-1,j} - 8\psi_{i-1,j} + 28\psi_{i,j} - 8\psi_{i+1,j} + \psi_{i-1,j+1} \\
&-8\psi_{i,j+1} + \psi_{i+1,j+1} - 3h(u_{i,j-1} - u_{i,j+1} + v_{i+1,j} - v_{i-1,j}) - 0.5h^2 Re \\
&\{v_{i,j}(u_{i+1,j} + u_{i-1,j} + u_{i,j+1} + u_{i,j-1}) - u_{i,j}(v_{i+1,j} + v_{i-1,j} + v_{i,j+1} \\
&+v_{i,j-1})\} = 0 \qquad \text{(A.10)}
\end{aligned}$$

where, h represents step-length on a uniform grid in both x- and y-directions.

The fourth-order central difference formula has been used to approximate the velocities u and v in (A.6) yields the following formulas:

$$u_{i,j} = \frac{3}{4h}(\psi_{i,j+1} - \psi_{i,j-1}) - \frac{1}{4}(u_{i,j+1} + u_{i,j-1}), \qquad \text{(A.11)}$$

$$v_{i,j} = -\frac{3}{4h}(\psi_{i+1,j} - \psi_{i-1,j}) - \frac{1}{4}(v_{i+1,j} + v_{i-1,j}). \qquad \text{(A.12)}$$

A.2.2 Associated algebraic systems and its solution

The algebraic system of equations associated with the compact finite difference scheme (A.10) can be written as the following matrix equation:

$$M\boldsymbol{\Psi} = \boldsymbol{f}(\psi, u, v) \qquad \text{(A.13)}$$

where, M is an asymmetric sparse matrix having dimension mn for a grid of size $m \times n$; $\boldsymbol{\Psi}$ and $\boldsymbol{f}$ are mn-component vectors. An outer-inner iteration strategy has been employed in order to solve this problem. We solve the equation (A.13) in the outer iteration cycle by using the biconjugate gradient stabilized method (BiCGStab) [81, 124] without any preconditioning which constitutes inner iteration cycle. We have used a relaxation parameter $\mu = 0.95$ inside both the outer and inner iteration cycles for ψ. All of our computations were carried out on on a Intel Core i5 based PC with 3GB RAM. The computations were continued untill the maximum ψ-error between two consecutive outer iteration steps fell bellow 0.5×10^{-9}.

A.2.3 Strategy for boundary conditions

In the domain $(x, y) \in [0, 1] \times [0, 2]$, we choose the left and right boundary of the triangular cavity in such a way that both the lines corresponding to these boundaries must pass through the available grid points in the computational domain. The boundary conditions for the top wall of the cavity are specified as $u = 1,\ v = 0$. For other two boundaries the following strategy has been adopted while imposing the boundary conditions as $u = 0,\ v = 0$ in the computational domain.

For the left boundary: $u_{i,j} = v_{i,j} = 0$ in which $0 \leq i < (m-1)/2$, $1 \leq j < n-1$ if $i < \{(m-1)/2 - j/4\}$, where $i,\ j$ stand for x-direction index and y-direction index respectively. In a similar manner, for the right boundary: $u_{i,j} = v_{i,j} = 0$ in which $(m-1)/2 \leq i < m-1$, $1 \leq j < n-1$ if $i > \{(m-1)/2 + j/4\}$. In the above, m and n represent maximum number of grid points along x- and y-direction respectively. For the streamfunction-velocity formulation, streamfunction values are set to be zero i.e, $\psi = 0$ along all the three boundaries of the cavity.

A.3 Numerical results

The flow in the triangular cavity has been computed on three different space grids of sizes 129×257, 257×513 and 513×1025. However, we present the result obtained from the finer grid only. The through investigation of literature reveals the study of Moffatt eddies mainly confined at very low *Re*. Keeping this in mind, we choose *Re* to be of value 1 in our numerical computation.

In figure A.2(a), we depict the presence of Moffatt eddies in the triangular cavity. These eddies are stacked from top to bottom in a cascade to the tip.

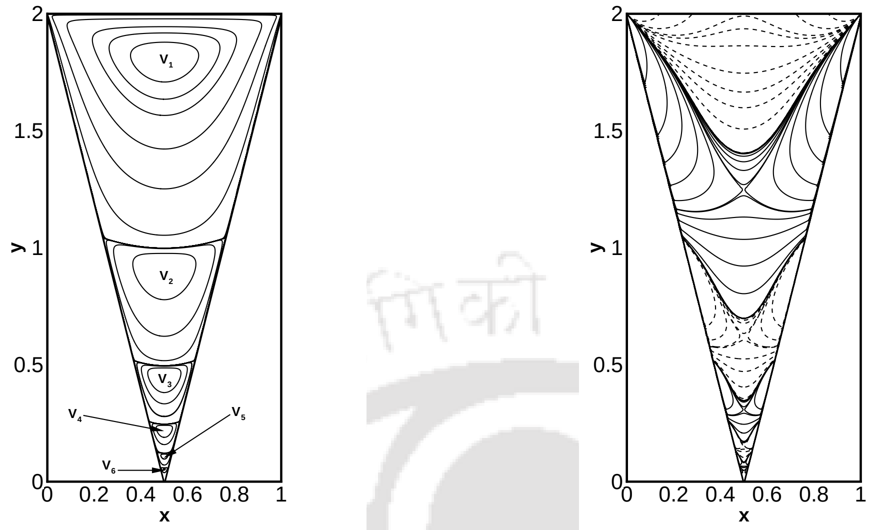

(a) (b)

Figure A.2: *(a) Evidence of Moffatt vortices and (b) vorticity distribution in the triangular cavity on grid of size* 513×1025*.*

We present them by streamfunction contours and the following nomenclature has been adopted V_1, V_2, $V_3 \cdots$, to mark them to in the sequence sequence as approach to the bottom stationary corner of the cavity. From our computation, we are able to trace six members from the sequence of Moffatt eddies. We compare our results with the only experimental result by Taneda [140] available in the existing literature which shows an excellent matching (see figure 5.1 of chapter 5).

In table A.1, we present the center location, intensity and size of each member in the sequence of Moffatt eddies. The intensity of an eddy is measured by the streamfunction value at its center and size by the vertical distance between its center and tip of the cavity. We observe that the intensity value and size of these eddies decreases rapidly as approaches towards the corner. Moreover, the eddies in the sequence fall off a geometric progression having fixed common ratio for both the size and intensity. From our computation, we determine the common ratio of size (S_R) and intensity (I_R) as

$$S_R\left(\frac{V_{n+1}}{V_n}\right) \approx 0.0012 \quad \text{and} \quad I_R\left(\frac{V_{n+1}}{V_n}\right) \approx 0.49,$$

where, $n = 1,\ 2,\ \cdots, 5$ (For further details see table A.2). All these facts are in accordance with the prediction of the theory of Moffatt [106, 107].

Table A.1: *Details of Moffatt eddies in the triangular cavity for* $Re = 1$ *on grid of size* 513×1025.

Vortex	**Intensity**	**Center Location**	**Size**
V_1	-8.4783 $\times 10^{-1}$	(0.5000, 1.8027)	1.8027
V_2	1.1159 $\times 10^{-4}$	(0.5000, 0.9063)	0.9063
V_3	-1.3625 $\times 10^{-7}$	(0.5000, 0.4492)	0.4492
V_4	1.6687 $\times 10^{-10}$	(0.5000, 0.2227)	0.2227
V_5	-2.0694 $\times 10^{-13}$	(0.5000, 0.1094)	0.1094
V_6	2.6748 $\times 10^{-16}$	(0.5000, 0.0547)	0.0547

Table A.2: *Intensity and size ratio between two eddies in succession.*

Eddy Ratio	**Intensity**	**Size**
$V_2 : V_1$	0.001316	0.502709
$V_3 : V_2$	0.001221	0.495696
$V_4 : V_3$	0.001224	0.495692
$V_5 : V_4$	0.001240	0.491468
$V_6 : V_5$	0.001292	0.499634

In figure A.2(b), we present the contour plot of constant vorticity which is defined by $\omega = v_x - u_y$ for $Re = 1$. We observe that the vorticity field in the cavity is symmetric about the vertical centerline. It is heartening to note that the characteristics of sequence of eddies and their distribution in the cavity were again in accordance with the analytical predictions of Moffatt [106, 107].

भारतीय प्रौद्योगिकी संस्थान गुवाहाटी • Indian Institute of Technology Guwahati •

Appendix B

A NOTE ON USING KOLMOGOROV LENGTH SCALE

In a recent note [133] on the current work published in [74], Shtern raised some doubts on using the Kolmogorov length scale in our proof of finiteness. We thought it appropriate to rope in some of the comments made in [73] in this context in the following.

Note that the very definition of vortex requires [60] the rotational effect in the immediate neighbourhood of the vortex center. As such the circulation [12, 146] of the vortex must be non-zero. On the other hand, a vortex with zero length scale will naturally render a zero circulation for a vortex and hence would fail to satisfy the definition of a vortex. Therefore the smallest length scale that can be accommodated in the so-called infinite sequence of vortices must be non-zero, even if smaller than the Kolomogorov length scale. This scale was used in the main proofs on finiteness in chapter 6 to signify a non-zero length scale only. Any such length scale (referred to as η in section 6.2.3.1), be it Kolmogorov or anything else, is sufficient to ensure the finiteness. Thus the claim (in [133]) that the notion of finiteness "is not even heuristically valid if there are geometric length scales which are smaller than the Kolmogorov scale" is an invalid one.

The above brings us to another point raised in [133], that the current study has not offered or referred to any proof of the statement "A vortex scale cannot be smaller than Kolmogorov length scale". A close examination of the current dissertation and [74] would reveal that no such statement was made thereat; rather we had stated that "the Kolmogorov theory [145] asserts that eddies below a certain size cannot be formed." However, Shtern [133] avoids making any comments on the justification provided in the last paragrpah of section 6.2.3.1 pertaining to Kolmogorov length scale. Under the same geometric configuration, for a flow undergoing laminar to turbulent transition, can the smallest possible laminar scale be smaller than the smallest turbulent scale defined by the Kolmogorov scale? The answer is a clear no, which comes from experimental and numerical evidences. For example, the visualization of flow past bluff bodies at high Reynolds numbers, where the flow is laminar just behind the body initially and becomes turbulent in the downstream region away from the body later on (see the visualizations in [39, 149, 150], chapter 7 of [146] chapters 5, 6 of [147]). Another example in this context is the visualization of flows arising out of plane jets at different Reylonds numbers depicting the laminar and turbulent regimes [138, 141]. Just behind the jets, the turbulent length scales are much smaller than the laminar ones here. Recall that the concept of the Kolmogorov length scale comes from the cascading effect where energy is transferred from larger to smaller eddies. Laminar eddies are not small enough to accommodate the mixing of the eddies to facilitate the transfer of energy [147].

Bibliography

[1] http://www.ssisc.org/lis, 2013.

[2] P. S. Addison. *Fractals and Chaos: An Illustrative Course.* IOP Publishing, Bristol, UK, 1997.

[3] C. K. Aidun, N. G. Triantafillopoulos, and J. D. Benson. Global stability of a lid-driven cavity with throughflow:Flow visualization studies. *Physics of Fluids A*, 3(9):2081–2091, 1991.

[4] S. Albensoeder and H. C. Kuhlmann. Accurate three-dimensional lid-driven cavity flow. *Journal of Computational Physics*, 206:536–558, 2005.

[5] D. M. Anderson and S. H. Davis. Two-fluid viscous flow in a corner. *Journal of Fluid Mechanics*, 257:1–31, 1993.

[6] B. Andersson, R. Andersson, L. Hakansson, M. Mortensen, R. Sudiyo, and B.V. Wachem. *Computational Fluid Dynamics for Engineers.* Cambridge University Press, Cambridge, UK, 2012.

[7] A. A. Andronov, E. A. Leontovich, I. I. Gordon, and A. G. Maier. *Qualitative Theory of Second-Order Dynamical Systems.* Wiley, New York, 1973.

[8] M. A. Armstrong. *Basic Topology.* Springer, New York, 1983.

[9] P. G. Bakker. *Bifurcations in Flow Patterns.* PhD thesis, Netherlands, 1989.

[10] D. C. Banks and B. A. Singer. Vortex tubes in turbulent flows: Identification, representation, reconstruction. *In Proceedings of the conference of Visualization, IEEE Computer Society Press*, pages 132–139, 1994.

[11] M. F. Barnsley. *Fractals Everywhere.* Academic Press, London, UK, 1993.

[12] G. K. Batchelor. *An Introduction to Fluid Dynamics.* Cambridge University Press, Cambridge, UK, 1993.

[13] B. J. Bellhouse and L. Talbot. The fluid mechanics of the aortic valve. *Journal of Fluid Mechanics*, 35(4):721–735, 1969.

[14] D. ben Avraham and S. Havlin. *Diffusion and Reactions in Fractals and Disordered Systems.* Cambridge University Press, Cambridge, UK, 2000.

[15] G. Biswas, M. Breuer, and F. Drust. Backward-facing step flows for various expansion ratios at low and moderate Reynolds numbers. *Journal of Fluids Engineering: Transactions of the ASME*, 126 (3):362–374, 2004.

[16] S. Biswas and J. C. Kalita. Moffatt vortices in the lid-driven cavity flow. *Journal of Physics: Conference Series*, 759:012081, 2016.

[17] S. Biswas and J. C. Kalita. Moffatt eddies in the driven cavity: A quantification study by an HOC approach. *Computers and Mathematics with Applications*, 76(3):471–487, 2018.

[18] R. Bouard and M. Coutanceau. The early stage of development of the wake behind an impulsively started cylinder for $40 < Re < 10^4$. *Journal of Fluid Mechanics*, 101(3):583–607, 1980.

[19] M. Branicki and H. K. Moffatt. Evolving eddy structures in oscillatory Stokes flows in domains with sharp corners. *Journal of Fluid Mechanics*, 551:63–92, 2006.

[20] M. J. Braun, F. K. Choy, and Y. M. Zhou. The effects of a hydrostatic pocket aspect ratio, supply orifice position, and attack angle on steady-state flow patterns, pressure, and shear characteristics. *ASME Journal of Tribology*, 115(4):678–685, 1993.

[21] F. P. Bretherton. Resonant interactions between waves. The case of discrete oscillations. *Journal of Fluid Mechanics*, 20 (3):457–469, 1964.

[22] C. H. Bruneau and M. Saad. The 2D lid-driven cavity problem revisited. *Computers and Fluids*, 35 (3):326–348, 2006.

[23] R. L. Burden and J. D. Faires. *Numerical Analysis*. Brooks/Cole, Cengage Learning, Boston, USA, 2011.

[24] O. R. Burggraf. Analytical and numerical studies of the structure of steady separated flows. *Journal of Fluid Mechanics*, 24 (1):113–151, 1966.

[25] M. P. Do Carmo. *Differential Geometry of Curves and Surfaces*. Prentice-Hall, Inc., Englewood Cliffs, New Jersey, 1976.

[26] P. Chakraborty, S. Balachandar, and R. J. Adrian. On the relationships between local vortex identification schemes. *Journal of Fluid Mechanics*, 535:189–214, 2005.

[27] T. P. Chiang, R. R. Hwang, and W. H. Sheu. On end-wall corner vortices in a lid-driven cavity. *Journal of Fluids Engineering: Transactions of the ASME*, 119:201–204, 1997.

[28] T. P. Chiang and W. H. Sheu. Numerical prediction of eddy structure in a shear-driven cavity. *Computational Mechanics*, 20:379–396, 1997.

[29] T. P. Chiang, W. H. Sheu, and R. R. Hwang. Three-dimensional vortex dynamics in a shear-driven rectangular cavity. *International Journal of Computational Fluid Dynamics*, 8:201–214, 1997.

[30] W. M. Collins and S. C. R. Dennis. Viscous eddies near a 90° and a 45° corner in flow through a curved tube of triangular cross-section. *Journal of Fluid Mechanics*, 76 (3):417–432, 1976.

[31] A. B. Cortes and J. D. Miller. Numerical experiments with the lid-driven cavity flow problem. *Computers and Fluids*, 23(8):1005–1027, 1994.

[32] M. Coutanceau and R. Bouard. Experimental determination of the main features of the viscous flow in the wake of a circular cylinder in uniform translation. Part 1. Steady flow. *Journal of Fluid Mechanics*, 79(2):231–256, 1977.

[33] M. Coutanceau and R. Bouard. Experimental determination of the main features of the viscous flow in the wake of a circular cylinder in uniform translation. Part 2. Unsteady flow. *Journal of Fluid Mechanics*, 79(2):257–272, 1977.

[34] G. de Vahl Davis and G. D. Mallinson. An evaluation of upwind and central difference approximations by a study of recirculating flow. *Computers and Fluids*, 4(1):29–43, 1976.

[35] W. R. Dean and P. E. Montagnon. On the steady motion of viscous liquid in a corner. *Mathematical Proceedings of the Cambridge Philosophical Society*, 45 (3):389–395, 1949.

[36] J. Délery. *Three-Dimensional Separated Flow Topology.* ISTE Ltd and John Wiley and Sons, Inc., London, UK, 2013.

[37] M. D. Deshpande and S. G. Milton. Kolmogorov scales in a driven cavity flow. *Fluid Dynamics Research*, 22 (6):359–381, 1998.

[38] M. Deville, T H. Lê, and Y. Morchoisne. Numerical simulation of 3-D incompressible unsteady viscous laminar flows. *In: Notes on Numerical Fluid Mechanics, A GAMM-Workshop*, 36:73–89, 1992.

[39] M. V. Dyke. *An Album of Fluid Motion.* The Parabolic Press, Stanford, USA, 1982.

[40] E. Erturk and O. Gokcol. Fine grid numerical solutions of triangular cavity flow. *The European Physics Journal Applied Physics*, 38:97–105, 2007.

[41] E. Erturk, T. C. Korke, and G. Gökcöl. Numerical solutions of 2-D steady incompressible driven cavity flow at high Reynolds numbers. *International Journal for Numerical Methods in Fluids*, 48 (7):747–774, 2005.

[42] H. Fellouah, C. Castelain, O. E. Moctar, and H. Peerhossaini. A numerical study of Dean instability in Non-Newtonian fluids. *Journal of Fluids Engineering: Transactions of the ASME*, 128 (1):34–41, 2005.

[43] E. Flapan. *When Topology Meets Chemistry: A Topological Look at Molecular Chirality*. Cambridge University Press, Cambridge, UK, 2000.

[44] C. J. Freitas and R. L. Street. Non-linear transport phenomena in a complex recirculating flow: A numerical investigation. *International Journal of Numerical Methods in Fluids*, 8:769–802, 1988.

[45] C. J. Freitas, R. L. Street, A. N. Findikakis, and J. R. Koseff. Numerical simulation of three-dimensional flow in a cavity. *International Journal of Numerical Methods in Fluids*, 5:561–575, 1985.

[46] U. Frisch. *Turbulence: The legacy of A. N. Kolmogorov*. Cambridge University Press, Cambridge, UK, 1995.

[47] P. H. Gaskell, J. L. Summers, H. M. Thompson, and M. D. Savage. Creeping flow analyses of free surface cavity flows. *Theoretical and Computational Fluid Dynamics*, 8(6):415—433, 1996.

[48] U. Ghia, K. N. Ghia, and C. T. Shin. High-*Re* solutions for incompressible flow using the Navier-Stokes equations and a multigrid method. *Journal of Computational Physics*, 48 (3):387–411, 1982.

[49] M. Ghil, J. G. Liu, C. Wang, and S. Wang. Boundary-layer separation and adverse pressure gradient for 2-D viscous incompressible flow. *Physica D*, 197:149–173, 2004.

[50] R. Glowinski, G. Guidoboni, and T. W. Pan. Wall-driven incompressible viscous flow in a two-dimensional semi-circular cavity. *Journal of Computational Physics*, 216:76–91, 2006.

[51] J. L. Guermond, C. Migeon, G. Pineau, and L. Quartapelle. Start-up flows in a three-dimensional rectangular driven cavity of aspect ratio $1:1:2$ at $Re = 1000$. *Journal of Fluid Mechanics*, 450:169–199, 2002.

[52] V. Guillemin and A. Pollack. *Differential Topology.* Prentice-Hall, Inc., Englewood Cliffs, New Jersey, 1974.

[53] M. M. Gupta and J. C. Kalita. A new paradigm approach for solving Navier-Stokes equations: streamfunction-velocity formulation. *Journal of Computational Physics*, 207:52–68, 2005.

[54] M. M. Gupta, R. P. Manohar, and B. Noble. Nature of viscous flows near sharp corners. *Computers and Fluids*, 9:379–388, 1981.

[55] K. Gustafson, K. Halasi, and R. Leben. Controversies concerning finite/infinite sequences of fluid corner vortices. *Contemporary Mathematics, American Mathematical Society*, 99:351–357, 1989.

[56] K. Gustafson and R. Leben. Mutigrid calculations of subvortices. *Applied Mathematics and Computation*, 19:89–102, 1986.

[57] K. Gustafson and R. Leben. Vortex subdomains. 1^{st} *International Symposium on Domain Decomposition methods for Partial Differential Equations, Paris, France*, 1987.

[58] K. Gustafson and J. A. Sethian. *Vortex Methods and Vortex Motion.* SIAM Publications, Philadelphia, PA, 1991.

[59] O. Hall, C. P. Hills, and A. D. Gilbert. Slow flow between concentric cones. *Quarterly Journal of Mechanics and Applied Mathematics*, 60 (1):27–48, 2007.

[60] G. Haller. An objective definition of a vortex. *Journal of Fluid Mechanics*, 525:1–26, 2005.

[61] M. Hellou and M. Coutanceau. Cellular stokes flow induced by rotation of a cylinder in a closed channel. *Journal of Fluid Mechanics*, 236:557–577, 1992.

[62] E. H. Hirschel, J. Cousteix, and W. Kordulla. *Three-Dimensional Attached Viscous Flow.* Springer-Verlag, Heidelberg, Germany, 2014.

[63] J. D. Hoffmann. *Numerical Methods for Engineers and Scientists.* Marcel Dekker Inc., New York, USA, 2001.

[64] Z. Huang, J. A. Olson, R. J. Kerekes, and S. I. Green. Numerical simulation of the flow around rows of cylinders. *Computers and Fluids*, 35 (5):485–491, 2006.

[65] J. C. R. Hunt, C. J. Abell, J. A. Peterka, and H. Woo. Kinematical studies of the flows around free or surface-mounted obstacles; applying topology to flow visualization. *Journal of Fluid Mechanics*, 86 (1):179–200, 1978.

[66] R. Iwatsu, K. Ishii, T. Kawamura, K. Kuwahara, and J. M. Hyun. Numerical simulation of three-dimensional flow structure in a driven cavity. *Fluid Dynamics Research*, 5(3):173–189, 1989.

[67] J. Jeong and F. Hussain. On the identification of a vortex. *Journal of Fluid Mechanics*, 285:69–94, 1995.

[68] J. Jiménez. The contributions of A. N. Kolmogorov to the theory of turbulence. *Arbor CLXXVIII*, 178 (704):589–606, 2004.

[69] D. W. Jordon and P. Smith. *Nonlinear Ordinary Differential Equations*. Oxford University Press Inc., New York, Fourth Edition, 2007.

[70] R. Jyotsna and S. P. Vanka. Multigrid calculation of steady, viscous flow in a triangular cavity. *Journal of Computational Physics*, 122:107–117, 1995.

[71] J. C. Kalita. Effects of clustering on the simulation of incompressible viscous flows. *Engineering Applications of Computational Fluid Mechanics*, 1 (1):36–48, 2007.

[72] J. C. Kalita. A super-compact higher order scheme for the unsteady 3D incompressible viscous flows. *Computational and Applied Mathematics*, 33:717–738, 2014.

[73] J. C. Kalita. Comments on “Comment on “Finiteness of corner vortices” [Z. Angew. Math. Phys. (2018) 69:37]”[Z. Angew. Math. Phys. (2018) 69:64] . *arXiv:1807.00200*, 2018.

[74] J. C. Kalita, S. Biswas, and S. Panda. Finiteness of corner vortices. *Zeitschrift für angewandte Mathematik und Physik*, 69:37, 2018.

[75] J. C. Kalita, D. C. Dalal, and A. K. Dass. Fully compact higher order computation of steady-state natural convection in a square cavity. *Physical Review E*, 64:1–13, 2001.

[76] J. C. Kalita, D. C. Dalal, and A. K. Dass. A class of higher order compact schemes for the unsteady two-dimensional convection-diffusion equation with variable convection coefficients. *International Journal for Numerical Methods in Fluids*, 38:1111–1131, 2002.

[77] J. C. Kalita, A. K. Dass, and D. C. Dalal. A transformation-free hoc scheme for steady convection-diffusion on nonuniform grids. *International Journal for Numerical Methods in Fluids*, 44:33–53, 2004.

[78] J. C. Kalita, A. K. Dass, and N. Nidhi. An efficient transient Navier-Stokes solver on compact nonuniform space grids. *Journal of Computational and Applied Mathematics*, 214 (1):148–162, 2008.

[79] J. C. Kalita and B. B. Gogoi. A biharmonic approach for the global stability analysis of 2D incompressible viscous flows. *Applied Mathematical Modelling*, 40:6831–6849, 2016.

[80] J. C. Kalita and S. Sen. Unsteady separation leading to secondary and tertiary vortex dynamics: the sub-α- and sub-β-phenomena. *Journal of Fluid Mechanics*, 730:19–51, 2013.

[81] C. T. Kelley. *Iterative Methods for Linear and Nonlinear Equations*. SIAM Publications, Philadelphia, PA, 1995.

[82] E. Kirkinis and S. H. Davis. Moffatt vortices induced by the motion of a contact line. *Journal of Fluid Mechanics*, 746:R3, 2014.

[83] J. R. Koseff and R. L. Street. The lid-driven cavity flow: a synthesis of qualitative and quantitative observations. *Journal of Fluids Engineering: Transactions of the ASME*, 106 (4):390–398, 1984.

[84] J. R. Koseff and R. L. Street. On end wall effects in a lid-driven cavity flow. *Journal of Fluids Engineering: Transactions of the ASME*, 106 (4):385–389, 1984.

[85] J. R. Koseff and R. L. Street. Visualization studies of a shear driven three-dimensional recirculating flow. *Journal of Fluids Engineering: Transactions of the ASME*, 106 (1):21–27, 1984.

[86] T. S. Krasnopolskaya. Two-dimensional Stokes flow near a corner in a right angle wedge and Moffatt's eddies. *Mechanics Research Communications*, 22:9–14, 1995.

[87] T. S. Krasnopolskaya, V. V. Meleshko, G. W. M. Peters, and H. E. H. Meijer. Steady Stokes flow in an annular cavity. *The Quarterly Journal of Mechanics and Applied Mathematics*, 49:593–619, 1996.

[88] H. C. Ku, R. S Hirsh, and T. D Taylor. A pseudospectral method for solution of the three-dimensional incompressible Navier-Stokes equations. *Journal of Computational Physics*, 70(2):439–462, 1987.

[89] D. Küchemann. Report on the IUTAM Symposium on concentrated vortex motion in fluids. *Journal of Fluid Mechanics*, 21 (1):1–20, 1965.

[90] Y. H. Kuo, K. L. Wong, and J. C.-F. Wong. Investigation of Taylor-Görtler-like vortices using the parallel consistent splitting scheme. *Advances in Applied Mathematics and Mechanics*, 1:799–815, 2009.

[91] R. Larson. *Elementary Linear Algebra*. Cengage Learning, Boston, USA, 2017.

[92] M. Lesieur. *Turbulence in Fluids*. Springer, The Netherlands, 2001.

[93] N. Liron and J. R. Blake. Existence of viscous eddies near boundaries. *Journal of Fluid Mechanics*, 107:109–129, 1981.

[94] C. Liu, L. Chen, P. Lu, and X. Liu. Study on multiple ring-like vortex formation and small vortex generation in late flow transition on a flat plate. *Theoretical and Computational Fluid Dynamics*, 27:41–70, 2013.

[95] D. Lohse and K. Q. Xia. Small-scale properties of turbulent Rayleigh–Bénard convection. *Annual Review of Fluid Mechanics*, 42:335–364, 2010.

[96] T. Ma and S. Wang. Structure of 2D incompressible flows with the dirichlet boundary conditions. *Discrete and Continuous Dynamical Systems-Series B*, 1 (1):29–41, 2001.

[97] T. Ma and S. Wang. *Geometric Theory of Incompressible Flows with Applications to Fluid Dynamics*. American Mathematical Society, Rhode Island, USA, 2005.

[98] J. P. P. Magalhães, D. M. S. Albuquerque, J. M. C. Pereira, and J. C. F. Pereira. Adaptive mesh finite-volume calculation of 2D lid-cavity corner vortices. *Journal of Computational Physics*, 243:365–381, 2013.

[99] C. P. Malhotra, P. D. Weidman, and A. M. J. Davis. Nested toroidal vortices between concentric cones. *Journal of Fluid Mechanics*, 522:117–139, 2005.

[100] V. S. Malyuga. Viscous eddies in a circular cone. *Journal of Fluid Mechanics*, 522:101–116, 2005.

[101] W. S. Massey. *Algebraic Topology: An Introduction*. Springer, New York, 1967.

[102] R. McLachlan. A steady separated viscous corner flow. *Journal of Fluid Mechanics*, 231:1–34, 1991.

[103] C. Migeon. Details on the start-up development of the Taylor-Görtler-like vortices inside a square-section lid-driven cavity for $1000 \leq Re \leq 3200$. *Experiments in Fluids*, 33(4):594–602, 2002.

[104] P. K. Mishra, A. K. De, M. K. Verma, and V. Eswaran. Dynamics of reorientations and reversals of large-scale flow in Rayleigh–Bénard convection. *Journal of Fluid Mechanics*, 668:480–499, 2011.

[105] P. K. Mishra and M. K. Verma. Energy spectra and fluxes for Rayleigh–Bénard convection. *Physical Review E*, 81:056316, 2010.

[106] H. K. Moffatt. Viscous and resistive eddies near a sharp corner. *Journal of Fluid Mechanics*, 18 (1):1–18, 1964.

[107] H. K. Moffatt. Viscous eddies near a sharp corner. *Archiwum Mechaniki Stosowanej*, 16 (2):365–372, 1964.

[108] H. K. Moffatt. The asymptotic behaviour of solutions of the Navier-Stokes equations near sharp corners. *Lecture Notes in Mathematics, Springer*, 771:371–380, 1979.

[109] H. K. Moffatt and B. R. Duffy. Local similarity solutions and their limitations. *Journal of Fluid Mechanics*, 96 (2):299–313, 1980.

[110] H. K. Moffatt, S. Kida, and K. Ohkitani. Stretched vortices – the sinews of turbulence; large-Reynolds-number asymptotics. *Journal of Fluid Mechanics*, 259:241–264, 1994.

[111] Z. Neufeld and E. H-Garcı́a. *Chemical and Biological Processes in Fluid Flows: A Dynamical Systems Approach.* Imperial College Press, London, UK, 2010.

[112] A. V. Obabko and K. W. Cassel. Navier-Stokes solutions of unsteady separation induced by a vortex. *Journal of Fluid Mechanics*, 465:99–130, 2002.

[113] M. E. O'Neill. On angles of separation in Stokes flows. *Journal of Fluid Mechanics*, 133:427–442, 1983.

[114] F. Pan and A. Acrivos. Steady flows in rectangular cavities. *Journal of Fluid Mechanics*, 28(4):643–665, 1967.

[115] T. C. Papanastasiou, G. C. Georgiou, and A. N. Alexandrou. *Viscous Fluid Flow.* CRC Press, Washington, D.C., USA, 1999.

[116] L. R. Pastur, Y. Fraigneau, F. Lusseyran, and J. Basely. From linear stability analysis to three-dimensional organisation in an incompressible open cavity flow. *arXiv:1207.6576*, 2012.

[117] S. V. Patankar and D. B. Spalding. A calculation procedure for heat, mass and momentum transfer in three-dimensional parabolic flows. *International Journal of Heat and Mass Transfer*, 15:1787–1806, 1972.

[118] L. Perko. *Differential Equations and Dynamical Systems*. Springer, New York, 2001.

[119] A. E. Perry and M. S. Chong. A description of eddying motions and flow patterns using critical-point concepts. *Annual Review of Fluid Mechanics*, 19:125–155, 1987.

[120] S. B. Pope. *Turbulent Flows*. Cambridge University Press, Cambridge, UK, 2000.

[121] C. Pozrikidis. Creeping flow in two-dimensional channels. *Journal of Fluid Mechanics*, 180:495–514, 1987.

[122] R. L. Ricca. *An Introduction to the Geometry and Topology of Fluid Flows*. Springer, New York, 2001.

[123] W. Rudin. *Principles of Mathematical Analysis*. McGRAW-HILL, New Delhi, India, 1976.

[124] Y. Saad. *Iterative methods for sparse linear systems*. PWS Publishing Company, 1996.

[125] M. Sahin and R. G. Owens. A novel fully implicit finite volume method applied to the lid-driven cavity problem–Part I: High Reynolds number flow calculations. *International Journal for Numerical Methods in Fluids*, 42:57–77, 2003.

[126] C. N. Savvides and J. H. Gerrard. Numerical analysis of the flow through a corrugated tube with application to arterial prostheses. *Journal of Fluid Mechanics*, 138:129–160, 1984.

[127] W. R. Sears. The boundary layer of yawed cylinders. *Journal of the Aeronautical Sciences*, 15:49–52, 1948.

[128] P. N. Shankar. The eddy structure in Stokes flow in a cavity. *Journal of Fluid Mechanics*, 250:371–383, 1993.

[129] P. N. Shankar. Moffatt eddies in the cone. *Journal of Fluid Mechanics*, 539:113–135, 2005.

[130] P. N. Shankar and M. D. Deshpande. Fluid mechanics in the driven cavity. *Annual Review of Fluid Mechanics*, 32 (1):93–136, 2000.

[131] T. W. H. Sheu and S. F. Tsai. Flow topology in a steady three-dimensional lid-driven cavity. *Computers and Fluids*, 31:911–934, 2002.

[132] V. Shtern. Moffatt eddies at an interface. *Theoretical and Computational Fluid Dynamics*, 28:651–656, 2014.

[133] V. Shtern. Comment on “Finiteness of corner vortices” [Z. Angew. Math. Phys. (2018) 69:37] . *Zeitschrift für angewandte Mathematik und Physik*, 69:64, 2018.

[134] B. A. Singer and R. D. Joslin. Metamorphosis of a hairpin vortex into a young turbulent spot. *Physics of Fluids*, 6(11):3724–3736, 1994.

[135] R. G. Sousa, R. J. Poole, A. M. Afonso, F. T. Pinho, P. J. Oliveira, A. Morozov, and M. A. Alves. Lid-driven cavity flow of viscoelastic liquids. *Journal of Non-Newtonian Fluid Mechanics*, 234:129–138, 2016.

[136] A. Surana, O. Grunberg, and G. Haller. Exact theory of three-dimensional flow separation. Part 1. Steady separation. *Journal of Fluid Mechanics*, 564 (10):57–103, 2006.

[137] A. Surana, G. B. Jacobs, and G. Haller. Extraction of separation and attachment surfaces from three-dimensional steady shear flows. *AIAA Journal*, 45(6):1290–1302, 2007.

[138] P. R. Suresh, K. Srinivasan, T. Sundararajan, and S. K. Das. Reynolds number dependence of plane jet development in the transitional regime. *Physics of Fluids*, 20:044105 (1–12), 2008.

[139] T. Taha and Z. F. Cui. CFD modelling of slug flow in vertical tubes. *Chemical Engineering Science*, 61 (2):676–687, 2006.

[140] S. Taneda. Visualization of separating Stokes flows. *Journal of the Physical Society of Japan*, 46:1935–1942, 1979.

[141] H. Tennekes and J. L. Lumley. *A First Course in Turbulence*. The MIT Press, Cambridge, Massachusetts, USA, 1972.

[142] M. Tobak and D. J. Peake. Topology of three dimensional separated flows. *Annual Review of Fluid Mechanics*, 14:61–85, 1982.

[143] D. J. Tritton. Experiments on the flow past a circular cylinder at low Reynolds numbers. *Journal of Fluid Mechanics*, 6(4):547–567, 1959.

[144] J. J. Tyson and S. H. Strogatz. The differential geometry of scroll waves. *International Journal of Bifurcation and Chaos*, 4:723–744, 1991.

[145] P. Walstra. *Physical Chemistry of Foods*. Marcel Dekker, Inc., New York, 2003.

[146] F. M. White. *Fluid Mechanics*. McGraw Hill Inc., New York, USA, 1991.

[147] F. M. White. *Viscous Fluid Flow*. McGraw Hill Inc., New York, USA, 2003.

[148] J. Z. Wu, H. Y. Ma, and M. D. Zhou. *Vortical Flows*. Springer-Verlag, Heidelberg, Germany, 2015.

[149] M. M. Zdravkovich. *Flow around Circular Cylinders; Volume 1. Fundamentals*. Oxford Science Publications, Oxford, UK, 1997.

[150] M. M. Zdravkovich. *Flow around Circular Cylinders; Volume 2. Applications*. Oxford Science Publications, Oxford, UK, 2009.

Indian Institute of Technology Guwahati

Publications:

Based on the work in this thesis, the following research articles are published or communicated.

List of Papers Published/Accepted.

1. S. Biswas and J. C. Kalita, Moffatt eddies in the driven cavity: a quantification study by an HOC approach, *Computers and Mathematics with Applications*, 76 (3): 471-487, 2018.
2. J. C. Kalita, S. Biswas and S. Panda, Finiteness of corner vortices, *Zeitschrift für angewandte Mathematik und Physik (ZAMP)*, 69 (2): 37, 2018.
3. S. Biswas and J. C. Kalita, Moffatt vortices in the lid-driven cavity flow, *Journal of Physics: Conference Series*, 759 (1): 012081, 2016.

List of Papers Communicated/Under Preparation.

1. S. Biswas and J. C. Kalita, Topology of corner vortices in the lid-driven cavity flow: 2D vis a vis 3D, *To be communicated.*
2. S. Biswas and J. C. Kalita, Topological equivalence class of Moffatt vortices, *To be communicated.*
3. J. C. Kalita, S. Biswas and S. Panda, The finiteness of vortices in steady incompressible viscous fluid flow, *To be communicated.*
4. J. C. Kalita, S. Biswas, Topology of Taylor-Görtler-Like vortices in the 3D lid-driven cavity flow, *To be communicated.*
5. S. Biswas and J. C. Kalita, On the identification of U-shaped like vortices in the 3D lid-driven cavity flow, *Under preparation.*

Indian Institute of Technology Guwahati